



University
of Glasgow

Kurkiewicz, Teresa (2011) *New NMR methods for studying dynamics in solids*. PhD thesis.

<http://theses.gla.ac.uk/2613/>

Copyright and moral rights for this thesis are retained by the author

A copy can be downloaded for personal non-commercial research or study, without prior permission or charge

This thesis cannot be reproduced or quoted extensively from without first obtaining permission in writing from the Author

The content must not be changed in any way or sold commercially in any format or medium without the formal permission of the Author

When referring to this work, full bibliographic details including the author, title, awarding institution and date of the thesis must be given

**New NMR methods for studying dynamics in
solids**

Submitted in partial fulfilment of the requirements
for the degree of Doctor of Philosophy

Teresa Kurkiewicz

University of Glasgow

Department of Chemistry

January 2010

Abstract

There is currently much interest in the investigation of dynamics in solids and the primary goal of this thesis is to present well-known and new NMR methods used for studying motion on Larmor and spectral timescale.

The quadrupolar interaction usually dominates solid-state NMR spectra of quadrupolar nuclei. When the magnitude of quadrupolar interaction is large then the second-order correction to the dominant Zeeman Hamiltonian must be considered. Owing to this second-order quadrupolar effect, NMR peaks can be displaced from their chemical shift positions by a second-order shift. When considering motional averaging of the second-order shift, the critical frequency is the Larmor frequency, ν_0 . In the case of motion that is faster than the Larmor precession, the isotropic quadrupolar shift is affected. This analogous phenomenon in solution-state NMR is known as the "dynamic shift".

In Chapter 4, it will be shown that multiple-quantum NMR measurements of isotropic second-order quadrupolar shifts are a simple way to probe nanosecond timescale motions in solids. An analysis of one- and two-dimensional ^{11}B MAS NMR spectra of three isomers of the *closo*-carboranes gives the results that provide the first evidence for the presence of solid-state dynamic shifts.

There are several experiments that provide a sensitive test for the presence of dynamics on spectral timescale. One piece of evidence for dynamics on the spectral timescale is a motional broadening of quadrupolar satellite-transition spinning sidebands. Therefore, it is possible to investigate the influence of dynamic reorientation on satellite-transitions MAS spectra by recording variable-temperature one-dimensional spectra with wide spectral width or by comparing two-dimensional STMAS spectra with MQMAS spectra. These methods can be extended to ^2H NMR spectroscopy as the sidebands observed in the magic angle spinning (MAS) NMR spectrum of a spin $I = 1$ ^2H nucleus may be very strongly broadened due to interference between the line-narrowing effects of MAS and the dynamics-driven reorientation of the ^2H quadrupole tensor, if motion is present in the solid.

In the last chapter, the ^{27}Al , ^{31}P and ^2H NMR study of AlPO-34 type materials with the topology of chabazite are undertaken and the use of the full range of NMR methods to develop a structure and dynamic behaviour of these materials is presented. In addition, the NMR calculations are performed in order to combine DFT calculations with experimental data. Finally, GaPO-34 samples were investigated to extract information about the effects of Ga substitution in AlPO-34 on dynamical behaviour.

Declaration

This thesis is available for library use on the understanding that it is copyright material and that no quotation from the thesis may be published without proper acknowledgement.

I certify that all material in this thesis that is not my own work has been identified and that no material has previously been submitted and approved for the award of a degree by this or any other university.

.....

Teresa Kurkiewicz

January 2010

Acknowledgment

I would like to express my appreciation to the following people:

My supervisor, Prof. Stephen Wimperis, for his supervision, guidance and knowledge.

Dr Sharon Ashbrook, for her advices on the ALPO project.

Dr Michael Thrippleton, for his help on my first project and my first publication, his assistance and patience.

Dr John Griffin for his help on my projects and my PhD thesis and for his company in Glasgow and in St. Andrews.

The Wimperis Group (Dr Alan Gregorovic, Dr Marica Dowell and Dr Tom Ball) for their help with NMR and all discussions.

My parents for their love and support.

My siblings, the closest relatives and friends, for their love, care, support and encouragement. I cannot imagine becoming a doctor without you.

Contents

Abstract.....	2
Declaration.....	3
Acknowledgment.....	4
Contents.....	5
1. Introduction.....	9
1.1. The key NMR developments.....	9
1.2. Thesis overview.....	15
1.3. General experimental details.....	17
2. Fundamentals.....	20
2.1. Zeeman interactions.....	20
2.2. The vector model.....	25
2.3. Fourier transform NMR.....	29
2.4. NMR Hamiltonians.....	31
2.4.1. Dipolar interactions.....	32
2.4.2. J-coupling interactions.....	35
2.4.3. Chemical shift interactions.....	36
2.4.4. Quadrupolar interactions.....	39

3.	High-resolution techniques and the other methods	48
3.1.	Magic angle spinning.....	48
3.1.1.	The MAS technique.....	48
3.1.2.	Spinning sidebands.....	49
3.2.	Multiple-quantum MAS NMR.....	51
3.2.1.	Basic sequence.....	52
3.2.2.	Amplitude-modulated experiments.....	56
3.2.3.	Shifted-echo experiments.....	58
3.2.4.	Split- t_1 experiments.....	58
3.3.	Satellite-transitions MAS NMR.....	61
3.4.	Cross-polarization experiment.....	66
3.5.	Insensitive nuclei enhance by polarization transfer (INEPT) experiment.....	67
3.5.1.	Double insensitive nuclei enhance by polarization transfer.....	69
3.6.	Spin-lattice relaxation time measurements.....	71
4.	Second-order quadrupolar shifts as an NMR probe of fast molecular- scale dynamics	74
4.1.	Dynamics in solids.....	74
4.1.1.	Introduction.....	74
4.1.2.	Slow-timescale motion – the two-dimensional exchange	

	experiment.....	75
4.1.3.	Intermediate-timescale motion – lineshape analysis.....	79
4.1.4.	Fast-timescale motion – spin-lattice relaxation time and second-order quadrupolar shift.....	85
4.2.	<i>Closo</i> -carboranes.....	89
4.2.1.	Introduction.....	89
4.2.2.	Results and discussion.....	90
4.2.3.	Conclusion.....	107
5.	Dynamic behaviour of microporous solids.....	110
5.1.	Introduction.....	110
5.2.	AlPO-34: Results and discussion.....	118
5.2.1.	As-made AlPO-34.....	118
5.2.2.	Deuterated AlPO-34.....	132
5.2.3.	Calcined AlPO-34.....	143
5.3.	CASTEP calculations.....	149
5.4.	GaPO-34 – gallium phosphate materials.....	155
5.5.	Conclusion.....	162
	Appendices.....	165
A	Preparation of 9,12-diiodo- <i>ortho</i> -carborane and as-made AlPO-34.....	165

B	Coefficients of zero-, second- and fourth-rank terms in Eqn. (3.8) for half-integer spin nuclei.....	167
C	Reduced rotation matrix elements.....	168
D	MQMAS ratios ($A_4(I, m_I) / A_4(I, 1/2)$) for half-integer spin nuclei.....	170
E	STMAS ratios for half-integer spin nuclei.....	171
	References.....	172

Chapter 1: Introduction

1.1. The key NMR developments

Nuclear magnetic resonance (NMR) is a powerful technique that has been around for more than 60 years. The versatility of NMR has made it a widespread scientific tool. The NMR phenomenon has proven an essential tool in physics and it has revolutionised chemistry and biochemistry. It has also made significant contributions to medicine and is now making an impact in geochemistry, chemical engineering and food technology.

The developments in liquid- and solid-state NMR have a long and successful history. It all started with the independent discoveries by the groups of Bloch and Purcell. In 1946 Purcell, Torrey and Pound [1.1] brought protons ^1H in solid paraffin wax to resonance and at that time Bloch, Hansen and Packard [1.2] did the same with liquid water.

Soon afterwards, in 1949, the chemical shift was discovered and two years later Arnold, Dharmatti and Packard observed that the chemical shift due to the $-\text{OH}$ proton in ethanol varied with temperature, showing three separate

resonances for each proton [1.3].

In liquid-state NMR spectra peaks are narrow and well-resolved due to rapid rotation of molecules in liquids. However, in solid-state NMR spectra line broadening is observed because rapid molecular motion in powdered solids are absent. These anisotropically broadened lineshapes can be MHz wide and difficult to interpret. Therefore, new development of methods in solid-state NMR and new instrumentation has focussed on ways of obtaining high-resolution isotropic spectra in which all anisotropic line broadening has been removed.

The first technique for improving the resolution of solid-state NMR spectra of powdered samples is magic angle spinning (MAS) method, developed by the groups of Andrew in 1958 [1.4,1.5] and independently by the group of Lowe in 1959 [1.6]. MAS technique involves a rapid rotation of a sample about an axis at 54.74° with respect to the magnetic field. Andrew used magic angle spinning to narrow the ^{23}Na line in NaCl, whereas Lowe used this technique to narrow the dipolar broadened ^{19}F resonances in CaF_2 and Teflon. Currently, MAS is used to remove the effect of chemical shift anisotropy, to assist in the removal of heteronuclear dipolar coupling effects, and to narrow NMR peaks of quadrupolar nuclei. MAS may be used on its own, and may also be successfully combined with other, more recently discovered, techniques.

The methodological development of NMR entailed instrumental evolution and, later in the 1950s, the first commercial spectrometers appeared. These were based on conventional electromagnets and permanent magnets. However, by the 1960s the superconducting magnet had already come to be largely adopted.

Meanwhile, one of the most widely employed methods, in NMR of solids, the Hartmann-Hahn cross-polarization technique, used to increase the sensitivity when observing low- γ spins in solids, was developed. In this experiment, the enhancement of the magnetization of the low- γ nucleus (e.g., ^{13}C) is achieved by cross-polarization from an abundant high- γ nucleus (e.g., ^1H) [1.7].

Soon after this, in 1966, the chemists Ernst and Anderson demonstrated Fourier transform nuclear magnetic resonance (FT NMR), in which short, high-power pulses excite all transitions in the spectrum simultaneously [1.8]. This procedure quickly replaced the older scanning techniques.

In 1971, Belgian physicist Jeener conceived of a new way of applying pulse sequences and displaying the results in terms of two separate frequency scales [1.9]. The concept was soon developed into the very important method of two-dimensional NMR particularly in the laboratory of Ernst (who received the

Nobel Prize in Chemistry in 1991 for his major contributions to FT NMR in both one and two frequency dimensions) and the laboratory of Freeman.

Another approach to achieve line narrowing for an abundant spin system, such as protons, in solids was introduced by Ostroff and Waugh [1.10] and Mansfield and Ware [1.11]. They imposed artificial motion on the solid by making the spin operators time-dependent, i.e., by introducing motion in the so-called spin space. This was realized by means of a special radiofrequency (rf) pulse sequence, which eliminates the decay due to the dipolar interaction almost completely while the decay due to the chemical shift is only partially eliminated. Hence, after Fourier transform, a spectrum is obtained that contains chemical shift information only. Improved rf sequences have been developed to remove the dipolar broadening even more completely. However, the proton spectra still often lack resolution, due to the remaining chemical shift anisotropy. Therefore, these multiple-pulse sequences have been combined with magic angle spinning, yielding the so-called CRAMPS (combined rotation and multiple-pulse spectroscopy) technique. With this technique, spectra are obtained with narrow lines determined by the isotropic chemical shift.

During the period 1980-2000 a number of clever methods were developed for obtaining high-resolution NMR spectra of half-integer quadrupolar nuclei, because MAS cannot completely average the quadrupolar interaction, leaving

residual (usually significant) line broadening in MAS spectra. Four major technical solutions have been developed to achieve enhanced resolution in the spectra of quadrupolar nuclei. These are double rotation (DOR) [1.12-1.14], dynamic angle spinning (DAS) [1.12,1.15], multiple-quantum magic angle spinning (MQMAS) [1.16-1.19] and satellite-transition magic angle spinning (STMAS) [1.20].

In the DOR technique the sample is spun simultaneously at two angles, at an angle of 54.7° relative to the direction of the static magnetic field (the magic angle) and an inner rotor containing a sample, placed in the outer rotor, is rotated around the axis at an angle of 30.6° or 70.1° relative to the first one. As might be imagined, this method, in which one rotor is spun within another, is experimentally challenging, but has been used successfully.

In DAS, the experiment involves spinning the sample at two different angles sequentially over different time periods, in order to refocus the signal. In this way a two-dimensional spectrum is obtained, with isotropic signals (quadrupolar broadening removed) in one dimension and quadrupolar broadened anisotropic patterns in the other. The two-dimensional spectrum therefore permits improved resolution in one dimension, free from quadrupolar, chemical shift anisotropy and dipolar effect.

One of the major developments is the MQMAS method, proposed in 1995 by Frydman and Harwood. This is a two-dimensional technique involving the correlation of multiple- and single-quantum coherences under MAS conditions. More details and an application of the MQMAS technique to both crystalline and amorphous materials will be discussed in later chapters of this thesis.

In the STMAS experiment, single-quantum (satellite, i.e., $m_I = 3/2 \leftrightarrow 1/2$ and $m_I = -1/2 \leftrightarrow -3/2$, transition) coherences are correlated with single-quantum (central, $m_I = 1/2 \leftrightarrow -1/2$, transition) coherences. Both, central and satellite transitions are affected by second-order quadrupolar interaction and the ratio of the second-order quadrupolar broadening of the satellite and central transitions is known as the STMAS ratio. Since the magnitudes of these broadenings are related by a simple numerical factor, the correlation of the two transitions in two-dimensional experiment will allow the removal of the second-order broadening. This experiment has been used to study dynamics and it might be useful for the study of low- γ nuclei.

One advantage of the transition-correlated MAS experiments over the other methods is that they are easier techniques to implement experimentally in terms of the physical procedure, because they only involve magic angle spinning and therefore can be performed with most commercial MAS probes.

The importance of solid-state NMR has increased dramatically over the last 20 years and solid-state NMR spectroscopy has the potential of becoming one of the key methods to provide the structural and dynamic information. Many other techniques such as three-dimensional, ^2H double-quantum magic angle spinning or satellite-transition acquired in real time by magic angle spinning (STARTMAS) methods have recently been developed or are under development and that show great potential for future investigations. Detailed descriptions of some of the above techniques and their applications will be discussed in Chapter 3.

Nuclear magnetic resonance, first discovered in 1946, has evolved into one of the premier techniques for molecular identification and the development of NMR methods is far from being complete. Furthermore, the next generation of high-field spectrometers in the range of a gigahertz will enable NMR to handle considerably more complex materials than has been possible before.

1.2. Thesis overview

This thesis is mainly concerned with the description of two classes of compounds that have important application in chemistry, physics, biology, medicine and other branches. The first class of these materials is *closo*-carboranes and they are used here as a model for studying dynamic shift effects

in solids, explaining also what the dynamic shift is and how NMR methods may be used to investigate this effect. The second class of compounds of interest in my study are the aluminophosphates (AlPOs). I will concentrate on AlPO samples made with different template molecules and also their derivatives such as gallium phosphate materials. The dynamic behavior of AlPO will be also shown but using different NMR methods, described in the theoretical chapters of this thesis, than in the case of carboranes.

The first chapter talks about the new discoveries that have been made during the last 60 years and briefly describes NMR methods concentrating on the techniques used for solid-state NMR.

Chapter 2 presents a discussion of the fundamental principles for NMR starting with Zeeman interactions, the vector model and the Fourier transform and then describing NMR Hamiltonians for every interactions that is a source of inhomogeneous broadening in NMR spectra, such as dipolar, scalar and chemical shift interactions. However, in particular, the focus is placed on quadrupolar interactions as they present the dominant interaction for quadrupolar nuclei and the investigations of quadrupolar nuclei are described in the experimental sections of this thesis.

Various high-resolution techniques are described in Chapter 3. This

chapter presents the way in which these techniques can be used to remove broadening from NMR spectra, especially for quadrupolar nuclei. The resulting high-resolution spectra, for example two-dimensional MQMAS or STMAS spectra provide, in turn, important information about structure and dynamics.

In Chapter 4, new method to probe nanosecond timescale motions in plastic solids is introduced. This chapter shows that measurements of isotropic quadrupolar shifts using multiple-quantum MAS spectroscopy give information on molecular reorientation and the carboranes are good examples for studying reorientation in solids. Their molecules, arranged within a lattice, are still free to reorientate on the nanosecond timescale and can therefore have a measureable influence on the centre-of-gravity shifts of quadrupolar nuclei.

Chapter 5 applies the most of the methods described in Chapter 3 and additionally *ab initio* methods [1.21], that can be used to calculate a wide range of physical properties of materials, to investigate structure and dynamic behaviour of aluminophosphates and their derivatives. The results of these experiments and calculations are discussed.

1.3. General experimental details

The experiments presented in this thesis were performed using a Bruker

Avance NMR spectrometer equipped with a widebore 9.4, 14.1 or 20.0 T magnet and 2.5-mm and 4-mm broadband MAS probes. All experiments employed magic angle spinning (MAS) and used rotation speeds of 10–33 kHz. All radiofrequency field strengths were calibrated independently on a variety of the samples and the values quoted are approximate only. Chemical shifts are reported in ppm relative to BF_3OEt_2 (l) for ^{11}B , 1 M $\text{Al}(\text{NO}_3)_3$ (aq) for ^{27}Al , 1 M $\text{Ga}(\text{NO}_3)_3$ (aq) for ^{71}Ga , TMS- d_{12} for ^2H and TMS for ^1H .

Low-temperature measurements were carried out by passing the rotor bearing gas through a liquid nitrogen-cooled heat exchanger. As a consequence of frictional sample heating due to MAS, the temperatures quoted in this article are likely to underestimate the true sample temperature by approximately 5 K.

Some of the samples were obtained from commercial suppliers and used without further purification. The aluminium and gallium phosphate materials (and their deuterated equivalents) were synthesized by Dr R. I. Walton (University of Warwick). The sample of 1,3-dimethylimidazolium- AlPO_3 was synthesized by a project student Lucy Clark of the University of St. Andrews. The samples of *meta*- and *para*-carborane were provided by Professor A. J. Welch (Heriot Watt University). The 9,12-diiodo-*ortho*-carborane was synthesized by a project student Darryn Mark. The preparation of some of the sample is presented in Appendix A.

First-principles calculations of NMR parameters of aluminium phosphate materials, meaning density functional theory calculations with plane waves and pseudopotentials, were performed using NMR CASTEP code. The CASTEP program originally was developed by Payne and co-workers in late 1980s and early 1990s [1.21]. CASTEP permits geometry optimisation, as well as calculation of the electronic properties of all manner of materials and molecules. This program can also give information about total energies and forces on an atomic system and perform molecular dynamic simulations.

Full experimental parameters are given in figure captions.

Chapter 2: Fundamentals

2.1. Zeeman interaction

Nuclei that can be observed in nuclear magnetic spectroscopy are magnetic nuclei, those with non-zero spin quantum number, I . The spin quantum number arises from the number of protons and neutrons in the nucleus and can be equal to 0, 1/2, 1, 3/2, 2,.... In the case of even number of protons and neutrons, $I = 0$, the nucleus is not observable in NMR spectrum. However, most elements have at least one NMR-active isotope.

The most important nuclei for structural studies in liquid-state NMR, especially in organic chemistry, are nuclei with $I = 1/2$, such as ^1H , ^{13}C , ^{15}N , ^{19}F or ^{31}P . On the other hand, in solid-state NMR, the quadrupolar nuclei, those with $I > 1/2$, are mainly of interest to NMR spectroscopists.

All of the magnetic nuclei are charged particles possessing an intrinsic angular momentum (spin). As the angular momentum is a vector quantity, it has the magnitude and direction. For the nucleus, the square of the magnitude of the intrinsic angular momentum, I , is a fundamental property of the state of

the nucleus. Its value is:

$$|\mathbf{I}|^2 = I(I+1)\hbar^2 \quad (2.1)$$

where $\hbar = \frac{h}{2\pi}$ and h is the Planck constant.

The spin state is also characterized by the projection of the angular momentum along any one of the axes (usually it is the z-axis of the coordinate system in which the system is described):

$$I_z = m_I \hbar \quad (2.2)$$

where m_I is referred to as the magnetic quantum number and this quantum number takes one of the $2I + 1$ integer values ($m_I = -I, -I + 1, \dots, +I$).

In the absence of an external field, each of the $2I + 1$ spin states has the same energy. However, as one of the characteristic features of the magnetic nuclei is also their possession of a magnetic dipole moment, $\boldsymbol{\mu}$, given by:

$$\boldsymbol{\mu} = \gamma \mathbf{I} \quad (2.3)$$

where γ is a gyromagnetic ratio characteristic for every nucleus, in the presence of an external magnetic field, the z-component of magnetic dipole moment interacts with the applied magnetic field and energies of each of $2I + 1$ states are slightly modified. This change of energies of the spin states due to the interaction of the z-component of magnetic dipole moment with the applied magnetic field is known as the Zeeman interaction. The energy of this interaction is given by:

$$E = -\mu_z B_0 \quad (2.4)$$

if B_0 is along the z axis.

It can be deduced from Eqns. (2.2), (2.3) and (2.4) that the states of different angular momentum projection along the field have energies that depend on the projection quantum number, magnetic field and the gyromagnetic ratio according to the equation below:

$$E_{m_I} = -m_I \gamma \hbar B_0 \quad (2.5)$$

The gyromagnetic ratio, γ , may have either sign, depending on whether the magnetic dipole moment is aligned parallel or antiparallel to the field. For particles with a positive value of γ (the majority of atomic nuclei), the z-

component of magnetic dipole moment, μ_z , is parallel to the field, B_0 , and the energy of the state of the angular momentum projection along the field is the lowest.

The particles can undergo a transition between the two energy states. However, allowed energy transitions are between adjacent energy levels ($\Delta m_I = \pm 1$). The energy difference between two adjacent states is given by:

$$\Delta E = \hbar\gamma B_0 \quad (2.6)$$

At thermal equilibrium, the ratio of nuclei between two adjacent levels in accordance with the Boltzmann distribution can be represented by:

$$\frac{n_{\text{upper}}}{n_{\text{lower}}} = e^{\frac{-\Delta E}{kT}} \quad (2.7)$$

where k is the Boltzmann constant ($k = 1.3805 \cdot 10^{-23}$ J/Kelvin) and T is the temperature in Kelvin. It is generally found that the number of spins in the lower energy level is slightly higher (by about one in every 10^5) than the number of spins in the higher energy level.

When the energy of the absorbed photon ($E = h\nu$) matches the energy

difference in Eqn. (2.6) a transition occurs. This may be expressed in terms of the frequency ν_0 (in units of Hz), called Larmor frequency, as:

$$\nu_0 = \frac{\gamma B_0}{2\pi} \quad (2.8)$$

or in angular frequency units (rad s^{-1}) as:

$$\omega_0 = \gamma B_0 \quad (2.9)$$

As the frequency applied to a sample, which correspond to the energy gap, ΔE , correspond to the radiofrequency (rf) band of the electromagnetic spectrum, the rf radiation is used in NMR spectroscopy.

The displacement of the energy levels due to Zeeman interaction can be presented graphically and the Figure 2.1 illustrates the effect of the Zeeman interaction on the energy levels of spins $I = 1$ and $I = 3/2$ nuclei.

However, the interactions that are really of interest to NMR spectroscopists are not the Zeeman interactions but the chemical shift (or chemical shift anisotropy), the scalar interaction (J -coupling interaction), the dipolar interaction and, for spins $I > 1/2$, the quadrupolar interaction. All of

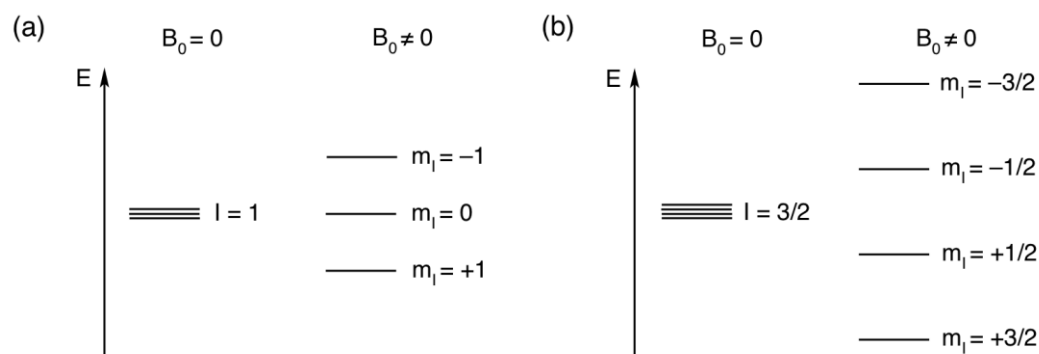


Figure 2.1. The effect of the Zeeman interaction on the energy levels of (a) a spin $I = 1$ nucleus and (b) a spin $I = 3/2$ nucleus.

these will be described in later sections.

2.2. The vector model

The vector model is a simple way to visualize rf pulses and free precession intervals in NMR without using the quantum mechanics needed to describe the behaviour of an ensemble of spins in macroscopic samples. The vector model was first proposed by Bloch in 1946 [2.1].

As described in previous section, in the presence of the external magnetic field and at thermal equilibrium, nuclei in a sample will populate the adjacent energy levels according to the Boltzmann distribution. This results in alignment of the z-components of magnetic moments along the field direction, so the sample has a net magnetisation vector along the arbitrary z-axis. If there is a collection of a large number of nuclear spins, then the aligned nuclear magnetic

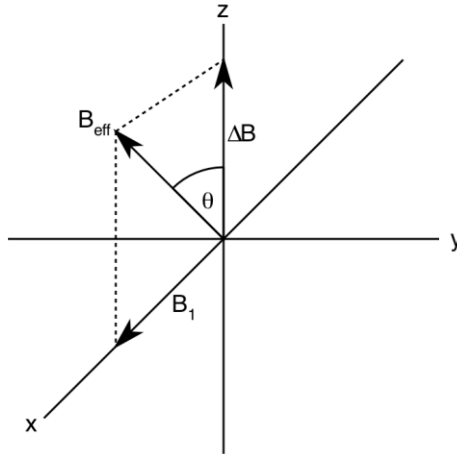


Figure 2.2. Vector model presentation of the magnetic fields present in the rotating frame.

moments lead to a bulk magnetization of the spins in a sample, \mathbf{M} .

If an rf pulse is applied to \mathbf{B}_0 with its oscillation frequency ω_{rf} (the transmitter frequency) very close to the Larmor frequency, ω_0 , the bulk magnetization vector tilts away from the z -axis and begins to precess around z -axis for the duration of the pulse length.

Because it is difficult to visualize this effect in the static laboratory frame, it turns out to be much easier to work out this in a *rotating frame*, in which the Cartesian axes rotating in the xy -plane (around the z -axis) at the frequency of the rf pulse, ω_{rf} . The rf pulse in the rotating frame can be thought of as a temporarily applied static magnetic field, B_1 , applied orthogonally to B_0 . If the pulse is off-resonance, the main static field B_0 is replaced by a reduced

(offset) field, ΔB , given by:

$$\Delta B = -\frac{\Omega}{\gamma} \quad (2.10)$$

where the offset Ω is the frequency of precession in the rotating frame and is given by:

$$\Omega = \omega_0 - \omega_{rf} \quad (2.11)$$

The associated *flip angle*, which is the angle by which the bulk magnetization vector nutates from the z-axis is:

$$\beta = \omega_1 \tau_p \quad (2.12)$$

where τ_p is the pulse length and ω_1 is the strength of the rotating field ($\omega_1 = -\gamma B_1$).

The offset field and the B_1 field added vectorially give an effective field B_{eff} , as shown in Figure 2.2 and, in the rotating frame, the bulk magnetization vector precesses around this effective field, just as in the laboratory frame the

Larmor precession takes place around the B_0 field. However, if the pulse is on-resonance ($\omega_{\text{rf}} = \omega_0$), the offset is zero and, referring to Fig. 2.2, the effective field lies along x-axis and is of size ω_1 .

After the rf field is turned off, the bulk magnetization vector starts to precess around z-axis, together with the xy plane. As well as the precession, there is a relaxation of the vector to bring it back along the z-axis.

The relaxation process has two components, the magnetization along the z-axis relaxes towards its equilibrium value and the transverse components (x and y) relax towards zero. As the bulk magnetization vector is composed of the magnetic moments of many individual spins, some of them may precess faster and some of them slower than the rotating axes. As a result, the magnetic moments spread out and the x- and y-components of the individual nuclear magnetic moments may cancel one another out reducing the length of the bulk magnetization vector. Therefore, the transverse components relax at a faster rate than the z component does in its return to equilibrium and two time constants are required to fully describe spin relaxation. These two relaxation times are called the spin-lattice (longitudinal) relaxation time, T_1 , and the spin-spin (transverse) relaxation time, T_2 . Transverse relaxation causes the x and y-components of the nuclear magnetization to decay towards zero, whilst

longitudinal relaxation returns the z-magnetization vector to its equilibrium value.

The rotation of the magnetization about the z-axis gives rise to a current in the rf coil located in the transverse plane and, after various manipulations, this current results in a signal called the free induction decay (FID) that is detected in an NMR experiment.

2.3. Fourier Transform NMR

Fourier transformation [2.2-2.4] is a mathematical operation that translates the time-domain function (FID) into the frequency-domain function (the spectrum). The free induction decay is the sum of many oscillating waves of differing frequencies, amplitudes and phases. It is detected using two detectors orthogonal to each other in the rotating frame. This method is known as quadrature detection [2.5]. For each resonance in the spectrum, the x and y components are detected simultaneously, corresponding to cosine and sine functions of the offset frequency, Ω , respectively. The x component is used as the real input and the y component as the imaginary input to a complex Fourier transform. As mentioned before the transverse magnetization decays exponentially with a rate constant $1/T_2$ and the signal then becomes:

$$f(t) = \exp\{i\Omega t\} \exp\left\{-\frac{t}{T_2}\right\} \quad (2.13)$$

for values of $t \geq 0$.

This complex time-domain signal can be converted into the frequency-domain function or into the spectrum by Fourier transformation:

$$F(\omega) = \int_{-\infty}^{\infty} f(t) \exp\{-i\omega t\} dt = A(\Delta\omega) - iD(\Delta\omega) \quad (2.14)$$

where:

$$A(\omega) = \frac{1/T_2}{(1/T_2)^2 + (\Delta\omega)^2} \quad (2.15)$$

is an absorptive Lorentzian function and

$$D(\omega) = \frac{\Delta\omega}{(1/T_2)^2 + (\Delta\omega)^2} \quad (2.16)$$

is a dispersive Lorentzian function. Both functions utilize the offset frequency variable, $\Delta\omega = \omega - \Omega$.

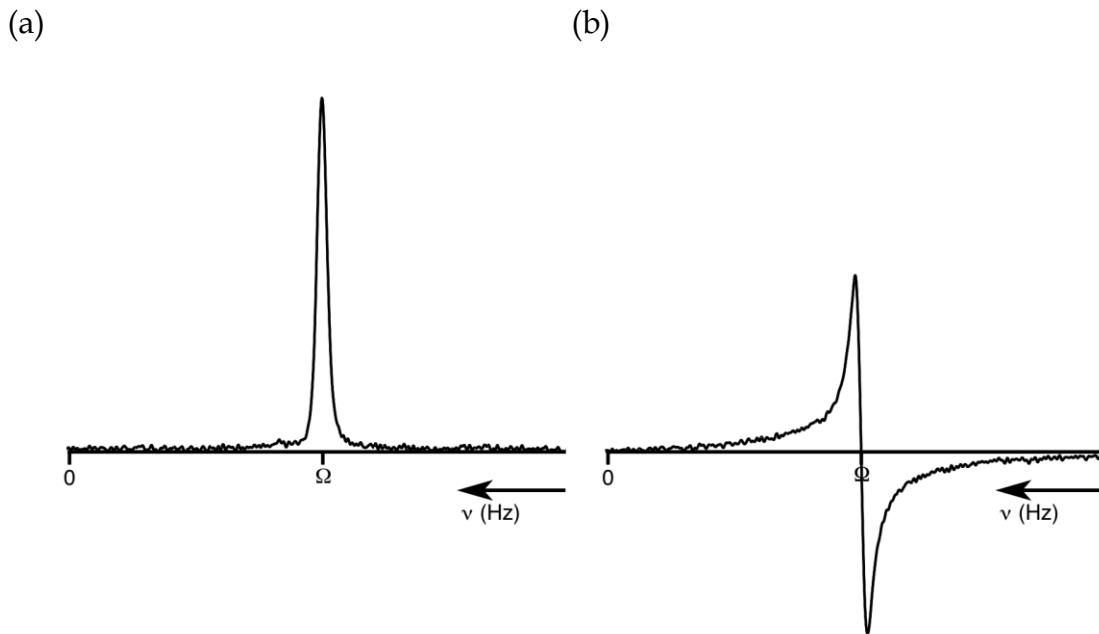


Figure 2.3. The ^{11}B MAS NMR (a) absorption (real) and (b) dispersion (imaginary) Lorentzian experimental lineshapes of solid borane triphenylphosphine (BH_3PPh_3).

This absorption lineshape has a width at half of its maximum height of $1/(\pi T_2)$. The dispersion lineshape is broader than the absorption mode and it has positive and negative parts. Figure 2.3 shows both functions (recorded experimentally).

2.4. NMR Hamiltonians

The operator which represents the observable quantity energy is called the Hamiltonian operator and is commonly represented using the symbol H . The energy associated with each spin state can be obtained by solving the time-

independent Schrödinger equation:

$$H\psi = E\psi \quad (2.17)$$

where ψ is a spin wavefunction and E is the energy.

For example, for a single nuclear spin in a magnetic field of strength B_0 applied along the z -axis in the laboratory frame, the Hamiltonian, which describes the change in the energy levels due to the Zeeman interaction, is given by:

$$H_Z = \omega_0 I_z \quad (2.18)$$

As the Zeeman interactions are due to the external magnetic fields, the other interactions (dipolar, chemical shift or quadrupolar interactions) originate from the presence of internal magnetic field and each of them can be also represented by Hamiltonian.

2.4.1. Dipolar interactions

In this interaction the local magnetic fields are due to the nuclear

magnetic moments of other, nearby, spins. These local fields depend on the distance between the two spins, r , the gyromagnetic ratios of the spins, γ_I and γ_S , and the angle between the vector joining the two spins and the external magnetic field, θ .

The secular form of the homonuclear dipolar Hamiltonian between two spins I and S is given by [2.6]:

$$H_D^{IS} = -\omega_D [2I_z S_z - I_x S_x - I_y S_y] \quad (2.19)$$

where ω_D is the dipolar coupling parameter, given by:

$$\omega_D = \frac{\omega_D^{\text{PAS}}}{2} (3 \cos^2 \theta - 1) \quad (2.20)$$

with the dipolar coupling constant in the principal axis system equal to:

$$\omega_D^{\text{PAS}} = \frac{\mu_0 \gamma_I \gamma_S \hbar}{4\pi r_{IS}^3} \quad (2.21)$$

In the solution state, the presence of molecular motion averages the dipolar coupling to zero. For solids, however, dipolar couplings among the

spins of a sample can have a major effect on an NMR spectrum, particularly for spin $I = 1/2$ nuclei. Because, in solid-state NMR, magic angle spinning (MAS) plays a similar role to the rapid isotropic rotation of molecules in liquids the MAS technique can be used to remove the effect of homonuclear dipolar coupling from an NMR spectrum, providing the rate of spinning is fast relative to the homonuclear dipolar linewidth. This technique involves rapid rotation of the sample around an axis that is at the "magic angle" (54.74°) with respect to the magnetic field. It can be observed from Eqn. (2.20) that if we spin the sample about an angle of 54.74° (θ is set to 54.74°), then $(3 \cos^2 \theta - 1) = 0$ and the dipolar Hamiltonian is also equal to zero.

In the case of two spin I and S heteronuclei, on the other hand, the secular form of the heteronuclear dipolar Hamiltonian between two spins I and S is given by:

$$H_D^{IS} = -2\omega_D I_z S_z \quad (2.22)$$

This heteronuclear coupling [2.7] may be removed from solid-state NMR spectra and high-power decoupling is the simplest technique, in addition to MAS. This method consists of applying continuous irradiation of very high power at the frequency of the I spin resonance (e.g., ^1H). The required pulse

sequence for the S spin (e.g., ^{13}C) is afterwards applied and the FID of the spin S measured while continuing the I-spin irradiation.

2.4.2. *J-coupling interactions*

In addition to the direct coupling of nuclei via the dipolar coupling, nuclei can also experience a coupling, known as the J coupling or indirect spin-spin coupling. The origin of this effect is an interaction between two nuclear spins due to the influence of bonding electrons on the magnetic field running between the two nuclei. This through-bond interaction in the heteronuclear case can be described by the following Hamiltonian [2.8]:

$$H_J = 2\pi J_{IS} I_z S_z \quad (2.23)$$

where J_{IS} is the heteronuclear J coupling constant between spins I and S.

The J coupling contributes only slightly to the total NMR Hamiltonian in terms of energy but it provides the spin-spin splittings that can be prominent in high-resolution spectra.

In solid-state NMR spectra of quadrupolar nuclei, the scalar coupling

interactions are small compared to other broadening mechanisms, such as the quadrupolar interactions, and they can therefore often be neglected.

2.4.3. *Chemical shift interaction*

When an atom is placed in a magnetic field, its electrons circulate about the direction of the applied magnetic field. This circulation causes a small magnetic field at the nucleus, which opposes the externally applied field. As a result of this, the magnetic field at the nucleus (the effective field), which is less than the applied field, is given by:

$$B = B_0(1 - \sigma) \quad (2.24)$$

and the frequency of precession of the spin changes to:

$$\omega_0' = -\gamma B_0(1 - \sigma) \quad (2.25)$$

where σ is a shielding parameter.

In terms of the Hamiltonian, the shielding for a single spin, with B_0 defined to be along the z axis, is given by:

$$H_{CS} = \gamma\sigma_{z,z}B_0I_z \quad (2.26)$$

where $\sigma_{z,z}$ is the component of the shielding tensor that shields I_z from B_0 and is composed of isotropic and anisotropic (orientation dependent) components:

$$\sigma_{z,z} = \sigma_{iso} + \frac{1}{3} \sum_{i=1}^3 (3 \cos^2 \theta - 1) \sigma_{i,i} \quad (2.27)$$

where θ is the angle that defines the orientation of the B_0 field in the principal axis system of the shielding tensor. This means that the chemical shift is a tensor quantity and the observed quantity depends on the relative orientation of the molecule with respect to the axis of the applied magnetic field.

In a powder sample a broad signal is observed which shows chemical shifts that correspond to all the possible orientations. This powder pattern has singularities that correspond to the three principal components of the shielding tensor (σ_{11} , σ_{22} , σ_{33}). To remove anisotropic contribution to chemical shifts in solids the magic angle spinning technique [2.9] has been widely used.

In an isotropic liquids the molecules are freely tumbling, the anisotropic shielding is averaged and the shielding is equal to its isotropic value (average of

the σ_{11} , σ_{22} , σ_{33} components):

$$\sigma_{\text{iso}} = \frac{\sigma_{11} + \sigma_{22} + \sigma_{33}}{3} \quad (2.28)$$

where σ_{11} , σ_{22} , σ_{33} are the principal tensor components.

The chemical shift of a nucleus is defined in terms of a difference between the resonance frequency of the nucleus and a standard, relative to a standard [2.10]. This frequency is reported in ppm:

$$\delta = \frac{(\omega - \omega_{\text{ref}})}{\omega_{\text{ref}}} \cdot 10^6 \quad (2.29)$$

In ^1H NMR spectroscopy this standard is usually tetramethylsilane, $\text{Si}(\text{CH}_3)_4$ (TMS).

The chemical shift can be related to the shielding by:

$$\delta = 10^6 \frac{\sigma_{\text{ref}} - \sigma}{1 - \sigma_{\text{ref}}} \approx 10^6 (\sigma_{\text{ref}} - \sigma) \quad (2.30)$$

where $\sigma_{\text{ref}} \ll 1$ has been assumed. The chemical shift is, therefore, a

deshielding parameter, as increase in shielding leads to a decrease in chemical shift.

2.4.4. Quadrupolar interactions

The quadrupolar Hamiltonian

Quadrupolar nuclei (those with spin quantum number $I > 1/2$) possess an electric quadrupole moment in addition to the magnetic dipole moment that all NMR-active nuclei must have. Interactions of the nuclear quadrupole moment, eQ , with the electric field gradient (EFG) present at the nucleus are usually dominant in solid-state NMR spectra of quadrupolar nuclei [2.11,2.12]. This interaction affects the nuclear spin energy levels in addition to the other magnetic interactions already described. The nuclear electric quadrupole moment/electric field gradient interaction can be rather large, causing powder patterns of megahertz in width for solid samples consisting of large numbers of randomly oriented crystallites (i.e., powders).

The electric field gradient (EFG) is a three-dimensional entity, described by the three principal values of the EFG tensor, $V_{X,X}$, $V_{Y,Y}$, $V_{Z,Z}$ associated with X, Y and Z principal axis system (PAS) axes, respectively, that satisfy the

condition:

$$V_{x,x} + V_{y,y} + V_{z,z} = 0 \quad (2.31)$$

A measure of the deviation of the EFG from axial symmetry is the asymmetry parameter, η , defined as:

$$\eta = \frac{V_{x,x} - V_{y,y}}{V_{z,z}} \quad (2.32)$$

while the magnitude of EFG tensor is given by $eq = V_{z,z}$.

The quadrupolar coupling constant, C_Q , describes the magnitude of the quadrupolar interaction [2.13] and in units of Hz is written:

$$C_Q = \frac{e^2qQ}{h} \quad (2.33)$$

where eq is the magnitude of EFG tensor and eQ is the nuclear quadrupole moment.

For a quadrupolar nucleus, the total Hamiltonian, neglecting the contribution from smaller interactions described in previous subsections, may

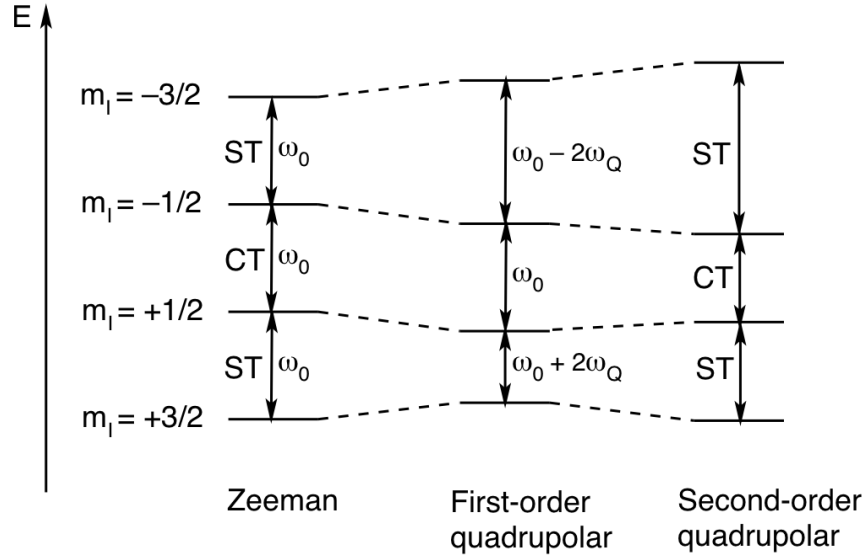


Figure 2.4. Schematic spin $I = 3/2$ energy level diagrams showing the effect of the Zeeman, first- and second-order quadrupolar interactions.

be expressed as the sum of the individual Hamiltonians for the Zeeman and quadrupolar interactions:

$$H = H_Z + H_Q \quad (2.34)$$

where the Hamiltonian H_Z describes the effect of Zeeman interaction and H_Q is the effect of the quadrupolar interactions and in the PAS is given by [2.14]:

$$H_Q = \omega_Q^{\text{PAS}} [I_Z^2 - (1/3)I(I+1) + (\eta/3)(I_X^2 - I_Y^2)] \quad (2.35)$$

where ω_Q^{PAS} is the quadrupolar splitting parameter in the principal axis system

(PAS) and is given, in units of rad s^{-1} , by:

$$\omega_Q^{\text{PAS}} = \frac{3\pi C_Q}{2I(2I - 1)} \quad (2.36)$$

First-order effects of the quadrupolar Hamiltonian

The quadrupolar interactions are strong and contribute to the energy levels. However, as they are smaller than Zeeman interaction, they can be described using perturbation theory of Zeeman energy levels [2.15]. Figure 2.4 shows the effect of the quadrupolar interaction on the energy levels for spin $I = 3/2$ nucleus. If the quadrupolar interaction is much smaller than the Zeeman interaction, the first-order quadrupolar contribution to the energy levels is sufficient to describe the spectrum. For spin $I = 3/2$ the Zeeman interaction results in two distinct types of single-quantum transition, the central transition (CT) with $m_I = +1/2 \leftrightarrow 1/2$ and the satellite transition, ST with $m_I = \pm 1/2 \leftrightarrow \pm 3/2$ [2.11]. Figure 2.4 shows that the central transition of spin $I = 3/2$ nuclei is unaffected by the quadrupolar interaction to the first-order approximation, remaining at the Larmor frequency. The satellite transitions, on the other hand, are affected by the quadrupolar interaction to a first-order approximation resulting in the CT and ST transitions being spaced by $2\omega_Q$, as

$E_{1/2}^{(1)} = E_{-1/2}^{(1)} = -\omega_Q$ and $E_{3/2}^{(1)} = E_{-3/2}^{(1)} = \omega_Q$, where the quadrupolar splitting parameter, ω_Q , is given by:

$$\omega_Q = \frac{1}{2} \omega_Q^{\text{PAS}} [3 \cos^2 \beta - 1 + \eta \sin^2 \beta \cos 2\gamma] \quad (2.37)$$

The angles β and γ in Eqn. (2.37) define the orientation of the PAS of the EFG with respect to the external magnetic field and the quadrupolar splitting parameter, ω_Q^{PAS} , is given in Eqn. (2.36).

As the system presented in Fig. 2.4 contains also multiple-quantum transitions, it can be observed that the triple-quantum transition is not broadened to first-order and has a frequency equal to three times the single-quantum central transition frequency.

More generally, all symmetric, odd-quantum transitions in half-integer ($I = 3/2, 5/2$, etc.) spin systems remain unaffected by this first-order quadrupolar interaction. However, in the case of integer spins, single-quantum transitions exhibit a perturbation by the quadrupolar interaction to a first-order approximation, whilst all symmetric, even-quantum transitions remain unaffected.

The method, which can be used to remove the first-order quadrupolar interaction from the spectrum, is magic angle spinning. As the quadrupolar interactions are large, therefore fast MAS rates are required to fully remove the interaction. However, if the MAS rate is too slow the spectrum will be broken up into a series of spinning sidebands and then magic angle spinning combined with rotor synchronization [2.16] is necessary in order to observe the isotropic lines.

Second-order effects of the quadrupolar Hamiltonian

When the magnitude of quadrupolar interaction is large compared to the Zeeman interactions, then the second-order terms become important to describe the perturbation of the Zeeman energy levels by the quadrupolar interactions. The effect of the second-order quadrupolar interaction upon the energy levels of a spin $I = 3/2$ is, that both single-quantum (CT and ST) transitions and triple-quantum transition are perturbed, as shown in Fig. 2.4.

The results of a full calculation of the perturbation to the energy levels have been published previously [2.13,2.17]. In this calculation the quadrupolar Hamiltonian is transformed from the PAS of the EFG into the laboratory frame and this rotation can be described by Wigner rotation matrix elements,

$D_{m,m}^l(\alpha, \beta, \gamma)$, where α , β and γ are the Euler angles [2.18] relating the two frames of references. The general expression for the second-order quadrupolar contribution to the energy levels, for the nucleus with spin quantum number I , is given by:

$$E_{m_I}^{(2)} = \frac{(\omega_Q^{\text{PAS}})^2}{2\omega_0} \{A^0(I, m_I)Q(\eta) + A^2(I, m_I)Q^2(\alpha, \beta, \gamma, \eta) + A^4(I, m_I)Q^4(\alpha, \beta, \gamma, \eta)\} \quad (2.38)$$

where $A^l(I, m_I)$ are the spin and energy level dependent coefficients of the zeroth-, second- and fourth-rank contributions ($l = 0, 2$ and 4 , respectively) and can be found in Appendix B, while Q^l are the zeroth-, second- and fourth-rank orientationally-dependent functions, although the $l = 0$ rank term is purely isotropic, given by:

$$Q^0(\eta) = \left(1 + \frac{\eta^2}{3}\right) \quad (2.39)$$

$$Q^2(\alpha, \beta, \gamma, \eta) = \left(1 - \frac{\eta^2}{3}\right) D_{0,0}^2(\alpha, \beta, \gamma) - \frac{\sqrt{2}}{\sqrt{3}} \eta \{D_{0,2}^2(\alpha, \beta, \gamma) + D_{0,-2}^2(\alpha, \beta, \gamma)\} \quad (2.40)$$

$$\begin{aligned}
Q^4(\alpha, \beta, \gamma, \eta) = & \left(1 + \frac{\eta^2}{18}\right) D_{0,0}^4(\alpha, \beta, \gamma) - \frac{\sqrt{10}}{6} \eta \{D_{0,2}^4(\alpha, \beta, \gamma) \\
& + D_{0,-2}^4(\alpha, \beta, \gamma)\} + \frac{35}{18\sqrt{70}} \eta^2 \{D_{0,4}^4(\alpha, \beta, \gamma) + D_{0,-4}^4(\alpha, \beta, \gamma)\}
\end{aligned} \tag{2.41}$$

where $D_{m,m'}^1(\alpha, \beta, \gamma)$ are Wigner rotation matrix elements. Each Wigner rotation matrix element, $D_{m,m'}^1(\alpha, \beta, \gamma)$, is defined as [2.19]:

$$D_{m,m'}^1(\alpha, \beta, \gamma) = d_{m,m'}^1(\beta) \exp\{-i(\alpha m + \gamma m')\} \tag{2.42}$$

where $d_{m,m'}^1$ are the reduced rotation elements [2.20] and are given in Appendix C.

The second-order quadrupolar contribution to the energy levels consists of an isotropic quadrupolar shift (proportional to $Q^0(\eta)$) and anisotropic quadrupolar broadening (from $Q^2(\alpha, \beta, \gamma, \eta)$ and $Q^4(\alpha, \beta, \gamma, \eta)$). Therefore, in a powder sample, the effect of the second-order quadrupolar interaction has the result that NMR peaks are no longer sharp and narrow but they are broadened and displaced from their chemical shift positions. The position of the NMR resonance for a quadrupolar nucleus is the sum of the isotropic chemical shift and the isotropic quadrupolar shift.

The method used to remove quadrupolar interaction from the spectrum can be multiple-quantum MAS which will be described in the following chapter.

Chapter 3: High-resolution techniques and other methods

3.1. Magic angle spinning

3.1.1. *The MAS technique*

As discussed in the previous chapter, all NMR interactions have an anisotropic contribution, which is clearly manifested in solid-state NMR spectra. In solid-state NMR, experiments are usually performed on powders comprising a large number of randomly oriented crystallites. The resulting NMR spectrum is then a superposition of the spectra from all crystallites. This gives powder spectra with NMR resonances spread over a large range of frequencies. In order to obtain high-resolution NMR spectra from powders, experimental manipulations of the sample or spins are often required, such as the magic angle spinning (MAS) technique.

The MAS technique involves rapid spinning of the sample about an axis inclined at an angle of 54.74° to the external magnetic field, B_0 . The rapid rotation about this particular axis removes most broadening interactions from

the NMR spectrum. In the case of spin $I = 1/2$, if the sample rotation is fast enough, the anisotropic interactions are averaged out completely. In the case of quadrupolar nuclei, on the other hand, the magic angle technique is employed to remove a quadrupolar interaction to a first-order approximation and also partly removes the effect of the second-order quadrupolar interaction. As discussed in Chapter 2, Eqn. (2.37) shows that the first-order quadrupolar coupling has an orientation dependence of $(3 \cos^2 \beta - 1)$, therefore when $\beta = 54.7^\circ$, this term gives zero and quadrupolar interactions to a first-order approximation are averaged to their isotropic values. However, as shown in Eqns. (2.38) – (2.42), magic angle spinning will also have an averaging effect on the fourth-rank term in the second-order contribution to the transition frequency but the resultant average will not be zero. This means that the second-order quadrupolar interaction cannot be removed completely by MAS. If the quadrupolar interaction is large, MAS assists resolution but does not completely remove anisotropic broadening. This technique may be used on its own, but may also be successfully combined with other line-narrowing techniques. For example, MAS has been used in combination with multiple-quantum NMR spectroscopy.

3.1.2. Spinning sidebands

Magic angle spinning has now become a routine technique for obtaining high-resolution NMR spectra of powder samples. However, a powdered solid consists of a number of crystallites and each of them changes its orientation with respect to the external magnetic field during this rotation. When the magnetization vectors from individual crystallites come back into phase, rotational echoes are formed. As a consequence of this train of rotational spin echoes, a central peak in the NMR spectrum is flanked on both high and low frequency by sidebands spaced at the spinning frequency.

For inhomogeneous [3.1,3.2] nuclear spin interactions (e.g., chemical shift, heteronuclear dipolar coupling, and first-order quadrupolar coupling), the sidebands are sharp, and thus sidebands patterns from different chemical sites are relatively easily resolved. Under slow-speed spinning, when the spinning frequency ν_R is less than the width of static powder pattern, the envelope of spinning sidebands imitates closely the shape of the static powder pattern. If the MAS rate, on the other hand, is greater than the width of static pattern, a centreband at the isotropic frequency (in the case of non-quadrupolar nuclei) is observed [3.3-3.4].

However, the intensities of the observed spinning sidebands can also be affected by line broadening due to any motional processes that may be present

in the sample. The dynamics to which spinning sideband pattern are sensitive are those on a time scale of the order of the inverse of width of the sideband pattern. A dynamic-induced "jump" in the frequency during the rotor period resulting from, e.g., the change in quadrupolar splitting for a ^2H nucleus due to a 180° 'flip' of a D_2O molecule, results in decreased intensity of each subsequent rotational echo and a broadening of the spinning sidebands is observed in the NMR spectrum.

The effect of motional broadening/narrowing of spinning sidebands will be described in more detail in Chapter 4.

3.2. Multiple-quantum MAS NMR

In 1995, Frydman and Harwood proposed a new method for obtaining high-resolution NMR spectra of half-integer quadrupolar nuclei, known as multiple-quantum magic angle spinning (MQMAS). Multiple-quantum NMR spectroscopy of solids is these days a powerful tool for providing important structural information about different materials. This method must be employed in addition to MAS to fully average the effect of the fourth-rank term in the second-order contribution to the transition frequency.

3.2.1. Basic sequence

MQMAS is a two-dimensional technique involving the correlation of multiple- and single-quantum coherences under MAS conditions. By this correlation, it is possible to refocus the fourth-rank broadening, whilst retaining the isotropic shifts.

From Eqn. (2.38) in Chapter 2, it can be seen that the second-order correction to the frequency of the central transition of a spin $I = 3/2$ nucleus under MAS conditions is equal to:

$$E_{|1/2\rangle}^{(2)} - E_{|-1/2\rangle}^{(2)} = \frac{(\omega_Q^{\text{PAS}})^2}{\omega_0} \left\{ \frac{2}{5} Q^0(\eta) + \frac{54}{35} d_{0,0}^4(54.7^\circ) Q^4(\alpha, \beta, \gamma, \eta) \right\} \quad (3.7)$$

and the frequency of the triple-quantum transition in the same spin system is:

$$E_{|3/2\rangle}^{(2)} - E_{|-3/2\rangle}^{(2)} = \frac{(\omega_Q^{\text{PAS}})^2}{\omega_0} \left\{ \frac{6}{5} Q^0(\eta) - \frac{6}{5} d_{0,0}^4(54.7^\circ) Q^4(\alpha, \beta, \gamma, \eta) \right\} \quad (3.8)$$

where the zeroth- and fourth-rank orientationally-dependent functions are given in Eqns. (2.39) and (2.41). The sample rotation about the magic angle averages the second-rank anisotropic term from Eqn. (2.38) to zero.

Figure 3.1a shows the basic two-pulse triple-quantum (for spin $I = 3/2$) MAS pulse sequence and two possible coherence transfer pathways. In this experiment, either $p = -3$ or $p = +3$ coherence is created first and allowed to evolve for a time period t_1 . This coherence is then transformed into observable single-quantum central-transition coherence ($p = -1$) by a further pulse. Phase cycling is used to select a pathway, which is phase-modulated with respect to t_1 .

It can be seen from Eqn. (3.7) that the time-domain signal for such an experiment, using the solid coherence transfer pathway and assuming only quadrupolar interactions, is given by:

$$\begin{aligned}
 s(t_1, t_2) = & \exp\left\{-i \frac{(\omega_Q^{\text{PAS}})^2}{\omega_0} \left[\frac{6}{5} Q^0(\eta) - \frac{6}{5} d_{0,0}^4(54.7^\circ) Q^4(\alpha, \beta, \gamma, \eta) \right] t_1 \right\} \\
 & \times \exp\left\{-i \frac{(\omega_Q^{\text{PAS}})^2}{\omega_0} \left[-\frac{2}{5} Q^0(\eta) + \frac{54}{35} d_{0,0}^4(54.7^\circ) Q^4(\alpha, \beta, \gamma, \eta) \right] t_2 \right\}
 \end{aligned} \tag{3.9}$$

The ratio of the rank $l = 4$ anisotropic broadening between triple- and single-quantum coherence is referred to as the MQMAS ratio. The MQMAS ratios for all available odd-order coherences for half-integer spins are given in Appendix D. The sign of the MQMAS ratio is very important since it determines the coherence selection in the MQMAS experiments. The correlation must be the $+|p|$ and -1 coherence, if the MQMAS ratio is positive, and $-|p|$ and -1

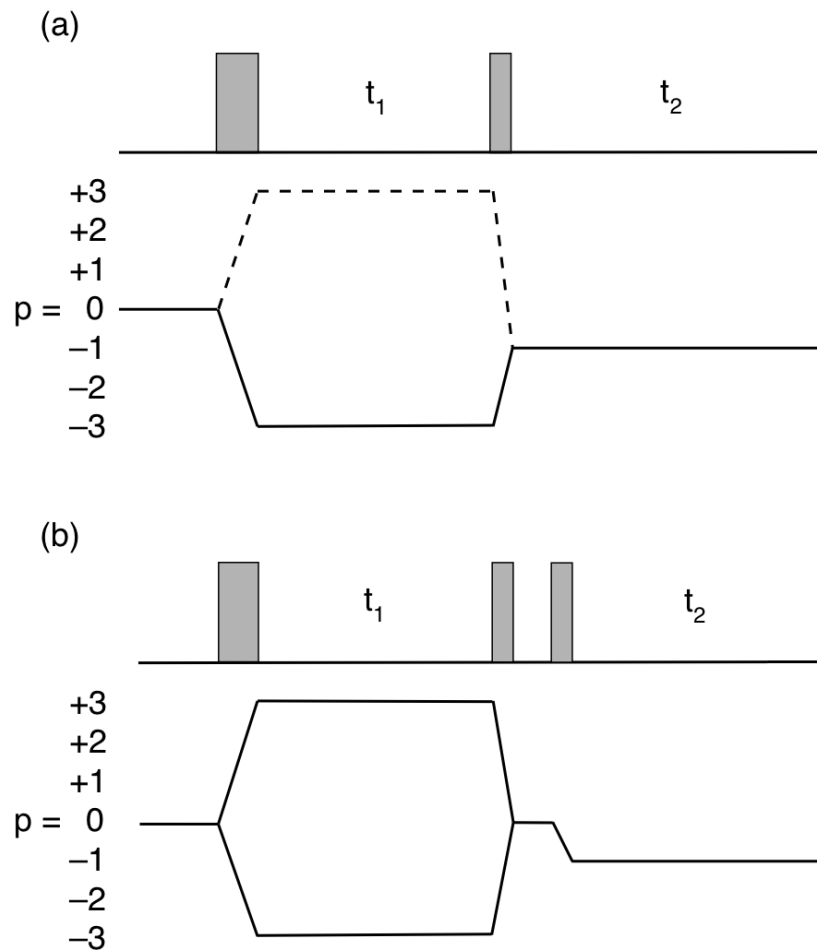


Figure 3.1. Pulse sequences and coherence transfer pathway diagrams for the (a) basic two-pulse and (b) amplitude-modulated z-filter triple-quantum MAS experiments.

coherences, if the ratio is negative, to refocus the second-order broadening at positive t_2 values. The pathway where the anisotropic broadening appears to be refocused at positive values of the acquisition time, t_2 , is termed the echo pathway. On the other hand, the pathway where the echo formed by refocusing of the anisotropic broadening moves backward in t_2 as t_1 increases is known as the antiecho pathway. Furthermore, the MQMAS ratio determines the gradient

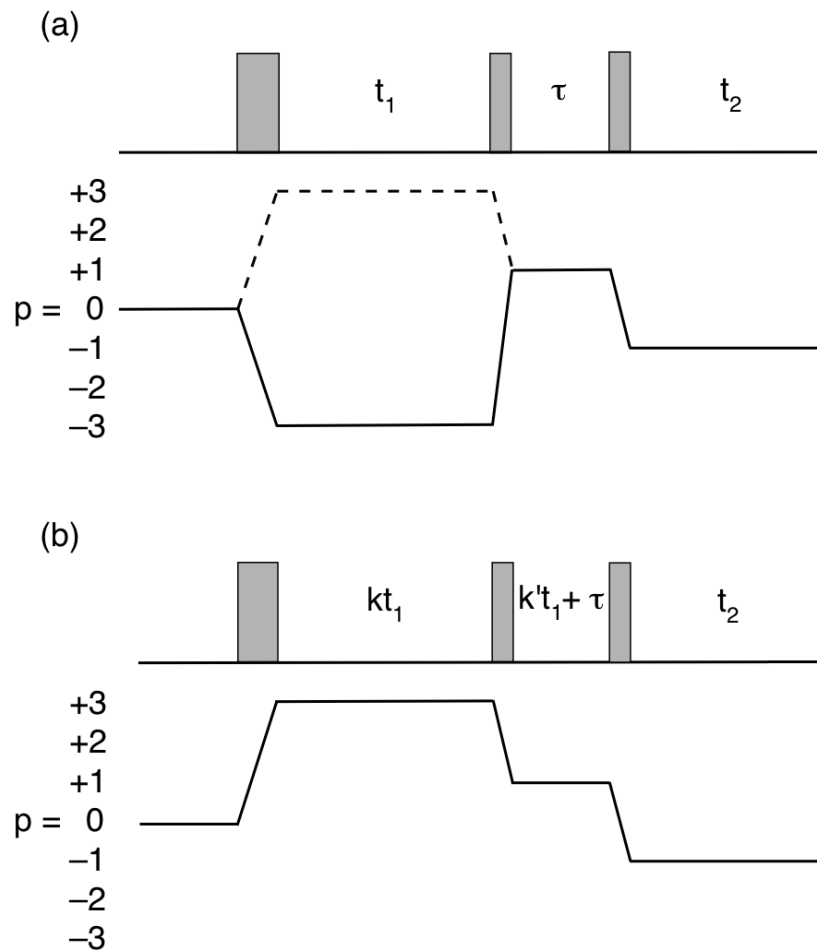


Figure 3.2. Pulse sequence and coherence transfer pathway diagrams for the phase-modulated (a) shifted-echo (solid line) and shifted-antiecho (dotted line) and (b) split- t_1 triple-quantum MAS experiments (for spin $I = 3/2$). Phase cycling is used to select the desired coherence transfer pathway.

along which the ridge lineshape lies in the two-dimensional MQMAS spectrum. The result after appropriate processing of the data in Eqn. (3.9) yields a spectrum in which one (F_1) dimension contains an isotropic spectrum and the other dimension (F_2) contains an anisotropically broadened ridge lineshape [3.5].

Because the signal yielded from this two-pulse MQMAS experiment in Fig. 3.1a (for the phase-modulated experiment) results in a lineshape that is a superposition of two-dimensional absorptive and dispersive lineshapes, such an experiment has not been widely used and different pulse sequences are currently used to obtain high-resolution pure-absorption lineshapes [3.6].

There exist a number of extensions of the basic MQMAS experiments including the amplitude-modulated, shifted-echo (whole-echo) or split- t_1 experiments.

3.2.2. Amplitude-modulated experiments

In 1996, Fernandez and Amoureux [3.7] described an amplitude-modulated MQMAS experiment, which allows achieving a purely absorptive two-dimensional lineshapes. In this method, both echo and antiecho pathways are selected, as shown in Figure 3.1a. A simultaneous evolution of $p = +3$ and $p = -3$ coherence during t_1 period leads to an increase in signal intensity with respect to the phase-modulated experiment performed by Frydman and Harwood. It also results in the loss of sign-discrimination in multiple-quantum coherence evolution period but this can be restored by using the time-proportional phase incrementation (TPPI) [3.8] or States-Haberhorn-Ruben [3.9]

methods. Phase-modulated experiments result if either of the echo or antiecho pathway is selected and amplitude-modulated experiments result if both pathways are retained and have equal amplitudes. However, as for spin $I = 3/2$ nucleus, the equal amplitudes of both pathways can be achieved by the use of a conversion pulse with a flip angle of 90° , for spin $I > 3/2$, on the other hand, there is no flip angle which combines both pathways equally for all crystallites found in a powder sample.

Amoureux *et al.* [3.10] suggested a modification to the amplitude-modulated experiment. They proposed a method, known as a z-filter [3.11,3.12], which allows combining both echo and antiecho pathways with equal amplitude for systems with spin $I > 3/2$. In this method, a conversion to observable single-quantum coherence was performed by using two pulses that proceed via a population state ($p = 0$). Figure 3.1b shows the pulse sequence and coherence transfer pathway for the amplitude-modulated z-filter experiment. The first pulse of the z-filter converts the $p = \pm 3$ coherences to populations with $p = 0$, while the final pulse generates the desired $p = -1$ coherence. A projection orthogonal to the ridges in the two-dimensional spectrum of a z-filtered experiment is normally achieved by first applying a shearing transformation [3.13-3.14].

3.2.3. *Shifted-echo experiments*

An alternative approach invented by Massiot *et al.* [3.15] to obtain pure-phase lineshapes was the "shifted-echo" or "whole-echo" experiment. Figure 3.2a presents the pulse sequence and coherence transfer pathway diagram for this experiment. This pulse sequence differs from the one in Fig. 3.1a only in the insertion of a spin echo into the pulse sequence and the echo interval, τ , by which the echo is shifted forward in t_2 , if the echo pathway is selected. Owing to the shifting of the echo in t_2 , a whole echo is formed for every value of t_1 , rather than the half echo when $t_1 \approx 0$ with original phase-modulated experiment.

In the shifted-echo experiment, when the inhomogeneous broadening dominates the homogeneous broadening [3.15], then the Fourier transform of the time-domain signal of whole echoes containing a real component that is symmetric and an imaginary component which is antisymmetric, yielding a spectrum in which the real part is purely absorptive and the imaginary part is zero. But if the inhomogeneous broadening is not dominant over the homogeneous broadening, the symmetry of the echo is lost and the imaginary part of the lineshape contains dispersive contributions.

3.2.4. *Split- t_1 experiments*

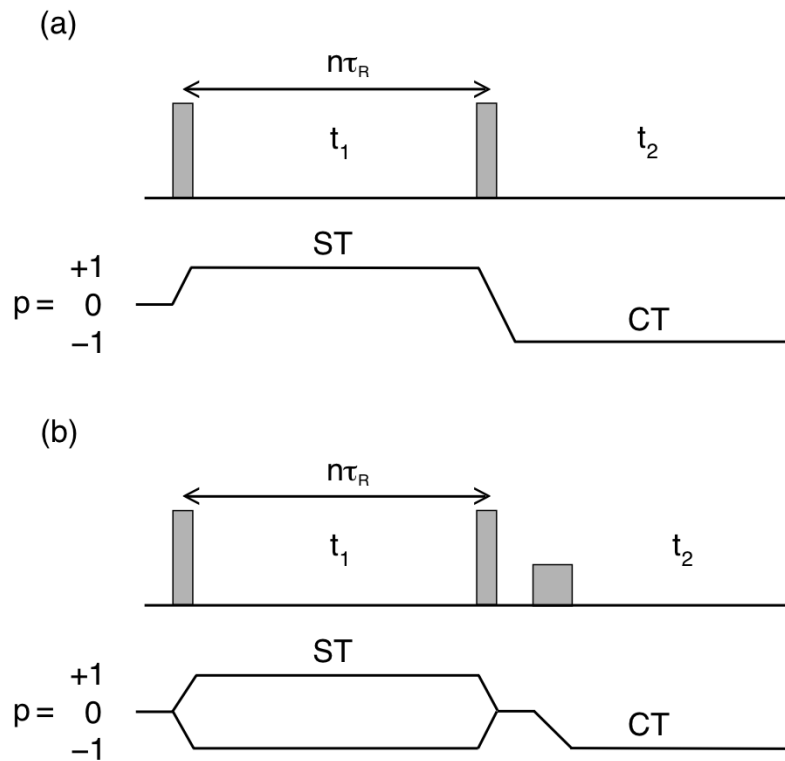


Figure 3.3. Pulse sequence and coherence transfer pathway diagrams for the (a) basic two-pulse, and (b) amplitude-modulated z -filter STMAS experiments. ST designates satellite-transition coherence and CT central-transition coherence.

In the MQMAS experiments described so far, a shearing transformation must be performed to yield a spectrum where the ridges are parallel to the F_2 axis. However, Brown *et al.* [3.12,3.14] proposed a further modification to the MQMAS experiment, which allows obtaining a spectrum in which the ridge lineshapes lie parallel to the F_2 axis after the Fourier transformation. Figure 3.2b presents the pulse sequence and coherence pathway for this approach, for spin $I = 3/2$, known as a "split- t_1 " experiment.

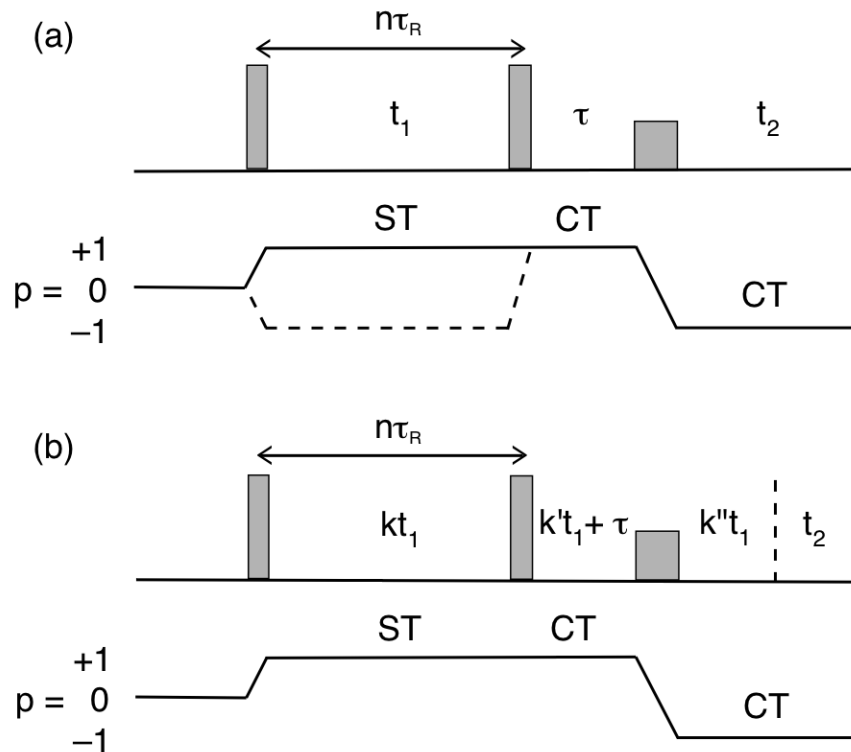


Figure 3.4. Pulse sequence and coherence transfer pathway diagrams for the (a) shifted-echo with the selection of either $p = +1$ (solid line) or $p = -1$ (dotted line) and (b) phase-modulated split- t_1 shifted-echo STMAS experiments. The coherence pathway is selected in t_1 by phase cycling.

The total t_1 period is split into periods of multiple-quantum and central-transition evolution in the ratio of the MQMAS ratio. In such an experiment, all fourth-rank anisotropic broadening are refocussed at the end of the t_1 period resulting in the appearance of the echo at the same position in t_2 , irrespective of the duration of the t_1 evolution period, resulting in an MQMAS spectrum with ridges lying parallel to F_2 .

Many workers have attempted to improve the efficiency of triple- to

single-quantum conversion, with fast-amplitude modulation (FAM) pulses [3.16] or soft-pulse added mixing (SPAM) [3.17] being two of the more promising approaches [3.18].

A large number of applications of the MQMAS technique have appeared in the literature as it is a useful tool for determining structural information. A number of articles have described MQMAS experiments and their applications in more detail [3.19-3.22].

3.3. Satellite-transition MAS NMR

Another technique, in which second-order quadrupolar interactions are removed, is the satellite-transition magic angle spinning (STMAS) experiment, which has also been used for studying dynamics in solids. The STMAS experiment makes use of the fact that, although both the central and satellite transitions are broadened to second order by the quadrupolar interactions, the magnitudes of these broadenings are related by a simple numerical factor. Hence, a correlation of the two transitions in a two-dimensional experiment will allow the removal of the second-order broadening.

The characteristic feature of the STMAS experiment is a requirement of

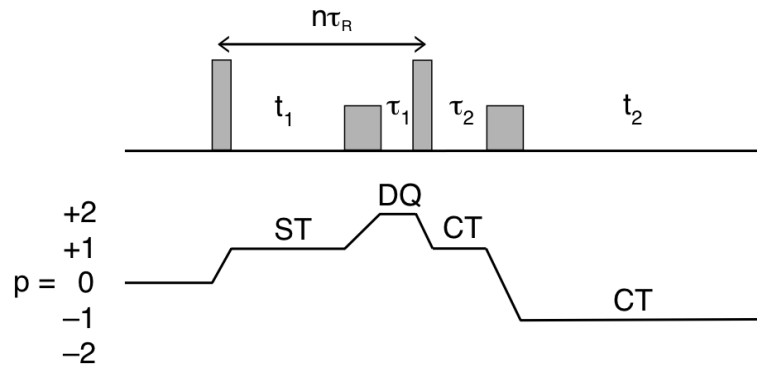


Figure 3.5. Pulse sequence and coherence transfer pathway diagram for a rotor-synchronized double-quantum filtered shifted-echo STMAS (DQF-STMAS) experiment. The second and fourth pulses are selective-inversion pulses for the central transition and hence are applied with low radiofrequency field strength.

very accurate rotor synchronization during the t_1 period as this removes the effects of any second-rank interaction, such as the first-order quadrupolar interaction, and makes all spinning sidebands overlap on top of each other [3.23]. Furthermore, the spinning angle must be also accurately (within $\pm 0.003^\circ$) adjusted to the magic angle (54.736°) to fully remove the anisotropic first-order quadrupolar interaction [3.24].

Figure 3.3a shows the simplest pulse sequence and coherence pathway diagram for the correlation of satellite and central transitions. Satellite transition coherences (ST) are excited with a single pulse and evolve in a rotor-synchronized evolution period t_1 . Then a second pulse converts them into central-transition coherence (CT), which is detected in an acquisition period t_2 .

Spectra that result from the experiment shown in Figure 3.3a contain two-dimensional lineshapes that are "phase twisted", as in the case of the basic two-pulse phase-modulated MQMAS experiment. The typical way to achieve a pure-absorption lineshapes in a two-dimensional STMAS spectrum is to perform amplitude-modulated z-filter experiment, in which echo and antiecho signals are combined with equal amplitude. Figure 3.3b shows a pulse sequence and coherence transfer pathway for this experiment. The last pulse is applied with low radiofrequency field strength, ensuring it is a selective excitation pulse for the central transition [3.10]. The problem with the loss of sign discrimination in the t_1 period may be solved by use of TPPI or the States-Haberhorn-Ruben method.

Another approach to the acquisition of pure-absorption lineshapes is a shifted-echo STMAS experiment, shown in Figure 3.4a. Once again, as in the MQMAS experiment, the τ interval is inserted after the second pulse and a whole echo signal is recorded even when $t_1 = 0$. The τ interval is chosen to be a few milliseconds long. The acquisition of the echo or antiecho signal depends on the selection of the pathway, for example, for spin $I = 3/2$ nuclei the $p = -1$ pathway represents the echo signal and then the fourth-rank anisotropic terms are refocused when $t_2 = \tau + 8/9t_1$.

A modification of the shifted-echo STMAS experiment can be made as previously in the MQMAS experiment in order to obtain two-dimensional spectra with ridges lying parallel to the F_2 axis without the need for a shearing transformation. Figure 3.4b presents the pulse sequence and coherence pathway diagram for a rotor-synchronized split- t_1 shifted-echo experiment. This split- t_1 approach has the same advantage over the z-filter method as in the case of the MQMAS experiment. The t_1 period is split to include evolution of both satellite and central transitions. The relative duration of the t_1 evolution periods is determined by the magnitude of the STMAS ratio, given in Appendix E. The positioning of the second part of the t_1 evolution period, either before or after the last pulse, depends upon the sign of the STMAS ratio [3.24]. When the STMAS ratio is negative, the second evolution period must be placed before the last pulse ($k'' = 0$), whilst if this ratio is positive, the second part of the t_1 evolution period must be placed after the final pulse ($k' = 0$), in order to select the echo pathway. It should be also noted that only the kt_1 period must be set equal to an integral number of rotor periods in order for the satellite-transition evolution period to remain rotor synchronized.

For nuclei with half-integer spin quantum numbers $I > 3/2$, there exist more than one pair of satellite transitions available for correlation with the central transition in an STMAS experiment. For example, for a spin $I = 5/2$

nucleus, there are two distinct sets of satellite transitions ($m_I = \pm 1/2 \leftrightarrow \pm 3/2$ and $m_I = \pm 3/2 \leftrightarrow \pm 5/2$), denoted ST_1 and ST_2 , respectively. Therefore, in addition to the diagonal $CT \rightarrow CT$ autocorrelation peak, a $ST_1 \rightarrow CT$ and a $ST_2 \rightarrow CT$ ridges should be also observed. A double-quantum filtered (DQF-STMAS) method can be used to avoid the appearance of unwanted signals and to simplify the spectrum. Figure 3.5 shows a pulse sequence and coherence transfer pathway for a double-quantum filtered shifted-echo STMAS experiment. In this approach, an additional central-transition selective inversion pulse is employed at the end of the t_1 duration, which effects conversion of inner satellite-transition (ST_1) coherence to double-quantum coherence. As a result, the double-quantum filtered STMAS spectra are free of diagonal and outer satellite-transition peaks and this has benefits when the satellite-transition signal decays rapidly due to motional effects or there is the presence of a distribution of NMR parameters.

It is also possible to refocus fourth-rank anisotropic quadrupolar broadening using transitions other than the single-quantum satellite transition. Double-quantum ($m_I = \pm 1/2 \leftrightarrow \pm 3/2$) satellite transitions may be useful in achieving this refocusing. For example, Kwak and Gan [3.25] described amplitude-modulated z-filtered DQ-STMAS experiment.

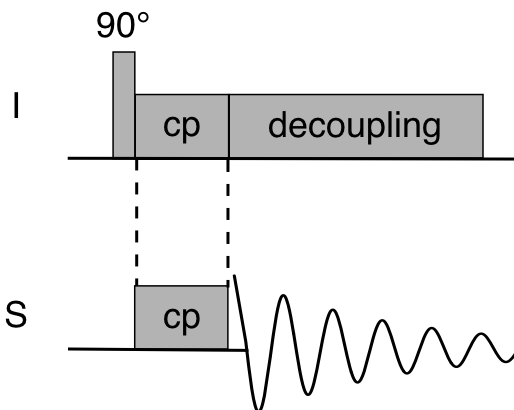


Figure 3.6. Pulse sequence for a conventional cross-polarization experiment.

STMAS experiments are in general subject to first-order broadening and broadening due to motion. Furthermore Dowell *et al.* [3.26] showed that the STMAS approach is able to deliver the same resolution afforded by MQMAS while offering a substantial sensitivity advantage over the MQMAS in the case of low- γ quadrupolar nuclei.

3.4. The cross-polarization experiment

Cross-polarization (CP) is a method used to enhance the magnetization of a low- γ nucleus, such as ^{13}C , by transferring polarization from an abundant high- γ nucleus, such as ^1H or ^{19}F . In this experiment, an initial pulse (90°) on the nucleus I (^1H or ^{19}F) creates transverse I-spin magnetization in the rotating frame, which is then spin-locked by a long period of continuous irradiation applied along the x axis. Simultaneously, a long pulse is also applied to the S

nuclei (eg., ^{13}C), which, in turn, spin-locks the emerging cross-polarized S-spin magnetization. The acquisition of the S-spin free induction decay follows, often with decoupling of the I-spin nuclei, as shown in Figure 3.6.

Cross-polarization from $I = 1/2$ nuclei to quadrupolar nuclei, such as ^2H , ^{11}B or ^{27}Al is more complex but has been also demonstrated. One of the variants of the CP experiment is the combination of the cross-polarization technique and the MQMAS experiment [3.27,3.28].

3.5. Insensitive Nuclei Enhanced by Polarization Transfer (INEPT) experiment

One of the most popular pulse sequences for achieving a signal enhancement of low- γ nuclei is called Insensitive Nuclei Enhanced by Polarization Transfer (INEPT). Figure 3.7 shows the basic INEPT pulse sequence introduced by Morris and Freeman in 1979 for solution-state NMR [3.29]. Broadly speaking, the first part of the pulse sequence is a spin-echo sandwich. The spin echo retains evolution under the J coupling, J_{IS} , and spin magnetization I evolves into a purely anti-phase state. The last 90° pulses transfer the anti-phase state from I to S. As a result, a spectrum with anti-phase multiplets is observed. Furthermore, a maximum signal intensity for two

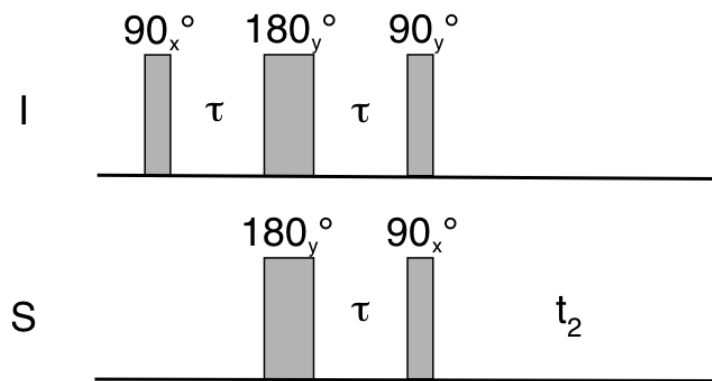


Figure 3.7. Pulse sequence for INEPT experiment. The narrow rectangles represent 90° pulses, while the broad rectangles represent 180° pulses.

coupled spin $I = 1/2$ nuclei is obtained when τ is chosen to be equal to $1/4J_{IS}$. However, if broadband decoupling on spin I is employed immediately after the 90° pulse, cancellation of the anti-phase multiplets occurs and no signal is observed [3.30].

Experiments can also be carried out with the refocused INEPT (RINEPT) pulse sequence [3.31]. The RINEPT pulse sequence is identical to that of the basic INEPT experiment, apart from the addition of an echo sequence after the transfer pulses and before the acquisition [3.32]. This allows refocusing of the anti-phase multiplets and, hence, acquisition of a decoupled S-spin spectrum. Figure 3.8 shows the RINEPT pulse sequence.

In solid-state NMR spectroscopy, the INEPT technique was first

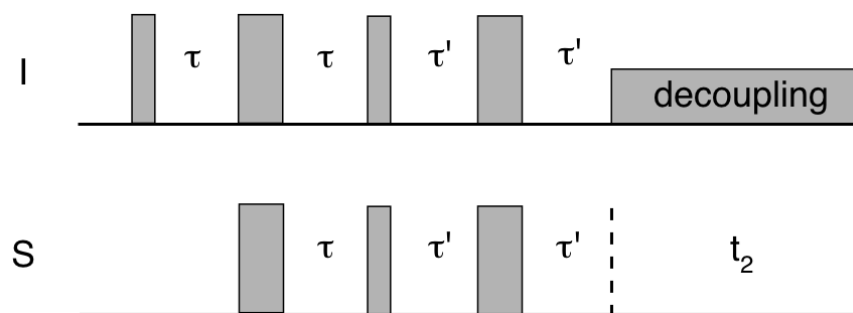


Figure 3.8. Pulse sequence for refocused INEPT (RINEPT) experiment. The narrow rectangles represent 90° pulses, while the broad rectangles represent 180° pulses.

introduced under MAS for through-bond transfers between weakly coupled nuclei in inorganic materials [3.33]. One of the variant of the INEPT-based pulse sequences is the double-INEPT pulse sequence, described below.

3.5.1. Double-INEPT

An alternative approach to the INEPT experiment, which was used in this work in the case of carboranes to excite triple-quantum coherence, is an approach based on the methods of Yen and Weitekamp [3.34] and Müller [3.35]. Figure 3.9 presents the pulse sequence, which is identical to that of the heteronuclear single-quantum correlation (HSQC) [3.36] experiment widely used in solution-state NMR spectroscopy but with a different coherence transfer

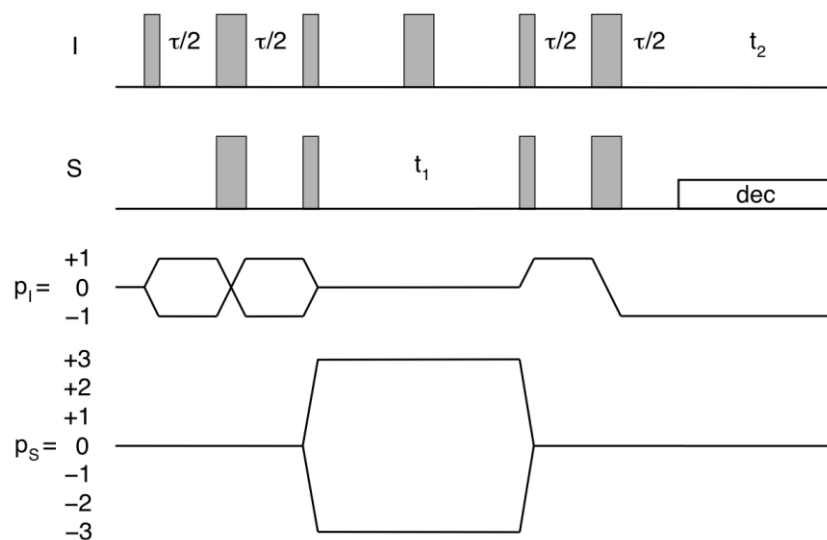


Figure 3.9. Pulse sequence and coherence transfer pathway diagram for a double-INEPT experiment. The narrow rectangles represent 90° pulses, while the broad rectangles represent 180° pulses.

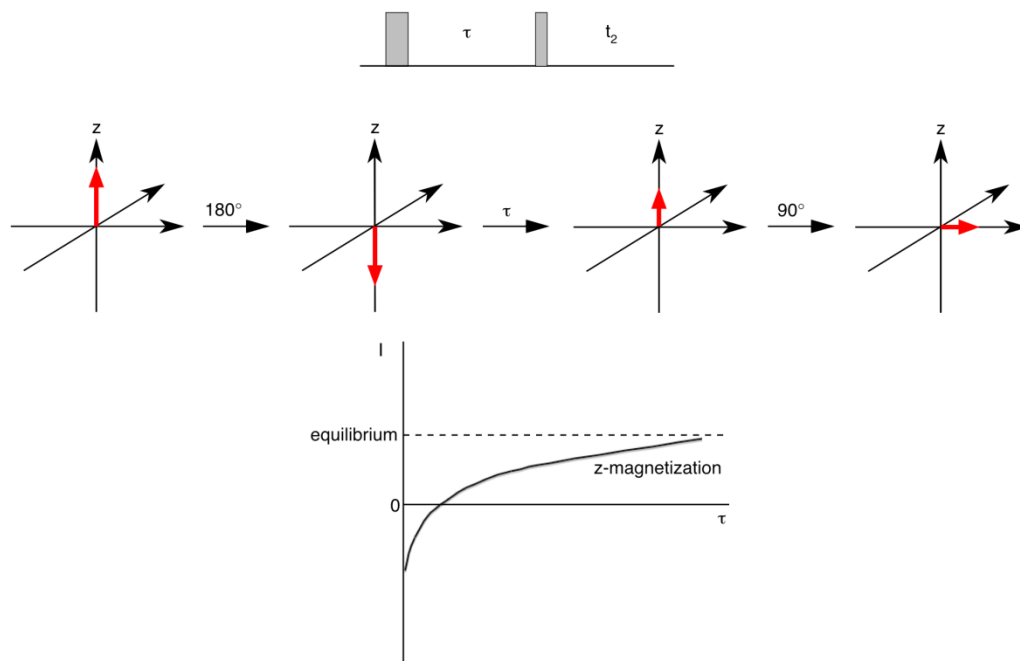
pathway. Although the HSQC term suggests an experiment with excitation of only a single-quantum coherence, Kemp-Harper *et al.* [3.37] discuss its application to a coupled $I = 1/2$, $S = 3/2$ system to excite S-spin multiple-quantum coherences in solution. The experiment name used in this work is the double-INEPT suggested in Ref. 41, as two INEPT pulse sequence elements are used. In the first step, I-spin anti-phase magnetization is created, which is then transferred to the heteronucleus, S. The magnetization of spin S is left to evolve during the time period t_1 . The I-spin coupling and chemical shift effects are removed by a 180° pulse applied midway through t_1 . A 90° pulse is then applied simultaneously to both nuclei at the beginning of the second INEPT step. This transfers the anti-phase magnetization back to the spin I, which is

then refocused over the second time period τ . The I-spin in-phase magnetization is then detected during t_2 in the presence of spin decoupling.

3.6. Spin-lattice relaxation time measurements

Relaxation is the process by which, over time, the bulk magnetization returns to its equilibrium position. The process by which the z-magnetization is returned to its equilibrium value is called longitudinal (spin-lattice) relaxation (T_1). In other words, the spin-lattice relaxation time characterizes the rate at which the longitudinal M_z component of the bulk magnetization vector recovers to its equilibrium state (the Boltzmann distribution). The process by which transverse magnetization decays away to its equilibrium value of zero is called transverse relaxation (T_2). In this thesis only spin-lattice relaxation will be discussed.

The T_1 (spin-lattice) relaxation time is normally measured using the "inversion recovery" method. Figure 3.10 shows the inversion recovery pulse sequence, the behaviour of the magnetization vector \mathbf{M} after the first pulse and during a time interval, τ , and a graph of the intensities I plotted against τ showing how relaxation drives the z-magnetization to its equilibrium. This experiment consists of two non-selective radiofrequency pulses and a variable



time interval, τ , during which the inverted magnetization vector \mathbf{M} recovers

Figure 3.10. Pulse sequence for an inversion recovery experiment, behaviour of magnetization vector \mathbf{M} , and schematic graph of the intensities I plotted against τ . The red arrows represent the magnetization vector \mathbf{M} . The narrow rectangle represents a 90° pulse, while the broad rectangle represents a 180° pulse.

back to equilibrium. Application of a 180° pulse aligns the magnetization vector along the (negative) z -axis. After the 180° pulse the magnetization vector will gradually decay along the $+z$ axis with increasing τ due to spin-lattice relaxation. The 90° pulse then rotates \mathbf{M} into the xy -plane. Once in the xy -plane, \mathbf{M} precesses about the z -axis, yielding a free induction decay, which is recorded and Fourier transformed to give an NMR spectrum with peaks of intensity I proportional to M_z . In this example, the T_1 relaxation is an exponential process:

$$M_z(\tau) = M_0(1 - 2\exp(-\tau / T_1)) \quad (3.7)$$

Therefore if we plot $\ln(I_\infty - I_\tau)$ against τ then a straight line of slope T_1 may be obtained and the T_1 value extracted.

It is important to know that an interval of five times the magnitude of the spin-lattice relaxation time of the material is usually used to ensure that the spins have enough time to reach thermal equilibrium before the next 180° pulse for variable τ . Typical dipolar T_1 values for protons can be between 0.1 and 10 seconds, whereas for solids T_1 can be of the order of minutes.

Chapter 4: Second-order quadrupolar shifts as an NMR probe of fast molecular-scale dynamics in solids

4.1. Dynamics in solids

4.1.1. Introduction

There is currently much interest in the investigation of molecular motion in solids. NMR spectroscopy is an excellent and well established technique for studying the dynamics in liquids and solids. In recent years, dynamic NMR methods have been applied successfully in liquids as well as in solid materials and a huge advantage of these NMR methods is the large range of dynamic timescales that can be covered.

Three basic timescale ranges can be distinguished, as presented in Fig. 4.1, which depend on the particular system and magnetic interaction: the slow molecular motion range with correlation times $\tau_C > 10^{-3}$ s; the intermediate molecular motion range with 10^{-9} s $< \tau_C < 10^{-3}$ s; and the fast molecular motion

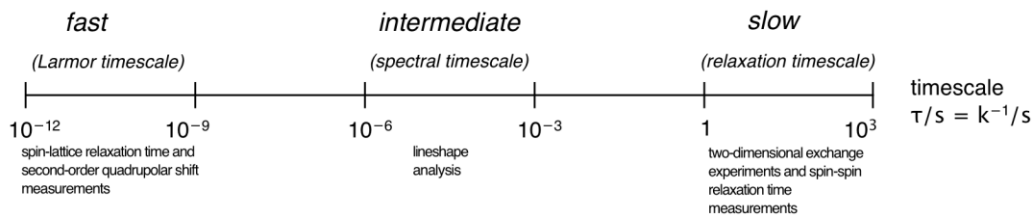


Figure 4.1. Motional timescales and the associated NMR methods for studying dynamics.

range with correlation times of the order of a nanosecond or less, where the correlation time, τ_C , is defined as the average time it takes for a molecule to end up at an orientation about one radian from its starting position.

The three ranges can be referred to as the relaxation, spectral and Larmor timescales, respectively, and may be studied via various types of NMR methods and experiments. Two-dimensional exchange and spin-spin relaxation time experiments can be used to study relatively slow motional processes. Motions with inverse correlation times of the order of the nuclear spin interaction anisotropy can be assessed via lineshape analysis. Spin-lattice relaxation time measurements are the usual method to investigate fast molecular reorientation but in this chapter I will show that multiple-quantum NMR measurements of isotropic quadrupolar shifts are also a simple way to probe nanosecond timescale motions in solids.

4.1.2. Slow-timescale motion – the two-dimensional exchange experiment

Two-dimensional exchange spectroscopy is invaluable for studying slow dynamic processes. There is a considerable literature about exchange experiments [4.1-4.3]. Figure 4.2 shows the basic pulse sequence for this method. After an initial non-selective 90° pulse, magnetization is created and, in the case of symmetrical two-site chemical exchange between two species A and B of equal concentrations and assuming equal spin-lattice relaxation rates and equal transverse relaxation, the transverse magnetization components during the t_1 (evolution) period are given by:

$$M_A(t_1) = M_{A0} \exp(i\omega_A t_1 - t_1 / T_2) \quad (4.1)$$

$$M_B(t_1) = M_{B0} \exp(i\omega_B t_1 - t_1 / T_2) \quad (4.2)$$

where M_{A0} and M_{B0} are equilibrium magnetizations.

When a second pulse with the same phase as the first one is applied, the longitudinal magnetization stored along z (the direction of the applied magnetic field) at $\tau_m = 0$ is created:

$$M_{zA}(t_1) = -M_{A0} \cos \omega_A t_1 \exp(-t_1 / T_2) \quad (4.3)$$

$$M_{zB}(t_1) = -M_{B0} \cos \omega_B t_1 \exp(-t_1 / T_2) \quad (4.4)$$

The z components migrate from one site to another due to chemical exchange for a period τ_m , the mixing time. Spin-lattice relaxation attenuates the magnetization at the same time. The magnetization at the end of the mixing period is given by:

$$\begin{aligned} M_{zA}(\tau_m) &= M_{zA}(t_1) \frac{1}{2} [1 + \exp(-2k\tau_m)] \exp(-\tau_m / T_1) + \\ M_{zB}(t_1) &\frac{1}{2} [1 - \exp(-2k\tau_m)] \exp(-\tau_m / T_1) \end{aligned} \quad (4.5)$$

$$\begin{aligned} M_{zB}(\tau_m) &= M_{zA}(t_1) \frac{1}{2} [1 - \exp(-2k\tau_m)] \exp(-\tau_m / T_1) + \\ M_{zB}(t_1) &\frac{1}{2} [1 + \exp(-2k\tau_m)] \exp(-\tau_m / T_1) \end{aligned} \quad (4.6)$$

where k is an exchange rate ($k = k_{AB} = k_{BA}$).

The final 90° pulse converts these longitudinal components into observable magnetization. After two-dimensional Fourier transformation the resulting two-dimensional spectrum is observed, correlating the characteristic frequency the spin had during t_1 period with that which it subsequently had in t_2 .

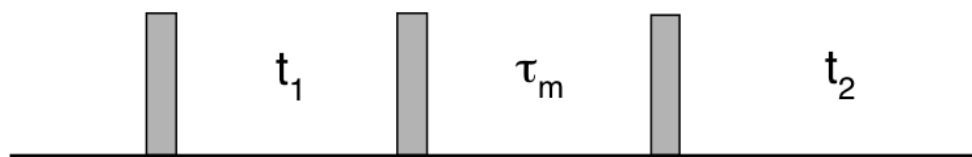


Figure 4.2. The basic pulse sequence for two-dimensional exchange experiment to study motion.

If there is no exchange during the τ_m period, only diagonal peaks appear in the spectrum. The existence of cross-peaks corresponds to chemically exchanging species because it means that the offset frequency after τ_m is different from the initial one. This is sufficient proof that a dynamic exchange process is taking place in the sample. Furthermore the cross-peak amplitudes are dependent on the length of the mixing time and can provide a quantitative estimate of the exchange rate.

Jeener *et al.* [4.3] demonstrated the use of two-dimensional NMR spectroscopy as a method for the investigation of chemical and magnetic rate processes in solution- and solid-state NMR and they described in detail how this two-dimensional exchange experiment is applicable to slow motions. Cahill *et al.* [4.4] investigated lithium dynamics in monoclinic $\text{Li}_3\text{V}_2(\text{PO}_4)_3$ through variable-temperature ^7Li magic-angle spinning (MAS) NMR spectra and exchange-based solid-state NMR studies. Two-dimensional exchange NMR

spectroscopy has also been used to probe mobility in fluoride-ion conductors such as α -PbF₂ and BaSn-F₄. [4.5,4.6]. Recent studies have demonstrated the use of ¹⁷O and ⁶Li 2D EXSY to study ion motion in conductors Bi₂WO₆ and Li₇MnN₄, respectively. [4.7,4.8]

4.1.3. Intermediate-timescale motion – lineshape analysis

In the case of intermediate molecular motion (on the spectral timescale), NMR spectra may exhibit characteristic lineshape effects. A powder pattern can be considered as being made up of an infinite number of overlapping sharp lines, arising from each different molecular orientation present in the sample. Therefore, any motion that changes the orientation of a molecule influences each resonance line and causes a distortion of the powder pattern which depends on the correlation time, the geometry of the molecule and, in the case of MAS NMR spectra, on the spinning rate. By simulating these effects and fitting the corresponding spectra it is possible to obtain detailed information about the mechanism of molecular motion.

As mentioned previously, the intermediate molecular motion regime includes processes with a correlation time τ_c being between 1 ms and 1 ns. Because of the wide range on the timescale, we can distinguish between two

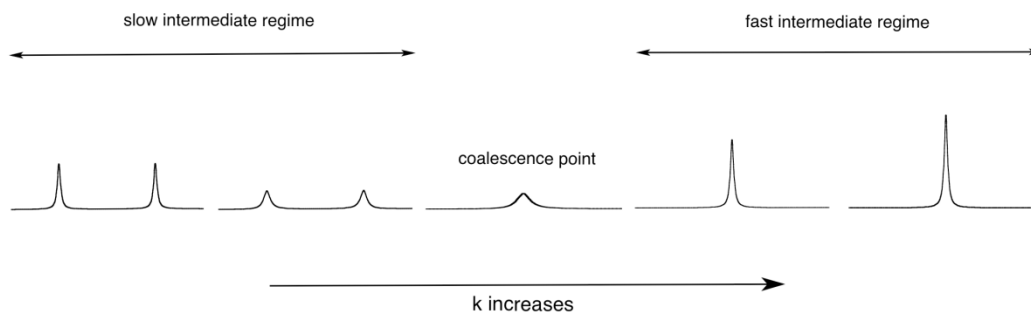


Figure 4.3. Spectra for two-site exchange, in intermediate (slow and fast) exchange regime.

different sub-regimes. There is a slow intermediate regime where the rate constant is slower than half of the width of the powder pattern (in other words half of the frequency difference between the two peaks) and where motional broadening is observed. The second sub-regime is the fast intermediate regime where the correlation time is much greater than the nuclear spin anisotropy, corresponding to a rate constant faster than half of the width of the powder pattern, and where motional narrowing takes place. In the slow intermediate range, if the rate constant increases, the decay of the FID is faster, leading to broader NMR peaks until a "coalescence point" is reached. At that point the rate constant is approximately equal to half of the frequency difference between two lines. On the other hand, in the fast intermediate regime, the decay of the total transverse magnetization gets slower as the rate of molecular reorientation increases, reducing the NMR peak width. The effect described above, using the example of symmetric two-site exchange, is shown graphically in Figure 4.3.

Since NMR has long played an important role in the study of molecular motion in the solid state, there are a lot of published studies, with the earliest dating from the 1950s [4.9,4.10]. The first studies of dynamics in the solid state relied, in general, on the analysis of powder lineshapes obtained from static samples, presenting low-resolution spectra. Further discoveries in solid-state NMR, such as the MAS experiment, described in Chapter 3, have made available high-resolution spectra and thus allow the possibility for much more detailed analysis of molecular motion in solids on the spectral timescale. The effect of molecular reorientation on the lineshape in MAS spectra was first discussed quantitatively by Maricq and Waugh [4.11]. They explained how the MAS technique fails in the presence of dynamic reorientation and this in turn causes an increase in the linewidth.

One piece of evidence for dynamics is a motional broadening of quadrupolar satellite-transition spinning sidebands. As pointed out in Chapter 3, the intensities of spinning sidebands are dependent on the motional process in the sample. The important point is that spinning sidebands patterns are sensitive only to motions on the order of the width of the spinning sideband patterns (i.e., on the μs timescale) and they are dependent on the spinning rate and nuclear spin anisotropy. The effect of molecular reorientation on rotational echoes is shown in Figure 4.4. Ashbrook *et al.* [4.12] presented the influence of

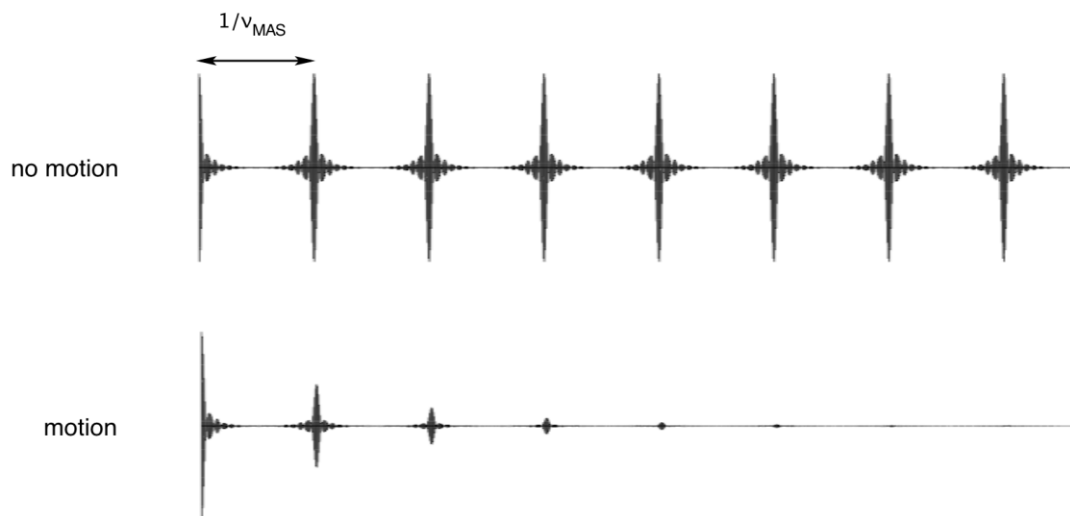


Figure 4.4. The effect of dynamics on rotational echoes in a MAS experiment. Rotational echoes form when magnetization vectors from individual crystallites come back into phase. Molecular reorientation results in decreased intensity of successive rotational echoes.

dynamic reorientation on STMAS spectra by comparing them with MQMAS spectra in ^{17}O ($I = 5/2$) NMR spectroscopy of two materials, chondrodite ($2\text{Mg}_2\text{SiO}_4 \cdot \text{Mg}(\text{OH})_2$) and clinohumite ($4\text{Mg}_2\text{SiO}_4 \cdot \text{Mg}(\text{OH})_2$). Antonijevic *et al.* have used this method later for investigation of dynamics on the μs timescale in the aluminophosphate material AlPO-14 [4.13]. Furthermore, these authors have introduced a simple model to illustrate and quantify the effect of dynamics on linewidths in MAS NMR spectra and, in 2008, Thrippleton *et al.* presented its wider application and fully justified the use of this model [4.14].

The most detailed investigations of molecular motion have involved ^2H NMR experiments. Some papers have discussed both theoretically as well as

experimentally a number of examples of how molecular motion may influence the ^2H NMR lineshape [4.15,4.16]. The methodology has been developed for both non-rotating and rotating samples and the simulations may involve different models of molecular motion.

There are several advantages of using deuterium. The low natural abundance makes selective enrichment possible in many molecular systems. The deuteron is a spin $I = 1$ nucleus that usually has a relatively small quadrupolar coupling and thus experiments are feasible for most systems, while the ^2H line broadening is sensitive to motion on the microsecond timescale. Because the ^2H quadrupolar interaction is determined by the local electron distribution, the spectra are often readily interpretable in terms of the geometry of the molecular system.

The ^2H lineshape can be obtained using the quadrupolar-echo experiment [4.17] as discussed by Davis *et al.* [4.18] in their investigation of phospholipid hydrocarbon chains. Powder NMR spectra of static samples consist of doublet patterns, the doublet arising from the two possible spin transitions (spin $I = 1$, $m_I = \pm 1 \sqrt{0}$). These spectra are often called Pake patterns with the splittings between the perpendicular edges of the powder patterns equal to $(3/4)C_Q$, where C_Q is the deuterium quadrupole coupling constant

defined in Eqn. (2.34). Jelinski *et al.* [4.14] have used ^2H NMR spectroscopy to elucidate two distinct motional regions in copolymers of selectively deuterated poly(butylene terephthalate) (PBT) and poly(tetramethyleneoxy terephthalate) (PTMT). Specifically, the PBT hard segments are characterized by a broad line pattern that arises as a result of limited molecular motion. However, the PTMT amorphous phase undergoes more extensive motion, as was indicated by an extreme narrowing of the deuterium spectrum.

^2H NMR spectroscopy has become one of the most useful methods in studying intermediate-timescale motion and is described in more detail by Duer *et al.* [4.20]. Cutajar *et al.* [4.21] used ^2H double-quantum MAS NMR experiment as a potential technique to probe molecular motion in the intermediate motional regime for investigations of oxalic acid dihydrate- d_6 , sodium tetrathionate dihydrate- d_6 and poly(methyl methacrylate- d_8) (PMMA). Solid-state ^2H NMR spectroscopy has been also used to probe the dynamic disorder of hydroxyl deuterons in a synthetic sample of deuterated hydroxyl-clinohumite ($4\text{Mg}_2\text{SiO}_4 \cdot \text{Mg}(\text{OD})_2$). [4.22]

Other applications of ^2H NMR spectroscopy, not only in studies of dynamics, are discussed in Ref. 4.23-4.26.

4.1.4. Fast-timescale motion – spin-lattice relaxation time and second-order quadrupolar shift

Spin-lattice relaxation time measurements

Measurement of spin-lattice relaxation rates can provide information on faster motions, which are inaccessible through quadrupolar-echo lineshapes. Longitudinal relaxation was explained in Chapter 3 and here it will be shown that the spin-lattice relaxation time, T_1 , is a useful source of information on molecular dynamics and is sensitive to motions with rates near the Larmor frequency.

The motion of a molecule can be characterized by a correlation time, τ_c , defined previously. Small molecules tumble very rapidly and therefore have short τ_c , while large molecules tumble slowly and therefore have long τ_c . It means that the correlation times for solutions, where rapid tumbling is present, are often very short and the condition $\omega_0\tau_c \ll 1$ is satisfied. This condition is known as *extreme narrowing limit*. On the other hand, in solids, where there is a high degree of restricted motion, the correlation times are much longer than for liquids and the condition, known as the *slow motion limit*, where $\omega_0\tau_c \gg 1$, is satisfied. When the motion has a correlation time about equal to about $1/\omega_0$ the

spin-lattice relaxation is most efficient.

In summary, spin-lattice relaxation times are a sensitive probe of molecular motion within a molecule. Analysis of relaxation times can tell us whether a given chemical environment is in a rigid portion of the molecule or in a flexible part of the molecule.

Because the motional frequency can range from ten to hundreds of MHz, spin-lattice relaxation experiments can be used to provide dynamic, structural and morphological information about many types of systems. T_1 values are particularly sensitive to high-frequency side-chain motion, as was found by Edzes and Veeman in their studies of the effects of plasticizers on the spin lattice relaxation of carbon nuclei in solid poly(methyl methacrylate) (PMMA) [4.27]. Koenig *et al.* [4.28] have used T_1 spin-lattice times to characterize the motional difference between α and β phases of poly(buteleneterephthalate). Schaefer *et al.* [4.29], in turn, have shown that T_1 values can be used to study the effect of thermal history on molecular motion in solid polymers. Measurement of this spin-lattice relaxation rate anisotropy has been also used in the case of ^2H NMR in model membrane systems [4.30,4.31].

These and other examples represent important applications of spin-

lattice relaxation experiments in the investigation of dynamic behaviour in a variety of systems.

Second-order quadrupolar shift

The coupling between the nuclear quadrupole moment and the electric field gradient across the nucleus results in an anisotropic interaction of spatial rank two, conventionally parameterised by a coupling constant C_Q and an asymmetry η . In high-field NMR, this quadrupolar interaction can be treated using average Hamiltonian theory. The second-order correction to the dominant Zeeman Hamiltonian can be decomposed into three terms, with spatial ranks zero, two and four as shown in Eqn. (2.38). The second- and fourth-rank terms result in an inhomogeneous line-broadening, while the rank zero term causes the well known isotropic quadrupolar shift as shown in Section 2.4 [4.32,4.33].

Since the average Hamiltonian is obtained by averaging over the Larmor period, the effect of molecular-scale dynamics on the quadrupolar shift depends on the timescale of any motion compared with the Larmor period. In the case of motion that is much slower than the Larmor frequency ν_0 , the average Hamiltonian expansion remains valid and the spectrum can be determined by

calculating the time-averaged second-order Hamiltonian. Thus, if the motional rate constant is significantly larger than the second-order parameter $2\pi C_Q^2/\nu_0$ (but still much smaller than $2\pi\nu_0$), the second- and fourth-rank terms are averaged and, in the case of isotropic motion, are reduced to zero. The zeroth-rank term, however, is orientation independent and unaffected by motion on this timescale; the isotropic quadrupolar shift is therefore unaffected [4.34].

In the opposite case, where motion is much faster than the Larmor precession, the effect of orientational averaging must be assessed *before* the average Hamiltonian is calculated. This means that both the second-order broadening and the isotropic quadrupolar shift are affected and, since the full quadrupolar Hamiltonian is second rank, rapid isotropic motion averages both to zero. Molecular-scale tumbling on the nanosecond timescale or faster can therefore have a measureable influence on the centre-of-gravity shifts of quadrupolar nuclei. This effect has been extensively studied in solution, where it is commonly referred to as the "dynamic shift" [4.35-4.38]. As pointed out by Werbelow and London [4.38], however, the phenomenon is better described as a quenching of the isotropic second-order quadrupolar shift by rapid tumbling. In solids, in contrast, this quenching effect is less well known, although temperature-dependent isotropic quadrupolar shifts have been observed, especially in single-crystal and static-powder NMR studies of ionic conductors

[4.39-4.41].

4.2. *Closo* - carboranes

4.2.1. *Introduction*

The *closo*-carborane molecules $C_2B_{10}H_{12}$ and their derivatives have attracted widespread interest because of their chemical properties. They form so-called "plastic crystals". In plastic crystals, molecules are arranged within a lattice, but are free to re-orientate. The *closo*-carborane molecules $C_2B_{10}H_{12}$ approximate regular icosahedra of CH and BH units and exist as three structural isomers. The isomers (shown in Fig. 4.5) are the *ortho* (OCA), *meta* (MCA) and *para* (PCA) isomers. The carbon atoms in OCA, MCA and PCA are separated by one, two and three bonds respectively. The highest temperature phase occurs above 275 K for OCA, 285 K for MCA and 300 K for PCA; X-ray diffraction studies of OCA and MCA reveal a face-centred cubic lattice for this phase. This is a plastic-crystalline phase, in which the molecular reorientation is rapid and isotropic and the NMR spectra are narrow and liquid-like. Below this temperature, there is a phase where the symmetry of the lattice is reduced, probably to orthorhombic symmetry for OCA and MCA. Rapid molecular reorientation continues but is thought to be anisotropic. At even lower

temperatures (below 160-200 K for OCA, 170 K for MCA and 238 K for PCA) less well characterized phases exist in which the motion of the molecules is reduced [4.42,4.43]. Following the literature, this chapter will refer to the high, medium and low temperature phases as I, II and III, respectively.

The carboranes are ideal models for studying reorientation in solids. The carboranes contain boron atoms, which may be conveniently studied by ^{11}B NMR. ^{11}B has spin $I = 3/2$ and hence is sensitive to electric field gradients. Although a number of NMR studies exist in the literature, many of these are over 20 years old and therefore do not exploit modern NMR methods, such as magic angle spinning (MAS) and multiple-quantum MAS (MQMAS). This chapter will show that these and other techniques provide a clear window on the structure and dynamics of the carboranes.

4.2.2. Results and discussion

Since the reorientation is thought to be isotropic at high temperature and anisotropic at low temperatures, the first step of the investigation was to record one-dimensional ^{11}B MAS NMR spectra at a variety of temperatures to observe how the lineshapes and shifts change with temperature.

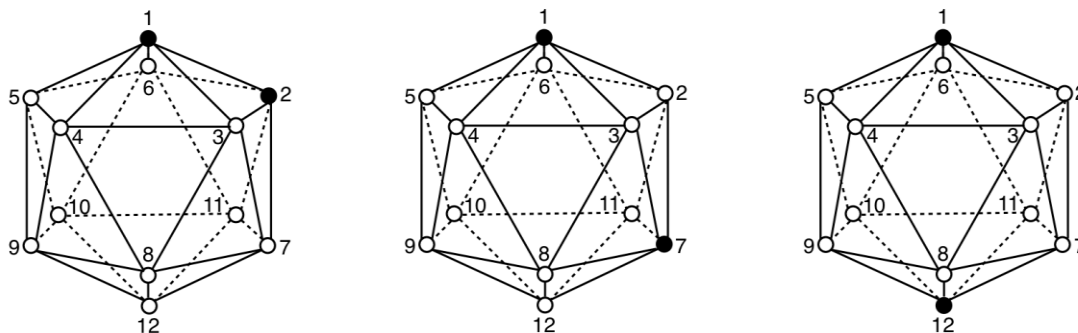


Figure 4.5. Chemical structure of the (a) *ortho*, (b) *meta* and (c) *para* isomers of the *closo*-carborane molecules $C_2B_{10}H_{12}$. The boron (white circles) and carbon atoms (black circles) form an icosahedron. Hydrogen atoms have been omitted.

Figures 4.6, 4.7 and 4.8 show ^{11}B MAS spectra of the three carborane isomers, recorded as a function of temperature. The number of peaks observed is equal to the number of unique boron environments for each isomer, and the peaks in one-dimensional ^{11}B MAS spectra have been assigned by comparison with solution-state NMR data [4.44]. ^{11}B MAS spectra of none of the investigated carboranes exhibit second-order quadrupolar powder patterns. The high-temperature carborane spectra resemble liquid-state NMR spectra and are thus consistent with the assumption of molecules undergoing rapid isotropic reorientation.

The ^{11}B linewidth increases with decreasing temperature for all three isomers and, below the I-II phase transition, the spectra of all three isomers exhibit significantly broader lines (OCA: ~ 600 Hz, MCA: 500–1000 Hz, PCA:

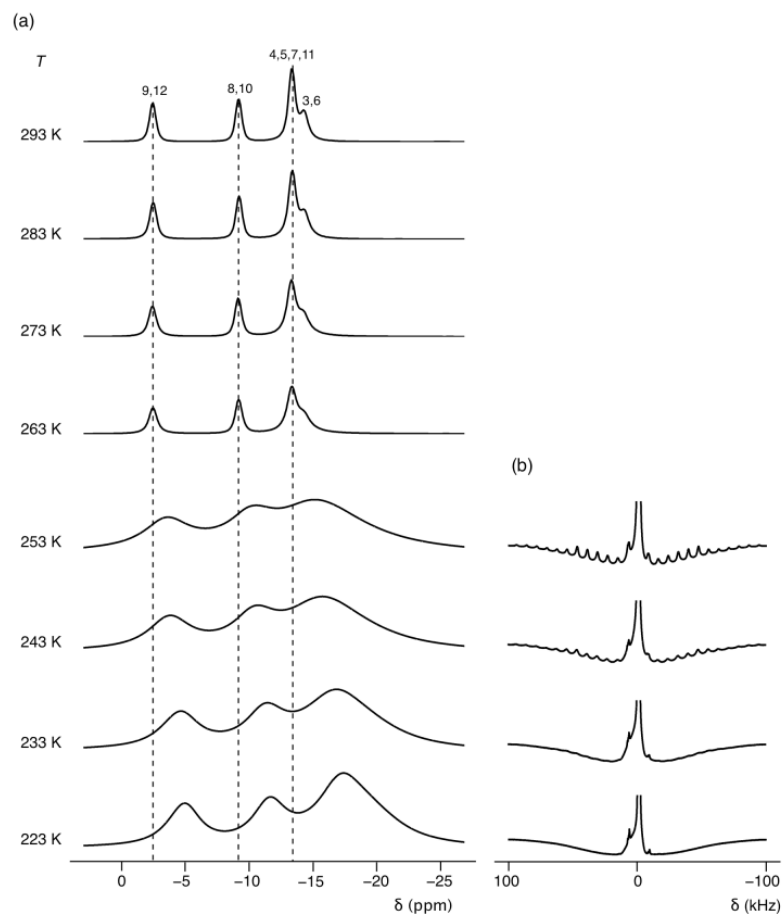


Figure 4.6. (a) Variable-temperature ^1H -decoupled ^{11}B MAS NMR spectra of OCA and (b) ^1H -decoupled ^{11}B MAS NMR spectra of the low temperature phase of OCA recorded using a wide spectral width. The ^{11}B radiofrequency field strength was between 145 and 165 kHz (90° pulse duration of 1.5–1.75 μs), while ^1H decoupling was applied with a field strength of ~ 50 kHz. The recycle interval (in the range 1–4 s) was optimised to ensure that the samples were fully relaxed prior to excitation. Spectra are the result of averaging 8 transients.

~ 1200 Hz). This is consistent with the transition to a more solid-like phase, where molecular reorientation is anisotropic and/or slower, so that the broadening interactions are not fully averaged. Temperature also affects the frequencies of the peaks. For OCA, a shift of the four main peaks to low frequency is observed, which increases as the sample is cooled to lower

temperatures at the I-II transition, while for MCA and PCA the change occurs more gradually below the phase transition. The frequency changes are likely to be due to “dynamic shift” effects, rather than changes in the chemical shift as will be proved later.

Figures 4.6b, 4.7b and 4.8b show that for all three isomers, very little spinning sideband intensity is apparent in phase I and the few sidebands observed are likely to result from shimming imperfections or susceptibility effects. This is consistent with rapid isotropic motion, which averages out the quadrupolar interaction and causes the satellite-transition signal to be concentrated in the centreband. Below the I-II phase transition temperature, many more spinning sidebands appear, spanning approximately 300 kHz for OCA and MCA and 80 kHz for PCA, consistent with more anisotropic motion, resulting in incomplete averaging of the quadrupolar interaction. It is interesting to note that the spinning sidebands pattern for PCA is significantly narrower than for the other two isomers. This observation is consistent with rapid anisotropic reorientation about the C_5 symmetry axis, which would average the quadrupolar coupling constant to a small fraction of its intrinsic value; alternatively, the reorientation may simply be more isotropic in PCA.

A further point to note in Figs. 4.6b, 4.7b and 4.8b is that the spinning

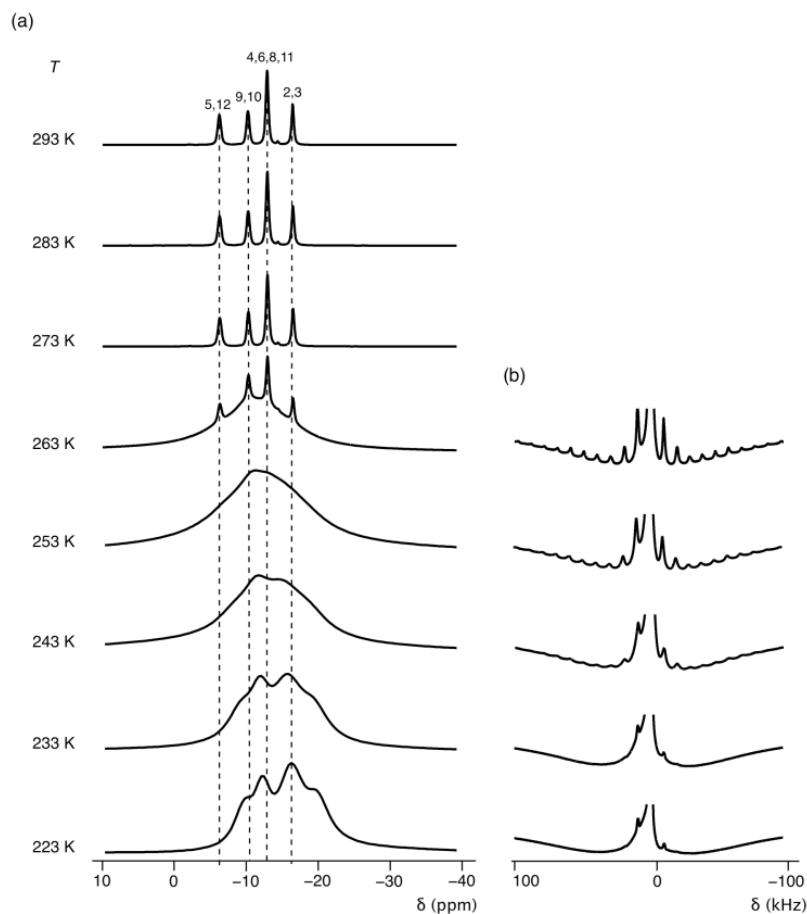


Figure 4.7. (a) Variable-temperature ^1H -decoupled ^{11}B MAS NMR spectra of MCA and (b) ^1H -decoupled ^{11}B MAS NMR spectra of the low temperature phase of MCA recorded using a wide spectral width. The ^{11}B radiofrequency field strength was 165 kHz (90° pulse duration of 1.5 μs), while ^1H decoupling was applied with a field strength of ~ 50 kHz. The recycle interval (in the range 1–4 s) was optimised to ensure that the sample was fully relaxed prior to excitation. Spectra are the result of averaging 8 transients.

sidebands increase in width as the temperature is reduced, until they disappear into the baseline. A motional broadening of quadrupolar satellite-transition spinning sidebands was explained in one of the previous subsections and this is likely to be the result of motional broadening, which causes the linewidths to increase as the rate of reorientation approaches the size of the quadrupolar

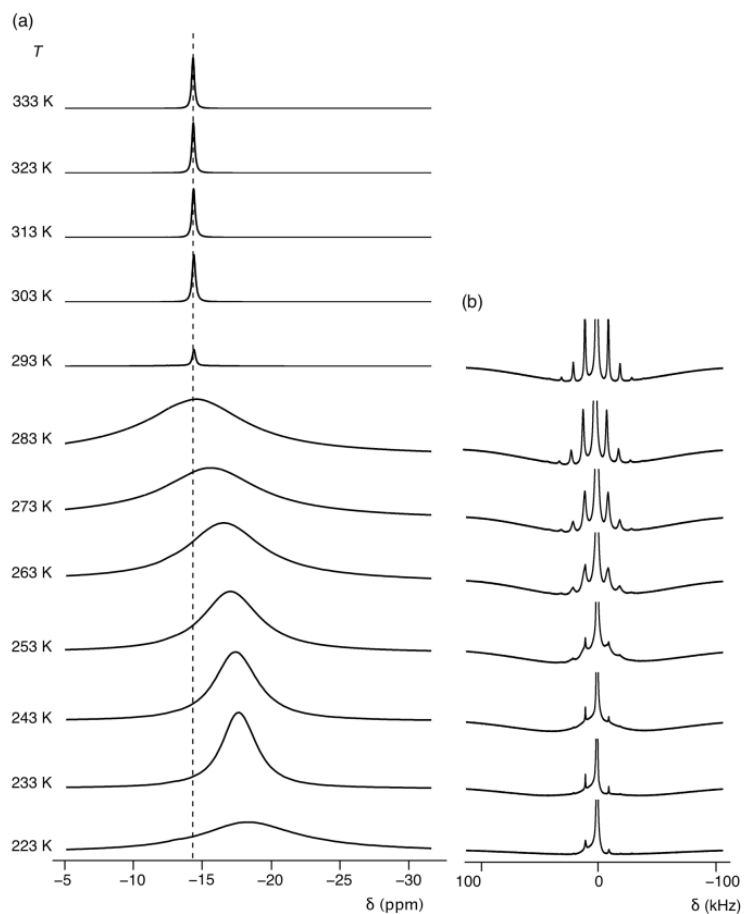


Figure 4.8. (a) Variable-temperature ^1H -decoupled ^{11}B MAS NMR spectra of PCA and (b) ^1H -decoupled ^{11}B MAS NMR spectra of the low temperature phase of PCA recorded using a wide spectral width. The ^{11}B radiofrequency field strength was between 145 and 155 kHz (90° pulse duration of 1.6–1.75 μs), while ^1H decoupling was applied with a field strength of ~ 50 kHz. The recycle interval (in the range 1–3 s) was optimised to ensure that the samples were fully relaxed prior to excitation. Spectra are the result of averaging 8 transients.

coupling interaction. This implies that molecular reorientation remains faster than ~ 1 MHz immediately below the I-II phase transition.

It is not possible to determine from one-dimensional ^{11}B MAS spectra whether the observed shifts include isotropic quadrupolar shifts, or whether

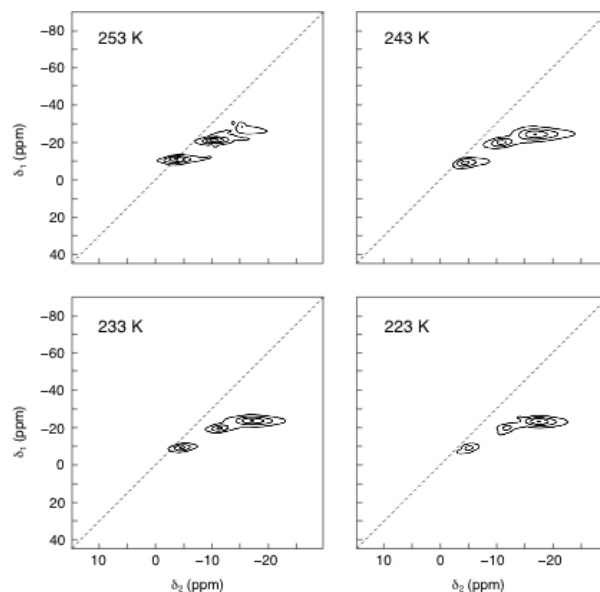


Figure 4.9. Variable-temperature ^1H -decoupled ^{11}B MQMAS NMR spectra of the OCA obtained using the pulse sequence in ref 34. The +3 diagonal is shown as a dotted line in each spectrum. The States-Haberhorn-Ruben method of δ_1 sign discrimination was used and pure-absorption two-dimensional lineshapes by means of a hypercomplex Fourier transform were obtained. The triple-quantum excitation period, τ_{ex} , was optimised at each temperature in the range 10–40 μs . 24 transients were averaged for each t_1 value, with a maximum t_1 of 1.5 ms and z-filter delay of 5 μs . A ^{11}B radiofrequency field strength of 140 kHz and a ^1H decoupling field strength of ~ 50 kHz were used.

they are entirely accounted for by a temperature dependence of the isotropic chemical shifts. This problem may be solved by measuring the frequencies of two different transitions at the *same* magnetic field, as suggested by Eliav *et al.* for measuring dynamic shifts in solution-state NMR [4.45]. Convenient choices for a spin $I = 3/2$ nucleus are the triple-quantum ($m_I = 3/2 \leftrightarrow -3/2$) and single-quantum central ($m_I = 1/2 \leftrightarrow -1/2$) transitions, since they can be measured simultaneously using the well known MQMAS technique in the solid state of Frydman and Harwood [4.46].

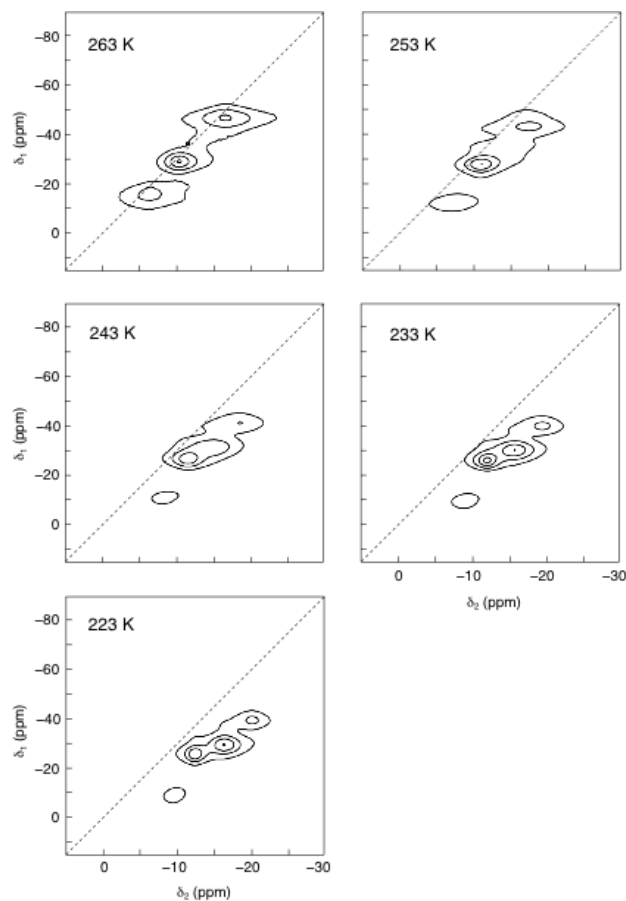


Figure 4.10. Variable-temperature ^1H -decoupled ^{11}B MQMAS NMR spectra of MCA obtained using the pulse sequence in ref 34. The +3 diagonal is shown as a dotted line in each spectrum. The States–Haberkorn–Ruben method of δ_1 sign discrimination was used and pure-absorption two-dimensional lineshapes by means of a hypercomplex Fourier transform were obtained. The triple-quantum excitation period, τ_{ex} , was optimised at each temperature in the range 10–20 μs . 24 transients were averaged for each t_1 value, with a maximum t_1 of 2.5 ms and z-filter delay of 5 μs . A ^{11}B radiofrequency field strength of 140 kHz and a ^1H decoupling field strength of ~ 50 kHz were used.

The total isotropic shift is the sum of the isotropic chemical shift and the isotropic second-order quadrupolar shift. It can be observed from Eqns. (2.38) and (2.39) that the isotropic quadrupolar shift is proportional to

$$A^0(I, m_I) \frac{(\omega_Q^{\text{PAS}})^2}{2\omega_0} \left(1 + \frac{\eta^2}{3}\right) \text{ where } \omega_Q^{\text{PAS}} \text{ is given in Eqn. (2.36). Therefore, in the}$$

absence of motion and for spin $I = 3/2$ nuclei, the isotropic frequencies of the triple-quantum (ν^{TQ}) and single-quantum central transitions (ν^{SQ}), in units of Hz, can be written relative to a reference frequency as a function of the quadrupolar product:

$$\nu^{\text{CT}} = \delta_{\text{CS}} \nu_0 - \frac{1}{40\nu_0} P_Q^2 \quad (4.7)$$

$$\nu^{\text{TQ}} = 3\delta_{\text{CS}} \nu_0 + \frac{3}{40\nu_0} P_Q^2 \quad (4.8)$$

where δ_{CS} is the isotropic chemical shift and P_Q is the quadrupolar product and is equal to:

$$P_Q = C_Q(1 + \eta^2/3)^{1/2} \quad (4.9)$$

In the absence of the quadrupolar shift, the isotropic shifts for the triple-quantum transitions should be exactly three times larger than the isotropic shifts for the single-quantum transitions and the peaks will lie on the line $\delta_1 = 3\delta_2$ in the MQMAS spectrum. Peaks with an isotropic quadrupolar shift are shifted to low frequency in the single-quantum δ_2 dimension and to high frequency in the triple-quantum δ_1 dimension, displacing the peaks "below" the $\delta_1 = 3\delta_2$ line in the conventional representation.

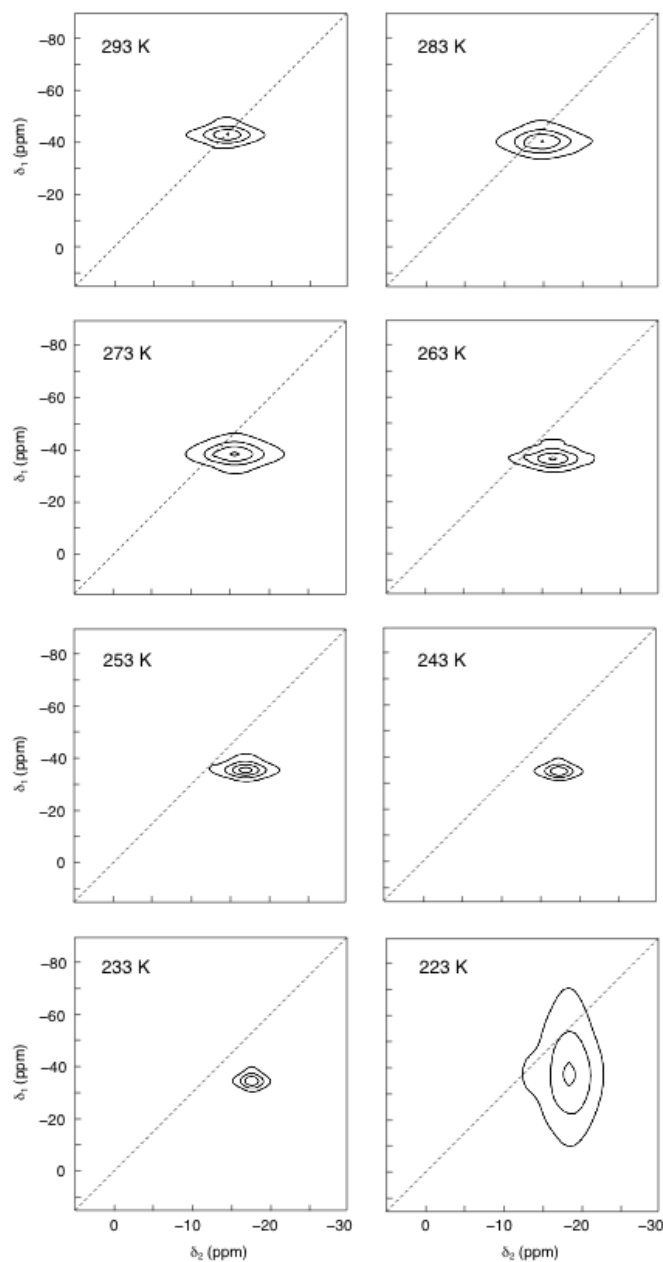


Figure 4.11. Variable-temperature ^1H -decoupled ^{11}B MQMAS NMR spectra of PCA obtained using the pulse sequence in ref 34. The +3 diagonal is shown as a dotted line in each spectrum. The States–Haberkorn–Ruben method of δ_1 sign discrimination was used. The triple-quantum excitation period, τ_{ex} was optimised at each temperature in the range 10–25 μs . 24 transients were averaged for each t_1 value, with a maximum t_1 of 3.8 ms and z-filter delay of 5 μs . A ^{11}B radiofrequency field strength of 160 kHz and a ^1H decoupling field strength of ~ 50 kHz were used. The ^{11}B MQMAS NMR spectrum of PCA recorded at 223 K was obtained using the same pulse sequence but with one pulse instead three pulses to excite triple-quantum coherence. 24 transients were averaged for each of 32 t_1 values, with an increment of 25 μs . All pulses used were non-selective, with the exception of the final 90° pulse, which was selective for the central transition.

MQMAS spectra of OCA, MCA and PCA recorded over the specified temperature range are shown in Figures 4.9, 4.10 and 4.11. Triple-quantum coherences were excited using a three-pulse $90^\circ_\phi - \tau_{\text{ex}} / 2 - 180^\circ_{\phi+90^\circ} - \tau_{\text{ex}} / 2 - 90^\circ_{\phi+90^\circ}$ excitation "sandwich" [4.47] as only small quadrupolar splittings were expected. It can be observed that the peaks do not lie on the line $\delta_1 = 3\delta_2$ and so do exhibit dynamic shifts. These increase as the temperature is reduced, although the magnitude and temperature dependence varies from site to site. The quadrupolar product P_Q can be calculated using Eqs. (4.7) and (4.8) by measuring the δ_1 and δ_2 frequencies of a peak. In the presence of motion, however, the value of P_Q measured by this approach is modified and therefore it is labelled P_Q^{eff} , as described in reference [4.48]. This can range from zero, if the quadrupolar interaction is averaged by rapid isotropic motion, to the intrinsic P_Q observed in the absence of dynamics. Intermediate P_Q^{eff} values should be observed when the motion occurs on a timescale comparable to the Larmor period or when the motion is anisotropic. Figure 4.12 shows the variation of P_Q^{eff} as a function of temperature for each resolved MQMAS peak.

For OCA, intermediate values of P_Q^{eff} , which increase with decreasing temperature, are observed, implying that the rate of motion in phase II is of the

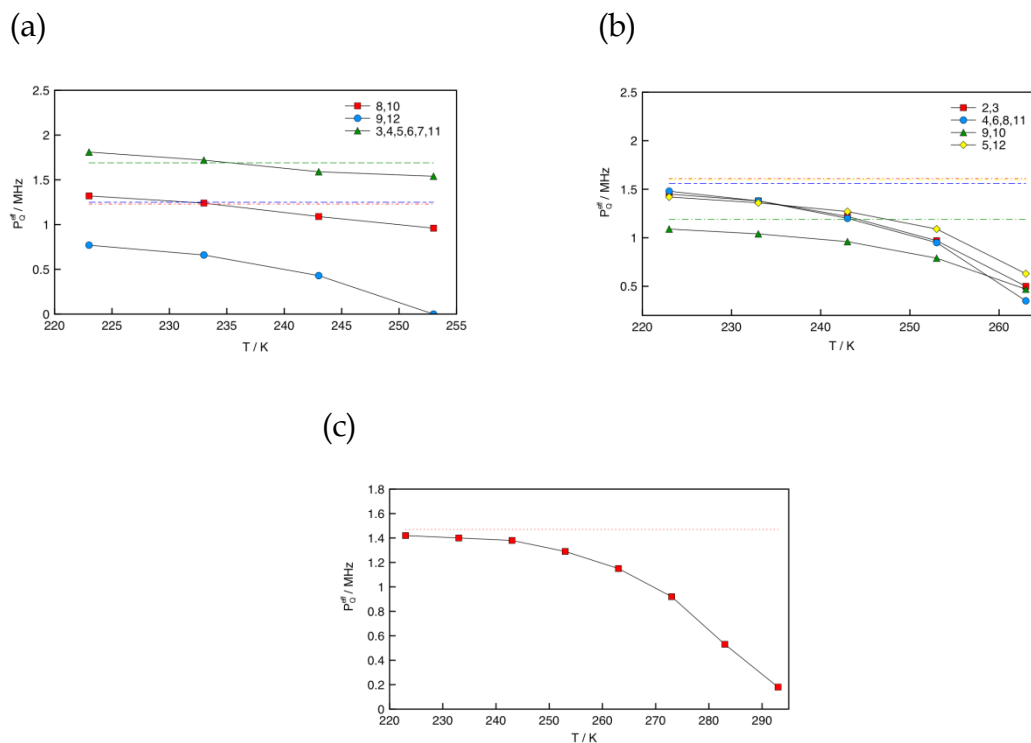


Figure 4.12. Variation of P_Q^{eff} as a function of temperature in the specified range for the chemically-distinct ^{11}B environments of (a) OCA, (b) MCA and (c) PCA. Note that the peaks representing the 3,6 and 4,5,7,11 environments of OCA overlap in the low-temperature phase and are indistinguishable in the MQMAS spectra. Dashed lines are the intrinsic P_Q values predicted by an *ab initio* calculation [4.49].

same order of magnitude as the Larmor frequency. At the lowest used temperature, 223 K, P_Q^{eff} for the 9,12 environment (boron 9 and 12 as shown in Figs. 4.5 and 4.6) remains significantly lower than the calculated intrinsic P_Q , indicating that motion is not fully quenched at the lowest temperature observed.

For MCA, the P_Q^{eff} values remain closer together than for OCA, are near-

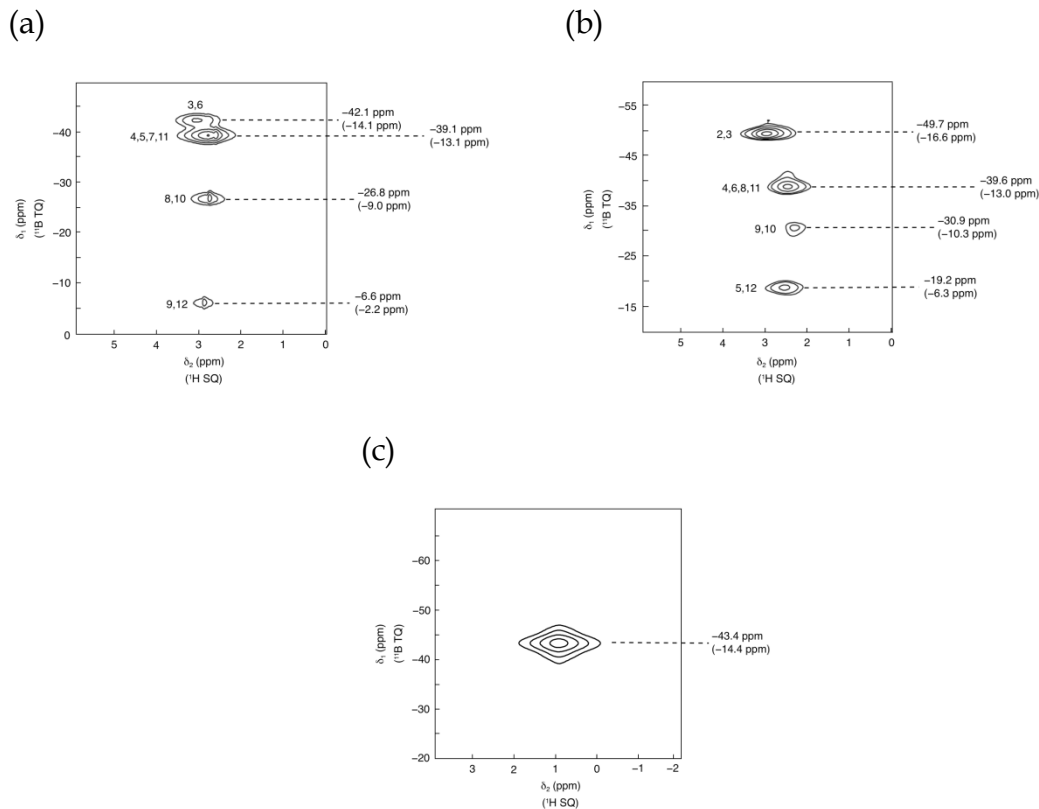


Figure 4.13. Triple-quantum (^{11}B) – single-quantum (^1H) correlation MAS spectrum of (a) OCA (293 K), (b) MCA (293 K) and (c) PCA (303 K). An excitation interval τ of 2 ms and a recycle intervals in the range 1–2 s were used. 48 transients were averaged for each t_1 value with a maximum t_1 of 6.4 ms. The ^{11}B radiofrequency field strength was between 140 and 166 kHz during the RF pulses and 50 kHz during ^{11}B decoupling.

zero at high temperature, and are closer to the calculated intrinsic P_Q values at low temperature. These observations suggest that molecular reorientation is more isotropic than for OCA at high temperatures, and is slower at low temperature.

For PCA, P_Q^{eff} falls steadily almost to zero as the temperature is increased.

This could suggest that reorientation is fast and relatively isotropic just below

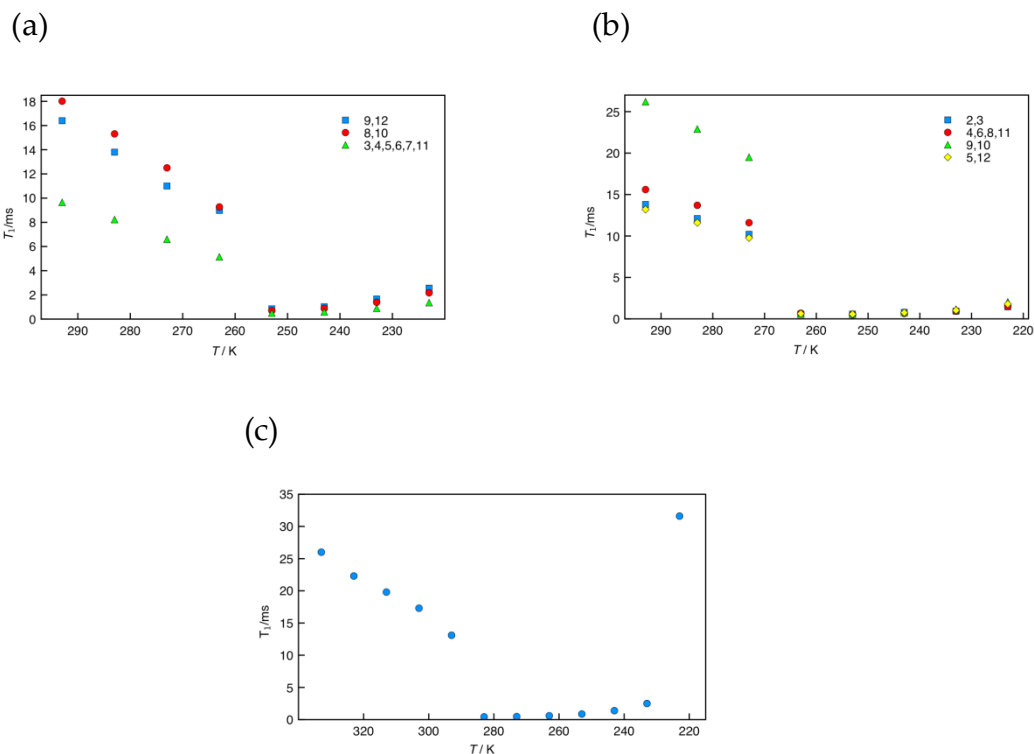


Figure 4.14 ^{11}B spin-lattice relaxation times (T_1) as a function of T for three isomers of carborane, (a) OCA (b) MCA and (c) PCA. The ^{11}B radiofrequency field strength of ~ 150 kHz was used, corresponding to a 90° pulse length of ~ 1.6 μs . The recovery intervals used were optimised for each temperature and isomer, within a range of 3 μs – 5 s.

the I-II phase transition, which is consistent with the suggestion of Beckman and Leffler [4.43] that the absence of an electrostatic dipole moment in PCA leads to reduced intermolecular interactions and less anisotropic reorientation compared with the other isomers.

Because the use of a three-pulse excitation "sandwich" to excite triple-quantum coherence did not yield any signal at high temperature due to averaging of the quadrupolar interactions to nearly zero, therefore an

alternative approach (double-INEPT) can be employed in this regime (the method described in Chapter 3).

Figure 4.13 shows triple-quantum (^{11}B) – single-quantum (^1H) correlation MAS spectra of OCA, MCA and PCA recorded using the double-INEPT pulse sequence shown in Fig. 3.9, together with the ^{11}B triple- and single-quantum frequencies (the latter in parentheses). The single-quantum frequencies were extracted from the one-dimensional spectra in Figs. 4.6, 4.7 and 4.8. For each of the isomers, the triple-quantum frequency was found to be three times the single-quantum frequency, indicating a P_Q^{eff} of zero, and implying isotropic motion at a rate faster than the Larmor frequency.

The spin-lattice relaxation time, T_1 , is sensitive to fast-timescale motion, as mentioned in subsection 4.1.4 of this chapter and, therefore, the temperature dependence of the ^{11}B spin-lattice relaxation time, T_1 , was also investigated in OCA and MCA between 223 and 293 K and in PCA between 223 and 333 K, employing the inversion-recovery technique described in Chapter 3. The temperature dependence of T_1 for the three isomers is shown in Fig. 4.14. The OCA and MCA undergo a single phase transition in the temperature range studied whereas the PCA undergoes two transitions. As the temperature is reduced in phase I, T_1 decreases, suggesting that the reorientation rate exceeds

the ^{11}B Larmor frequency (128.4 MHz) [4.50].

Below the I-II phase transition, longitudinal relaxation is more rapid but T_1 increases as the temperature is reduced, implying molecular reorientation at a rate below the Larmor frequency. Phase III of PCA has a much longer T_1 than the higher temperature phases, consistent with significantly retarded reorientation. The experimental results are in good agreement with the data reported for OCA, MCA and PCA previously [4.43,4.51-4.54].

Since ^{11}B MAS spectra of none of the investigated carboranes exhibit second-order quadrupolar powder patterns, we were interested in comparing these with a carborane where there were no dynamics and a second-order lineshape could be observed. Therefore, the OCA derivative 9,12-diiodo-orthocarborane was synthesized and the two heavy iodine atoms that destroy the near-icosahedral symmetry of the molecule were expected to restrict molecular reorientation.

The one-dimensional ^{11}B MAS spectra of solid 9,12-diiodo-orthocarborane in Figure 4.15 do not exhibit a second-order quadrupolar powder pattern and bear little resemblance to those of the unsubstituted carboranes, with no site-resolution and a much greater linewidth of ~ 3 kHz.

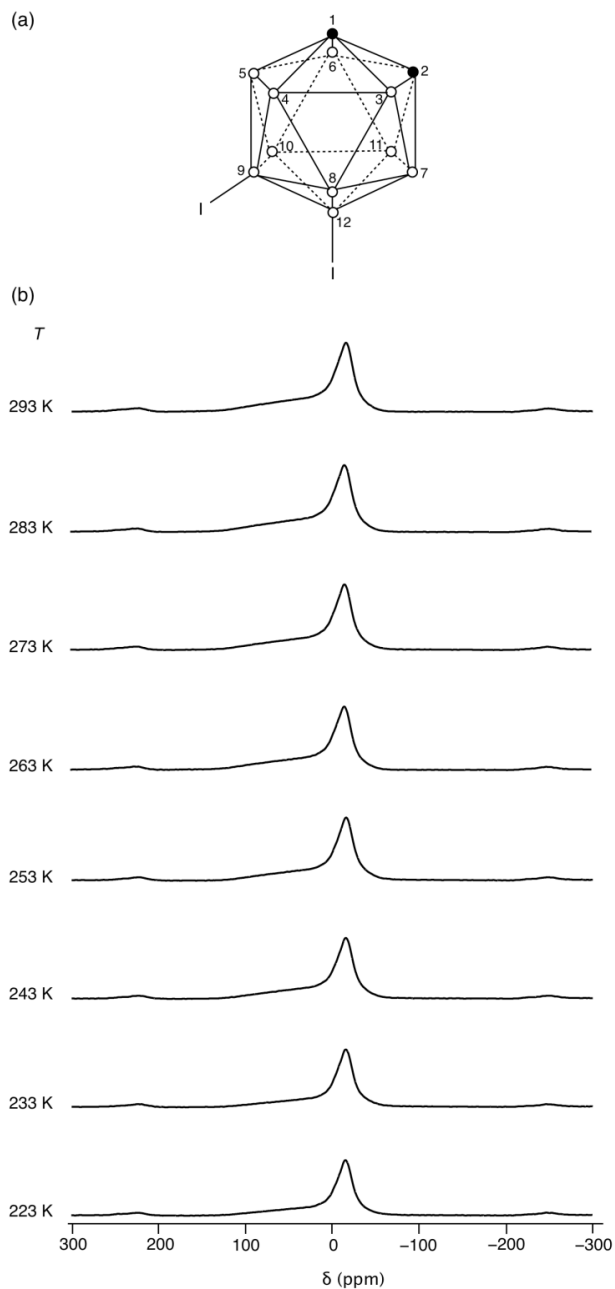


Figure 4.15. (a) Structure and (b) variable-temperature ^1H -decoupled ^{11}B MAS NMR spectra of 9,12-diiodo-*ortho*-carborane. The ^{11}B radiofrequency field strength was 175 kHz (90° pulse duration of 1.0 μs), while ^1H decoupling was applied with a field strength of ~ 50 kHz. The recycle interval of 60 s was used. Spectra are the result of averaging 4 transients.

Furthermore, the spectra show no temperature dependence, suggesting

an absence of motion on the ms - ns timescale.

This two-dimensional ^{11}B MQMAS spectrum was recorded at room temperature using the standard MQMAS pulse sequence. Figure 4.16 presents the two-dimensional MQMAS spectrum of 9,12-diiodo-*ortho*-carborane. The spectrum shows single broad peak and it can be observed that this peak does not lie on the line $\delta_1 = 3\delta_2$ suggesting the possibility of existence of the quadrupolar shift as was found for all three isomers of carborane at low temperatures but further investigations would be necessary to explain it in more detail.

4.2.3. Conclusion

The results presented here show that multiple-quantum NMR measurements of isotropic quadrupolar shifts are a simple way to probe nanosecond timescale motions in plastic solids. The molecular reorientation can be easily and semi-quantitatively probed by using both high-resolution MAS and multiple-quantum MAS NMR spectroscopy.

In this work, the one-dimensional ^{11}B MAS NMR spectra at variety of temperatures were recorded and, even if the second-order quadrupolar powder

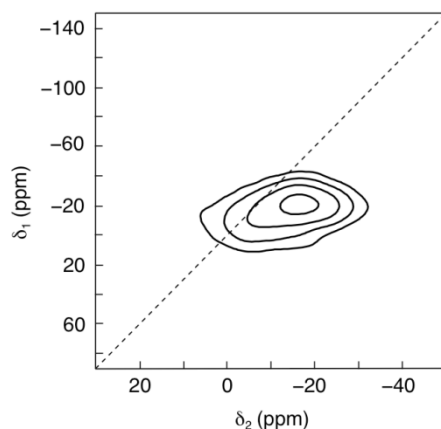


Figure 4.16. ^1H -decoupled ^{11}B MQMAS NMR spectrum of 9,12-diiodo-*ortho*-carborane. 96 transients were averaged for each of 64 t_1 values, with a t_1 increment of 50 μs and with a recycle interval of 60s. A ^{11}B radiofrequency field strength of 150 kHz and a ^1H decoupling field strength of ~ 50 kHz were used.

patterns were observed for none of the investigated carboranes, the lineshapes and the frequencies of the peaks were affected. The ^{11}B linewidth changes within the specified temperature range for each isomer and the spectra have significantly broader lines in the low temperature phase. It means that at high temperatures, molecules undergo rapid isotropic reorientation while, in the low temperature phase, a more solid-like phase, where molecular reorientation is slower and anisotropic, is present.

The effect of the motion on the spinning sidebands intensities was also described and it was shown that, at high temperature, the rapid isotropic motion averages out the quadrupolar interaction and causes the satellite-

transition signal to be concentrated in the centre band. On the other hand, at low temperature, many more spinning sidebands appeared, consistent with more anisotropic motion, resulting in incomplete averaging of the quadrupolar interaction.

In order to confirm a presence of the dynamic shift, the MQMAS spectra of OCA, MCA and PCA were recorded. The peaks in the variable-temperature MQMAS spectra of the three isomers do not lie on the line $\delta_1 = 3\delta_2$ and, hence, do exhibit dynamic shifts. As at high temperature the quadrupolar interactions are averaged to nearly zero and it was not possible to record MQMAS spectra in this regime, using any of the MQMAS pulse sequence described in Chapter 3, therefore a double-INEPT approach was employed. In each double-INEPT spectrum, the triple-quantum frequency was found to be three times the single-quantum frequency, indicating a P_Q^{eff} of zero and showing no dynamic-shift effect.

The temperature dependence of the ^{11}B spin-lattice relaxation time, T_1 , shown in Fig. 4.14, reveals a single phase transition for OCA and MCA and two transitions for PCA in the temperature range studied. Furthermore, the investigations of T_1 show that the reorientation rate exceeds the ^{11}B Larmor frequency in phase I while molecular reorientation at a rate below the Larmor

frequency is suggested below the I-II phase transition.

Additionally, the one-dimensional ^{11}B MAS and two-dimensional ^{11}B MQMAS spectra of solid 9,12-diiodo-orthocarborane were recorded in order to find a sample that shows the effect of dynamic shift and the spectrum with second-order broadened lineshape. It was observed that the one-dimensional spectrum does not exhibit a second-order quadrupolar powder pattern. However, the two-dimensional MQMAS spectrum of 9,12-diiodo-*ortho*-carborane shows a single broad peak which does not lie on the line $\delta_1 = 3\delta_2$ suggesting the existence of the quadrupolar shift.

In summary, the quadrupolar shifts are a good probe of motion even if we are not able to observe a second-order quadrupolar lineshape. In contrast to methods relying on the measurement of T_1 , T_{1r} or T_2 relaxation parameters, the data can be quickly interpreted by visual inspection of two-dimensional NMR spectra.

Chapter 5: Dynamic behaviour of microporous solids

5.1. Introduction

Solids can exhibit porosity and the porous solids are particularly interesting materials when the size of the pores is comparable to the size of molecules. Therefore, the synthesis of such structures with different size and topology of pores gives unlimited possibilities for designing and modifying such materials. Many studies have been undertaken in the area of synthesis and characterization and a variety of applications have been explored including adsorption ability, ion exchange and use as catalysts and molecular sieves.

Porous materials may be classified as microporous, mesoporous or macroporous on account of the size of the pores, with pores with diameter smaller than 2 nm, between 2 and 50 nm and greater than 50 nm, respectively. One well-known class of microporous solids is the zeolites. Zeolites are microporous aluminosilicate minerals known also as "molecular sieves", referring to this particular property. They can be classified according to the

Si/Al ratio, with the ratio between 1 and, in the case of silicates, ∞ , when Si atoms and not Al are present. The fundamental building unit of zeolites is a tetrahedron (SiO_4 or AlO_4) and the SiO_4 units are linked to AlO_4 or one to another by oxygen atoms. The unit cell formula for zeolites, including SiO_4 or AlO_4 tetrahedra, metal cations for electroneutrality (because the zeolites have a charged framework owing to the different oxidation states of Al^{3+} and Si^{4+}) and water molecules is:



where n is the valence of the metal, x is the $\text{SiO}_2/\text{Al}_2\text{O}_3$ ratio ($x \geq 2$) and y is the number of water molecules. The structure of the zeolite framework can be thought to be constructed of a system of cages (with empty spaces) and channels. In terms of the channel system, zeolites can be classified as a one-, two- or three-dimensional network of channels, where molecules can migrate in one direction, in the xy plane, or in any place within a crystal, respectively.

In 1982, Flanigen and co-workers [5.1,5.2] discovered a novel class of crystalline microporous aluminophosphates (AlPOs), with many of them derived from zeolite structures by substitution of Si atoms for P atoms. The difference between zeolites and aluminophosphates is that the former have

charged frameworks while the latter can have neutral or anionic frameworks. In the case of neutral open-framework aluminophosphates, the AlPO_n frameworks, where n is an integer denoting the structure-type, these are composed of alternating AlO₄ and PO₄ tetrahedra with Al/P = 1. Because aluminophosphates are prepared by using a hydrothermal method in the presence of templates or structure-directing agents, which are typically positive charged organic amines, F⁻ (from HF) or OH⁻ (from water) anions are present to balance the positively charged amines. On the other hand, the anionic framework AlPOs (those with Al/P ratio less than unity) are made up of alternate Al-centred polyhedra (AlO₄, AlO₅, AlO₆) and P-centred tetrahedra and they have negatively charged frameworks owing to the terminal P-O bonds. In this case, the negative charge of the framework is neutralised with a positively charged organic template or metal cation. However, as the anionic frameworks of aluminophosphates are unstable upon removal of the occluded protonated template molecules by calcination, they are not discussed here.

Since the discovery of microporous aluminophosphates, they have attracted considerable attention owing to their many applications. More than 200 structure-types of open-framework aluminophosphates have been identified to date. A structure database containing detailed structural information on open-framework AlPOs is reported in the literature [5.3].

One of the more interesting AlPOs, owing to its ability to catalyse highly shape-selective production of light olefins from methanol [5.4-5.6] and the direct oxidation of the terminal carbon of a linear alkane molecule [5.7,5.8], is AlPO-34, which has the topology of chabazite (code: CHA) [5.9]. The CHA-type structure is named after the mineral chabazite, an aluminosilicate that contains a variety of occluded alkali and alkali earth metal cations along with water in its natural form, and for which the thermal behavior above room temperature of a natural specimen has recently been reported [5.10].

It is well known that an aluminophosphate with the triclinic form of the chabazite topology (as-made AlPO-34) can be synthesized from a fluoride medium using morpholine or piperidine as structure-directing agents [5.11-5.15]. In AlPO-34, two fluoride ions bridge between two Al atoms in 4-rings connecting double-6-rings and thus distort the rhombohedral symmetry of chabazite. After thermal treatment the template- and fluoride-free material (calcined-dehydrated AlPO-34) adopts the rhombohedral symmetry of the chabazite topology. Figure 5.1 show the crystal structure of calcined-dehydrated AlPO-34. The framework structure of this phase transforms back to the triclinic symmetry of chabazite in the presence of water (calcined-rehydrated AlPO-34).

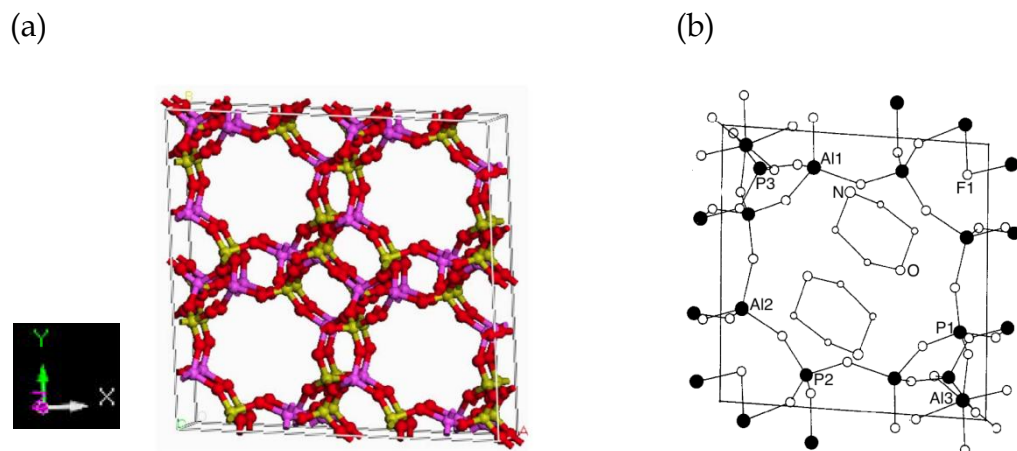


Figure 5.1. (a) Crystal structure of calcined-dehydrated AlPO-34 with aluminium shown in purple, phosphorus in yellow and oxygen in red (b) The unit cell of morph-AlPO-34 showing atom numbering.

Templates that have been identified for the synthesis of heteroatom-substituted AlPO-34 include isopropylamine [5.16,5.17], morpholine [5.18-5.20], piperidine [5.21] and triethylamine [5.22]. Also, the addition of HF in the synthesis gel has been widely reported [5.23-5.25].

As described previously, a large variety of organic templates that occupy the pore and cages play an important role in directing the formation of a specific structure. As a consequence, it is important to understand the templating effect, the nature of the organic template molecule including any dynamic behaviour, and also the structures of the as-made materials and their stability upon removal of the structure-directing organic template. However, it is often difficult to study template or adsorbed guest molecules in porous solids

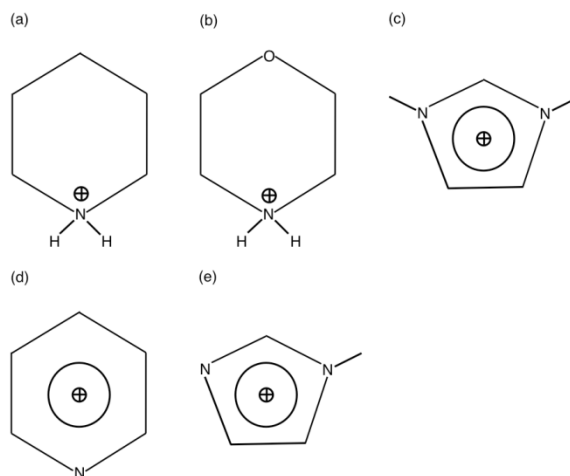


Figure 5.2. Chemical structure of (a) piperidine (b) morpholine (c) 1,3-dimethylimidazolium (d) pyridine and (e) 1-methylimidazolium cations present within the framework of AlPO and GaPO samples.

using standard diffraction techniques, owing to the considerable positional and/or dynamic disorder of the guest species. It is therefore necessary to use methods, such as solid-state MAS NMR spectroscopy, that directly probe the local environments of individual atom types and are sensitive to dynamic behaviour. NMR is a very powerful technique for structural determination, particularly with regards to the coordination states of aluminium, and is a sensitive probe of the dynamics in microporous materials.

The aim of this work is investigating structure, motion and dynamic behaviour in AlPO-34 type materials using the full range of NMR methods, such as MAS, multiple-quantum MAS (MQMAS), satellite-transition MAS

(STMAS) and also first-principles calculations. Furthermore, the first results of NMR experiments of GaPO-34 samples are presented here.

The samples discussed here are:

1. As-made (templated) AlPO-34:
 - a. pip-AlPO-34 - prepared using piperidine ($C_5H_{10}NH$) in the synthesis as the structure-directing agent
 - b. morph-AlPO-34 - prepared using morpholine (C_4H_9NO) in the synthesis as the structure-directing agent
 - c. dmi-AlPO-34 (or SIZ-4) - prepared using the ionic liquid 1-butyl-3-methylimidazolium bromide in the synthesis as the structure-directing agent (1-butyl-3-methylimidazolium bromide was used in the synthesis in order to have only the 1,3-dimethylimidazolium cation within the pores)
2. Calcined AlPO-34:
 - a. dehydrated
 - b. rehydrated
3. Deuterated:
 - a. morph-AlPO-34 - synthesized using deuterated morpholine, water and phosphoric (V) acid

- b. pip-AlPO-34 - synthesized using deuterated piperidine, water and phosphoric (V) acid
- c. Hpip-AlPO-34 - synthesized using protonated piperidine, deuterated water and phosphoric (V) acid

The samples of gallium phosphate materials that have been investigated here are two forms of as-made GaPO-34, one prepared with 1-methylimidazolium salt as the template molecule (mim-GaPO-34) and one with pyridine as the template molecule (py-GaPO-34). Figure 5.2 shows chemical structures of the template molecules (cations) in AlPO-34 and GaPO-34.

5.2. AlPO-34: Results and discussion

5.2.1. As-made AlPO-34

As-made AlPO-34 was prepared using a variety of organic template molecules, employing specific synthesis conditions (preparation of pip- and dmi-AlPO-34 in Appendix A). The first investigated as-made AlPO-34 was pip-AlPO-34. The asymmetric unit of the framework of pip-AlPO-34 is composed of one octahedrally coordinated Al atom coordinated to four O and two F atoms, two tetrahedrally coordinated Al atoms and three tetrahedral P atoms

[5.26] and was expected to be the same as AlPO-34 synthesized with pyridine as a template, as reported previously [5.27]. The X-ray powder diffraction pattern of the as-made triclinic pip-AlPO-34 can be found in the literature [5.28].

^{27}Al and ^{31}P MAS NMR experiments, which have been widely used to study microporous frameworks, were obtained in order to confirm a presence of 4- and 6-coordinated Al atoms and 4-coordinated P atoms. Figure 5.3 shows the one-dimensional ^{27}Al , ^{31}P and ^{13}C MAS NMR spectra of pip-AlPO-34.

Many previous researchers have shown that ^{27}Al NMR chemical shifts can be correlated with the coordination number of aluminum in aluminophosphate compounds [5.29-5.34]. ^{27}Al MAS NMR spectrum of pip-AlPO-34 shows two lines at 40.2 and -6.5 ppm and it can be therefore deduced that they correspond to the 4- and 6-coordinated species, respectively. The first peak is more intense than that of the octahedral species, indicating that this peak probably contains the resonances from the two tetrahedral sites found by the structure analysis. The ^{31}P spectrum consists of three peaks in agreement with the published structure [5.28]. The ^{13}C MAS NMR spectrum was also recorded in order to confirm the presence of the particular template within the structure as chemical shifts in the ^{13}C solid-state NMR spectrum can be

compared with chemical shifts in the ^{13}C liquid-state NMR spectrum found in literature. This spectrum was obtained using the CP method to enhance the magnetization of the low- γ nucleus, ^{13}C , as described in Chapter 3. The ^{13}C spectrum consists of two broad peaks. The peak at 23 ppm is more intense than the one at 47 ppm, suggesting the presence of the two carbons at similar chemical shifts. These results are consistent with the literature [5.35], as the solution ^{13}C NMR spectrum of piperidine shows three peaks at 47.6, 27.3 and 25.3 ppm. It means that the two inequivalent carbon sites at 27.3 and 25.3 ppm are observed as a single broad line in the solid-state NMR spectrum. Therefore, the chemical shifts of two lines at 47.3 and 22.5 ppm in the ^{13}C MAS NMR spectrum correspond to the two carbons bonded to the nitrogen atom and all the other carbons from the ring, respectively.

A high-resolution ^{27}Al MQMAS spectrum of pip-AlPO-34 was recorded, using the pulse sequence in Fig. 3.1b in order to increase significantly the resolution of the spectrum and to separate the contributions of the two Al tetrahedral species. Figure 5.4a shows the two-dimensional ^{27}Al MQMAS (triple-quantum) spectrum of pip-AlPO-34. It can be observed that only two from the three peaks expected from the structure analysis are visible in Fig. 5.4a.

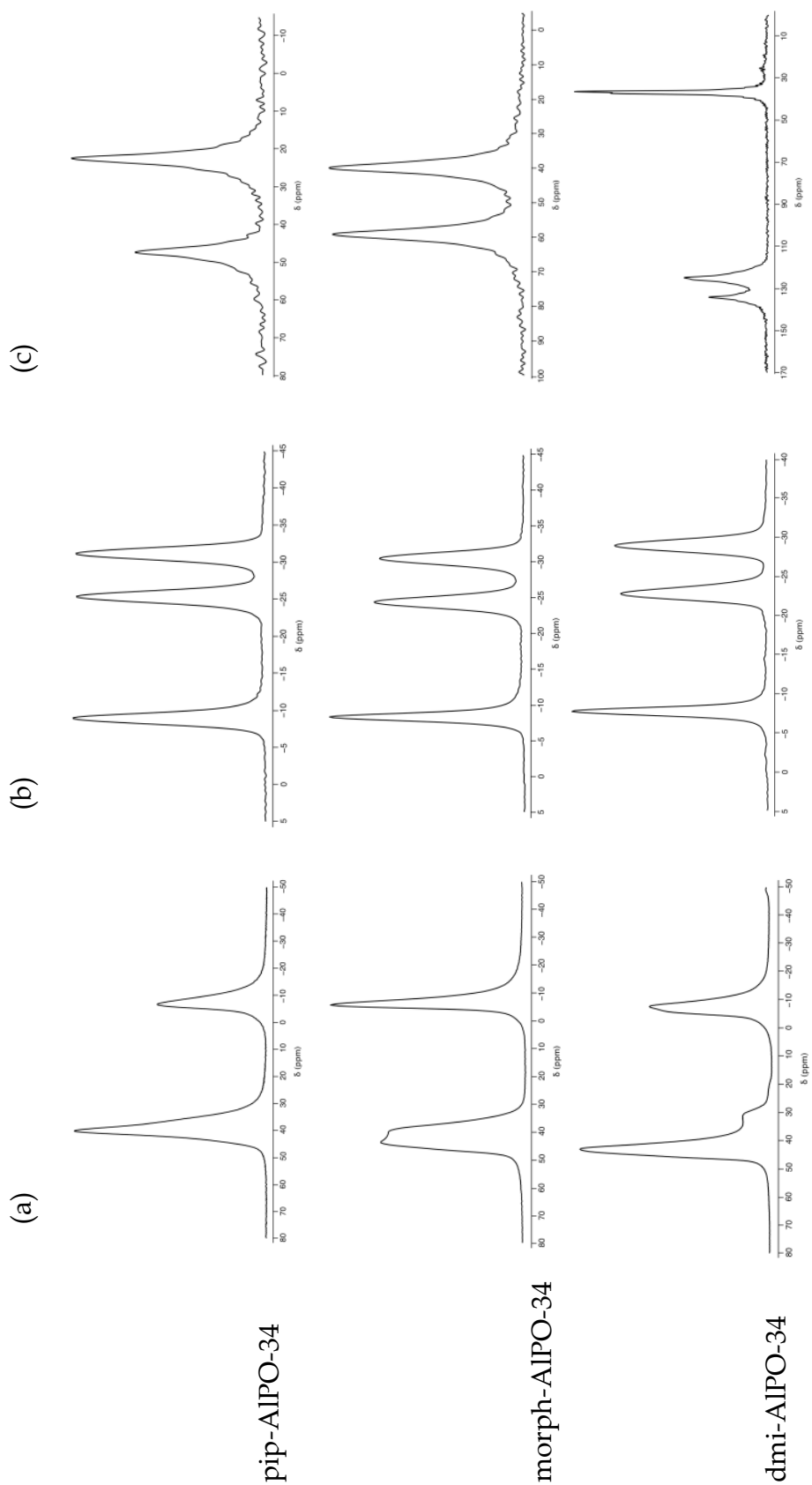


Figure 5.3 (a) ^{27}Al , (b) ^{31}P and (c) ^1H -decoupled single-quantum cross-polarized ^{13}C MAS NMR spectra of as-made pip-, morph- and dmi-AIPO-34. ^{27}Al and ^{31}P spectra are the result of averaging 64 transients with recycle interval of 1 s and 4 transients with recycle interval of 360 s, respectively. The ^{13}C MAS spectra are the result of averaging (pip) 2000 (morph) 28000 and (dmi) 3600 transients with recycle interval in the range of 2-8 s and were recorded with high-power ^1H decoupling. The MAS rate was 10 kHz.

As mentioned in Chapter 4, the evidence for dynamics on the μs timescale is a motional broadening of quadrupolar satellite-transition spinning sidebands because the intensities of spinning sidebands are dependent on the motional process in the sample and thus on the temperature. Therefore, a further investigation of as-made pip-AlPO-34 was to record one-dimensional ^{27}Al MAS NMR spectra with a wide spectral width at two different temperatures. Figure 5.5a shows ^{27}Al MAS NMR spectra recorded at 293 and 333 K. A wide spectral width has been used and the spinning angle accurately set to the magic angle, so that the spinning sidebands of the satellite transitions can be observed. Reduced spinning sideband intensity is observed at 293 K. Therefore, it can be assumed that the motional frequency within pip-AlPO-34 is high compared with the size of the quadrupolar coupling. However, even at 333 K, each satellite sideband is still broad overall, suggesting that the sidebands are probably strongly motionally broadened at both temperatures.

Since motional broadening was observed in variable-temperature NMR spectra, a STMAS experiment was performed in order to investigate this dynamic behaviour in detail. A correlation of the two transitions in a two-dimensional STMAS experiment allows the removal of the second-order broadening, as discussed in Chapters 3 and 4, therefore the STMAS spectrum of pip-AlPO-34 was recorded. The STMAS NMR experiment was performed using

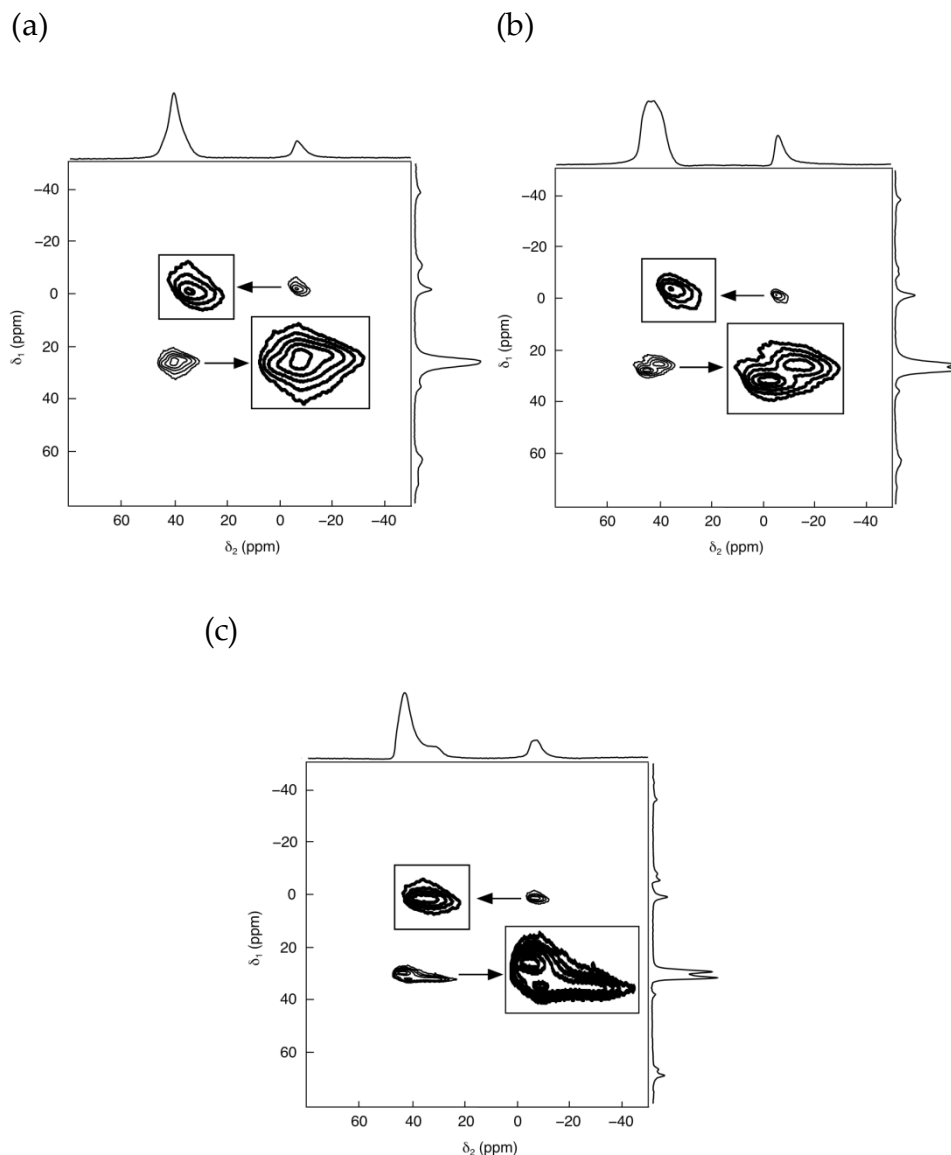


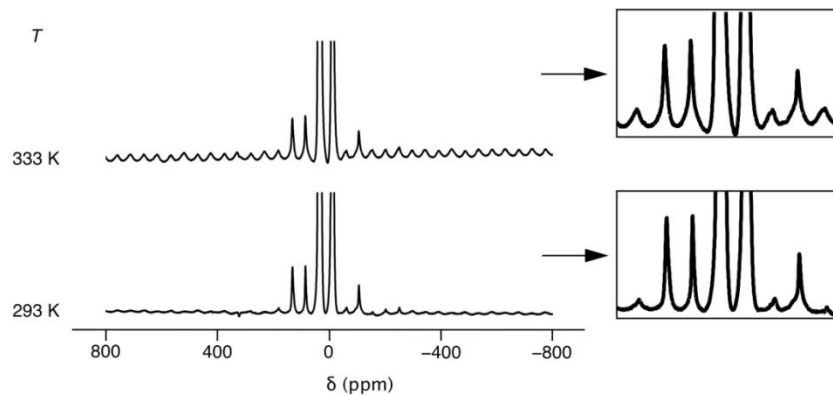
Figure 5.4 Two-dimensional ^{27}Al MQMAS (triple-quantum) spectrum of (a) pip-AIPO-34, (b) morph-AIPO-34 and (c) dmi-ALPO-34. 96 transients were averaged for each 256 t_1 values, with a t_1 increment of 12.5 μs with a recycle interval of 1s; z-filter intervals τ of (a) 95.25 μs , (b) 98.50 μs and (c) 98.45 μs were used. The time-proportional phase incrementation (TPPI) method of δ_1 sign discrimination was used and pure-absorption two-dimensional lineshapes were obtained by means of a hypercomplex Fourier transform. The concept is of acquisition of an echo or shifted echo FID in t_2 and the use of a z-filter when acquiring data in the hypercomplex manner, both of which require straightforward additions to the simple pulse sequence in Fig. 3.1b and have been reviewed in much more detail. [5.36-5.38]

the pulse sequence shown in Fig. 3.3b and the spinning angle was accurately

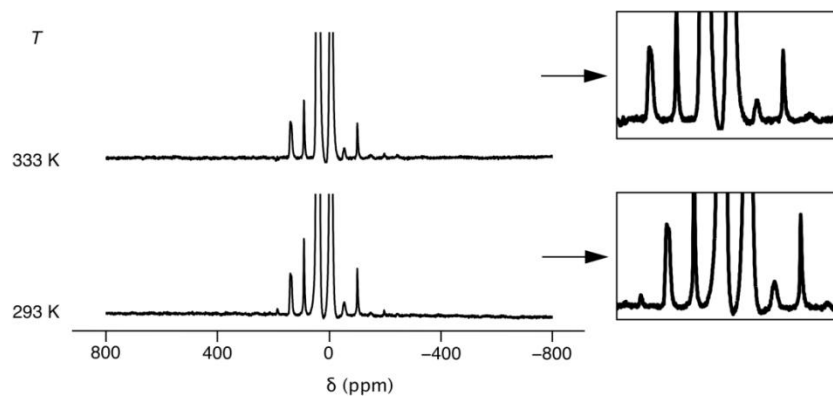
adjusted to the magic angle (54.736°) using the ^{87}Rb ($I = 3/2$) STMAS signal from RbNO_3 . Figure 5.6 presents the STMAS spectrum of pip-AlPO-34. As pip-AlPO-34 possesses three distinguishable Al sites, three ridge lineshapes are expected to be observed. However, only the two ^{27}Al peaks lie on the CT \rightarrow CT diagonal (+1) and none of the ST \rightarrow CT ridges are observed. This observation may be explained by very strong dynamic broadening, as was observed in ^{27}Al MAS NMR spectra with a wide spectral width.

A second as-made material, morph-AlPO-34, prepared in the same way as pip-AlPO-34 but using morpholine as the organic template molecule seems to be an interesting material for the comparison of the motions in those two samples. The structure was determined using synchrotron radiation [5.24]. Two fluorine atoms were found to bridge two aluminium atoms of a 4-membered ring, which connects two double-6-rings of the chabazite type structure as in the case of pip-AlPO-34. The additional F atoms are compensated by two morpholinium cations located in each chabazite cage. The unit cell formula is $(\text{AlPO}_4)_6(\text{C}_4\text{H}_{10}\text{NO})_2\text{F}_2$ and the unit cell of morph-AlPO-34 is presented in Fig. 5.1b. There are three crystallographic sites for Al: one Al is 6-coordinated to 4 oxygens and 2 fluorine atoms, and two Al atoms are 4-coordinated.

(a)



(b)



(c)

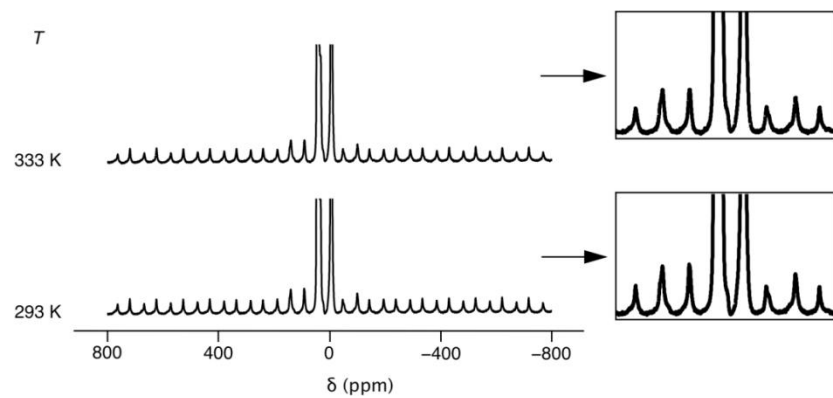


Figure 5.5 ^{27}Al MAS NMR spectra of (a) pip-AIPO-34, (b) morph-AIPO-34 and (c) dmi-AIPO-34 with a wide spectral width recorded at 293 and 333 K. ^{27}Al and ^{31}P spectra are the result of averaging 64 transients with recycle interval of 1 s and 4 transients with recycle interval of 360 s, respectively. The MAS rate was 10 kHz.

The ^{27}Al , ^{31}P and ^{13}C MAS NMR spectra of morph-AlPO-34 look very similar to those of the piperidine templated AlPO-34 and are displayed in Fig. 5.3. The ^{13}C spectrum of morph-AlPO-34 consists of two broad peaks the same as in the spectrum of pip-AlPO-34. The chemical shifts of these two lines are 46.1 and 65.4 ppm corresponding to carbons bonded to the nitrogen atom and those bonded to the oxygen atom, respectively. These values are in good agreement with previous liquid-state NMR studies that showed signals at 46.6 and 68.2 ppm [5.39]. The ^{31}P NMR MAS spectra show lines in the chemical shift range -35 to -5 ppm consistent with tetrahedrally coordinated phosphorus (as PO_4) in the framework of the materials. The ^{27}Al spectrum of morph-AlPO-34 resembles pip-AlPO-34. This spectrum shows two lines at 40.2 and -6.3 ppm with the first two peaks overlapping. This result shows that the structure of both as-made samples is the same. The ^{27}Al MQMAS spectrum was also recorded in order to observe all crystallographically distinct Al sites and it is presented in Fig. 5.4b. It can be immediately observed that the three expected lines are clearly visible in that spectrum. It means that the 4-coordinated Al sites have been fully resolved by the MQMAS experiment and it can be deduced that the ^{27}Al MAS NMR spectrum contains two tetrahedral sites and one octahedral site.

Once again, as in the case of pip-AlPO-34, ^{27}Al MAS NMR spectra with a

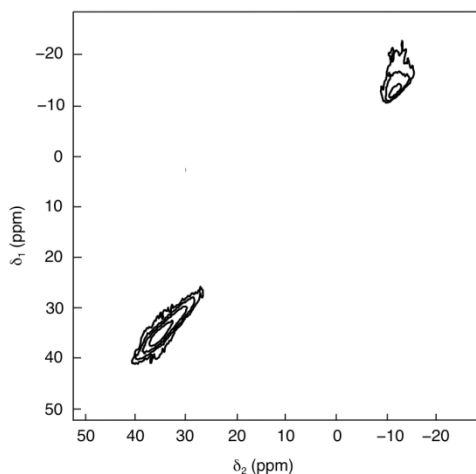


Figure 5.6 Two-dimensional ^{27}Al STMAS spectrum of pip-AlPO-34 recorded using the amplitude-modulated z-filtered pulse sequence. The spectrum is the result of averaging 64 transients for each 138 t_1 values, with a t_1 increment of 50 μs . A recycle interval of 1 s and the a z-filter interval of 2 ms were used. The States-Haberhorn-Ruben (States) method of δ_1 sign discrimination was used.

wide spectral width shown in Fig. 5.5b were recorded at 293 and 333 K to compare motions in those two samples. They did not show any spinning sidebands of the satellite transitions, even upon raising the temperature. This suggests that the spinning sidebands in this AlPO are so strongly motionally broadened that it is not possible to observe them. This suggests that motion is slower than in pip-AlPO-34. For comparison, in the piperidine they have been observed in the conventional MAS NMR spectrum recorded at 333 K (very broad) but not in the STMAS spectrum.

Morris and co-workers [5.40,5.41] have also used ionic liquids as both the solvent and template for the preparation of SIZ-n type AlPO materials. This

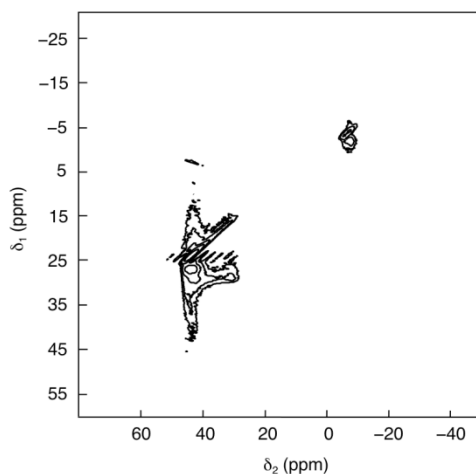


Figure 5.7 Two-dimensional ^{27}Al STMAS spectrum of dmi-AIPO-34 recorded using the phase-modulated split- t_1 shifted-echo pulse sequence. The spectrum is the result of averaging 128 transients for each 256 t_1 values, with a t_1 increment of 100 μs . A recycle interval of 1 s was used.

"ionothermal" method is unique in that the solvent also acts as the structure-directing agent (Appendix A). Furthermore, the unique properties of imidazolium ionic liquids were exploited to synthesize several new AIPO materials, SIZ-1 to SIZ-11 [5.42]. While the frameworks and structures of pip-AIPO-34 and morph-AIPO-34 are well known, information about a third as-made material, dmi-AIPO-34 (SIZ-4) with 1,3-dimethylimidazolium cation as the organic template molecule, is not widely available. No published data of NMR experiments of that sample have appeared although active research is expected in this area. Therefore, dmi-AIPO-34 seems to be a very interesting sample to investigate in order to describe its structure and motional behaviour and to compare the results with those obtained for other as-made AIPO-34s.

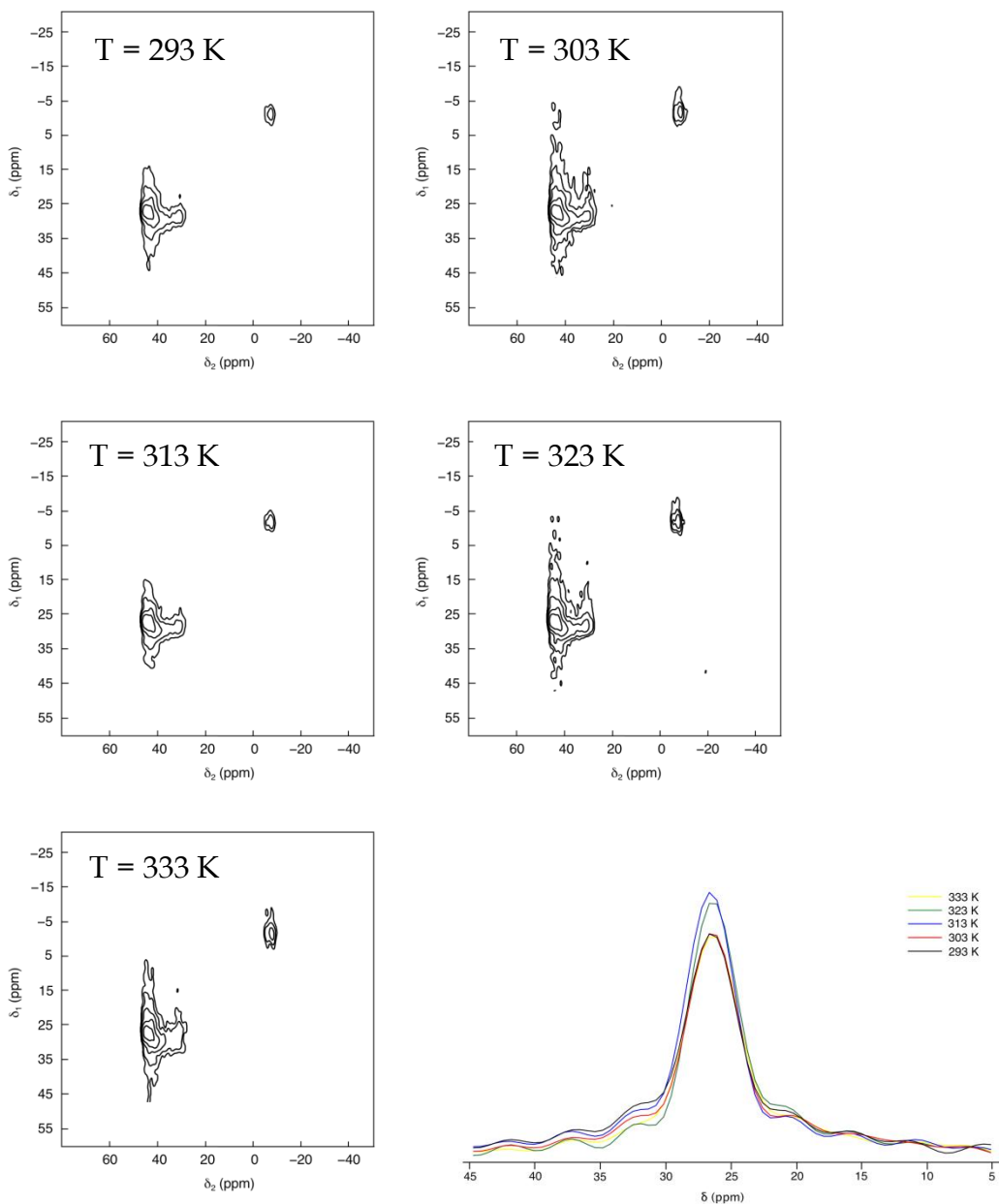


Figure 5.8 Two-dimensional ^{27}Al DQF-STMAS spectra of dmi-AIPO-34 recorded at 293, 303, 313, 323 and 333 K using pulse sequence shown in Fig. 3.5 and cross-sections parallel to the δ_1 dimensions that correspond to peak at 40 ppm extracted from ^{27}Al DQF-STMAS spectra. Spectra are the result of averaging 1024 transients for each of 16 t_1 values, with a t_1 increment of 100 μs and with a recycle interval of 1 s. The τ intervals, τ_1 and τ_2 , were 3 μs and 5 ms, respectively.

Yu and co-workers [5.43] described the synthesis of anionic SIZ-4 and its crystal structure analysis using single-crystal X-ray diffraction. Their structural

analysis indicates that SIZ-4 has the unit cell formula of $[\text{Al}_3\text{P}_4\text{O}_{16}][\text{C}_5\text{N}_2\text{H}_9]_2[\text{NH}_4]$. They have proposed the two-dimensional network that is constructed from some one-dimensional chains composed of alternating AlO_4 and PO_4 units. The asymmetric unit contains three distinct tetrahedral AlO_4 units and four distinct tetrahedral P atoms.

As in the case of the two other as-made AlPO-34 one-dimensional spectra were first recorded in order to confirm the presence of the triclinic form of the chabazite topology and compare results with those found for AlPO samples prepared with piperidine and morpholine. The ^{27}Al , ^{31}P and ^{13}C MAS NMR spectra of dmi-AlPO-34 are displayed in Fig. 5.3. The ^{31}P MAS NMR spectrum of dmi-AlPO-34 looks identical to the morpholine templated AlPO-34 and is composed of three resonances between -35 and -5 ppm. The ^{13}C spectrum of dmi-AlPO-34 in Fig. 5.3c shows three peaks. The chemical shifts of these three lines are at 134.0, 125.4 and 37.2 ppm and correspond to the carbons bonded to both nitrogen atoms, the other carbons from the ring linked to each other through the double bond, and carbons from the methyl groups, respectively, consistent with the literature in reference to liquid-state NMR of the template [5.39]. The ^{13}C NMR spectrum of SIZ-4 shows narrower peaks compared to the ^{13}C NMR spectra of pip- and morph-AlPO-34. However, the ^{27}Al MAS NMR spectrum of dmi-AlPO-34 looks very similar to the morpholine and piperidine

templated AlPO-34 but with different relative intensities. It shows signals at 40.1 ppm (4-coordinate) and -12.2 ppm (6-coordinate). As the 40 ppm peak is more intense than the other peak, indicating that this peak probably contains the resonances from the two or more 4-coordinated Al sites, the MQMAS spectrum was recorded and is presented in Fig. 5.4c. Compared with the MAS spectrum, peaks in two-dimensional MQMAS spectrum are better resolved and two 4-coordinated and one 6-coordinated Al sites are visible.

The ^{27}Al MAS NMR spectrum with a wide spectral width at 333 K was also recorded and compared with the same spectrum recorded at 293 K to investigate whether there is a motional broadening effect of the spinning sidebands. This spectrum did not show any difference in the linewidth of the spinning sidebands of the satellite transitions compared to the spectrum recorded at 293 K. Therefore, it can be deduced that this sample presents no motion on μs timescale. However, because of the high intensity of the spinning sidebands observed in Fig. 5.5c, the STMAS spectrum of dmi-AlPO-34 presented in Figure 5.7 has been recorded using the pulse sequence shown in Fig. 3.4b. This is the first as-made sample of AlPO-34 investigated here for which it was possible to obtain an STMAS spectrum with observable satellite transitions. In other samples, the satellite transitions appeared to be too broad for this to be possible, probably as a result of strong dynamic broadening.

Because of the overlapping different types of transitions such as the CT and ST₁ in the ²⁷Al STMAS NMR spectrum, a double-quantum filtered method, with the pulse sequence shown in Fig. 3.5, has been employed in the rotor-synchronized t₁ dimension of the STMAS experiment to simplify the spectrum as described in Ref. 3.25. The ²⁷Al DQF-STMAS spectra recorded as a function of temperature in the range 293 – 333 K and also cross-sections parallel to the δ₁ dimension that correspond to the peak at 40.1 ppm extracted from each DQF-STMAS spectrum of dmi-AlPO-34 are displayed in Fig. 5.8. It can be observed that the linewidth does not change in the isotropic dimension. However, small changes in peaks intensities are observed but they are difficult to rationalise. Therefore, further studies have still to be performed in order to give a definitive explanation for this observation.

5.2.2. Deuterated AlPO-34

One interesting avenue for investigation of aluminophosphates is to show if the deuteration of the sample affects the motional behaviour. It can be investigated by checking if the ²⁷Al and ³¹P spectra differ from those recorded for the ¹H form of the samples and by using ²H NMR spectroscopy, since molecular motion can influence the ²H NMR lineshape. The samples of aluminophosphate materials synthesized using deuterated organic templates

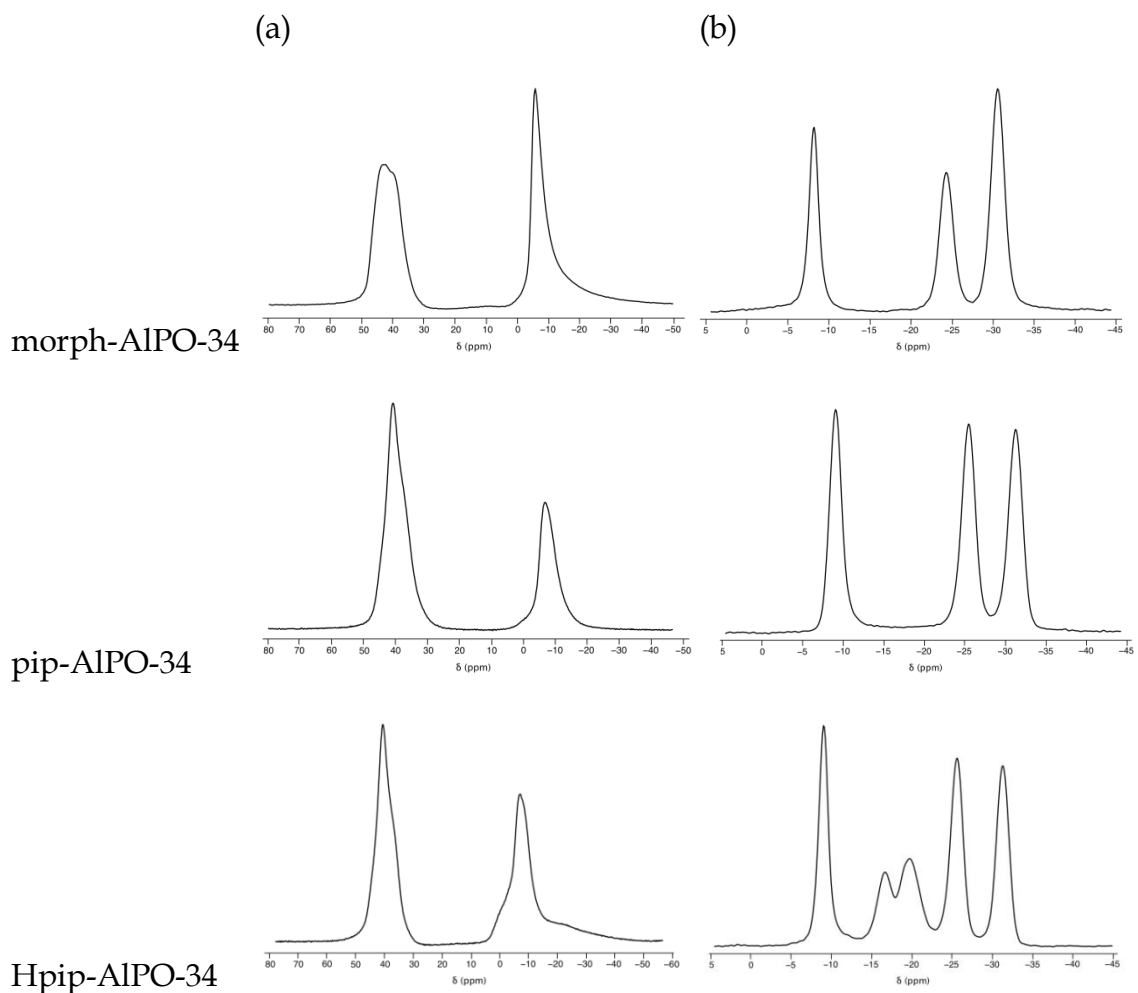


Figure 5.9 (a) ^{27}Al and (b) ^{31}P MAS NMR spectra of deuterated morph-AlPO-34, pip-AlPO-34 and Hpip-AlPO-34.

were deuterated morph-AlPO-34 and pip-AlPO-34. Additionally, results for pip-AlPO-34 deuterated using D_2O , D_3PO_4 and protonated instead of deuterated piperidine (Hpip-AlPO-34) are discussed here. Therefore, in the case of Hpip-AlPO-34 only the presence of the deuterons arising from D_2O and/or OD, not from deuterated organic template as for the two other materials, is expected.

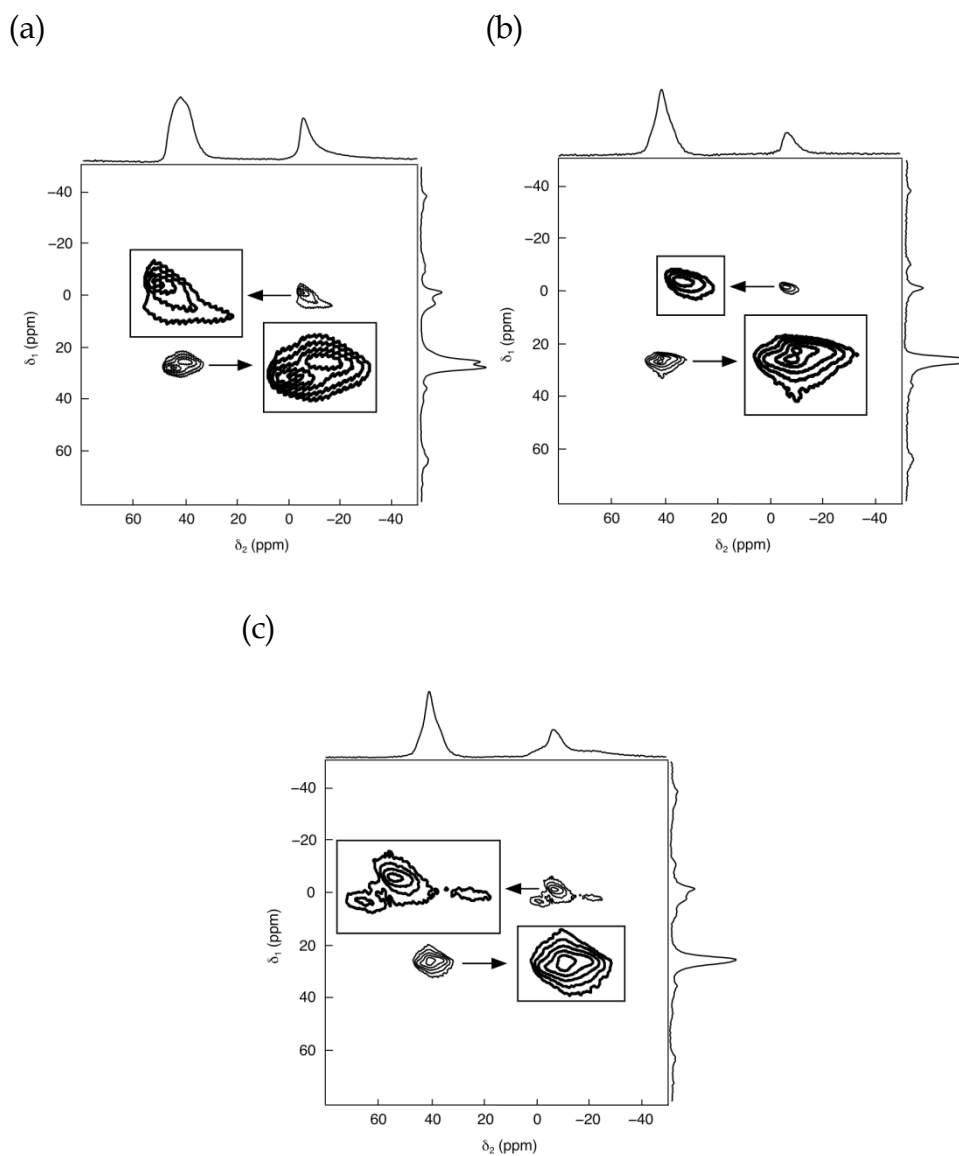


Figure 5.10 Two-dimensional ^{27}Al triple-quantum MAS NMR spectrum of deuterated (a) morph-AlPO-34, (b) pip-AlPO-34 and (c) Hpip-AlPO-34.

The first step of this investigation was to record ^{27}Al and ^{31}P one-dimensional spectra. Figure 5.9 shows the ^{27}Al and ^{31}P MAS spectra of deuterated samples. The parameters used to record all ^{27}Al and ^{31}P MAS spectra of deuterated samples are the same as for the ^1H forms.

The ^{27}Al MAS spectra are essentially identical to the ^1H form of all three samples while the ^{31}P MAS spectrum had the same shifts but the intensities are rather different in the case of deuterated morph- and pip-AlPO-34. It could be due to changes in relaxation or dipolar coupling behaviour following deuteration. However, the ^{31}P MAS spectrum of Hpip-AlPO34 shows two additional peaks between -15 and -25 ppm probably arising from an impurity. High-resolution ^{27}Al MQMAS spectra of the deuterated samples were recorded for the purpose of averaging out the second-order quadrupolar interaction and to separate the contributions of the two tetrahedral species observed unresolved in the one-dimensional ^{27}Al MAS spectra, as in the case of as-made AlPO-34 materials. Figure 5.10 displays the two-dimensional ^{27}Al MQMAS (triple-quantum) spectra. It can be observed that the two tetrahedral Al peaks are resolved in Fig. 5.10a and 5.10b but only two of the three expected peaks are visible in Fig. 5.10c. Furthermore, in the case of deuterated morph-AlPO-34 and Hpip-AlPO-34, in the δ_2 dimension broad peaks from an impurity are also observed between 5 and -22 ppm. It will be shown in the following subsection that the starting material (Al_2O_3) used to synthesize the AlPO-34 samples contains an impurity and some of the spectra show additional peaks origin probably from this impurity. Furthermore, this explanation of the presence of the additional peaks in NMR spectra was confirmed by X-ray diffraction pattern of AlPO-34 samples recorded by Dr R. I. Walton's group.

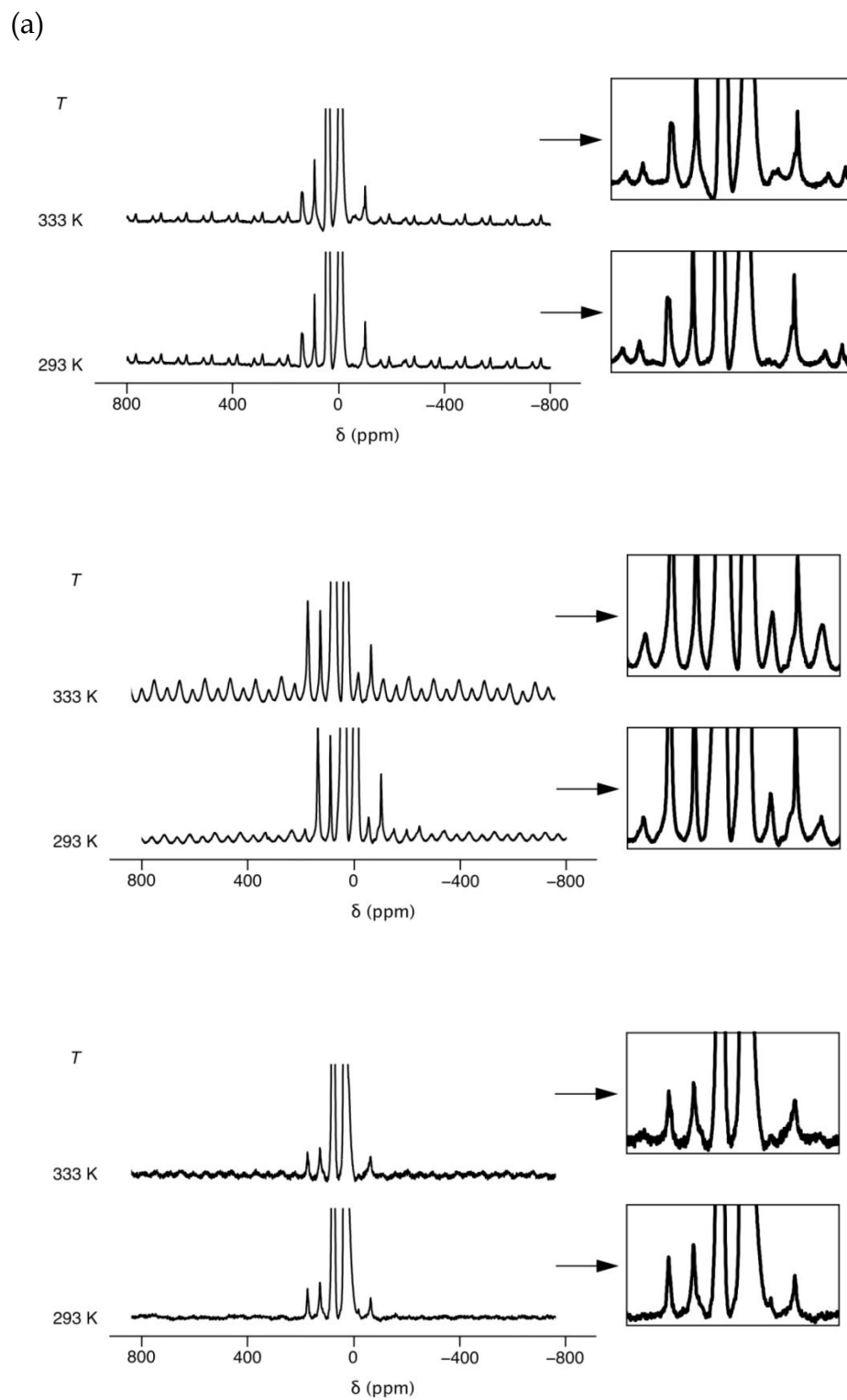


Figure 5.11 ^{27}Al MAS NMR spectra with a wide spectral width recorded at room temperature and at 333 K of deuterated (a) morph-AlPO-34, (b) pip-AlPO-34 and (c) Hpip-AlPO-34.

In addition, one-dimensional ^{27}Al MAS NMR spectra with a wide spectral width were recorded at variable temperature to check if the spinning sidebands of the satellite transitions are observed and depend on the temperature. Figure 5.11 shows ^{27}Al MAS NMR spectra of the deuterated samples recorded at room temperature and at 333 K both recorded with a wide spectral width.

The spectra of deuterated morph-AlPO-34 show spinning sidebands of the satellite transitions with very low intensities. These spectra were analysed in more detail, with the frequency difference between the central transition and the spinning sidebands being measured. This indicated that the spinning sidebands probably originate from the impurity; this was confirmed by the results of the MQMAS experiment. However, the two-dimensional STMAS spectrum of deuterated morph-AlPO-34 was also recorded. The two-dimensional ^{27}Al STMAS split- t_1 spectrum is displayed in Fig. 5.12. The ^{27}Al STMAS spectrum consists of central transition (CT) peaks. Peaks at $\delta_2 = -10$ ppm and $\delta_2 = 10$ ppm are also observed, which confirms the observation made with respect to the one-dimensional ^{27}Al MAS spectrum with the wide spectral width and the MQMAS spectrum that there is an impurity present in the deuterated morph-AlPO-34.

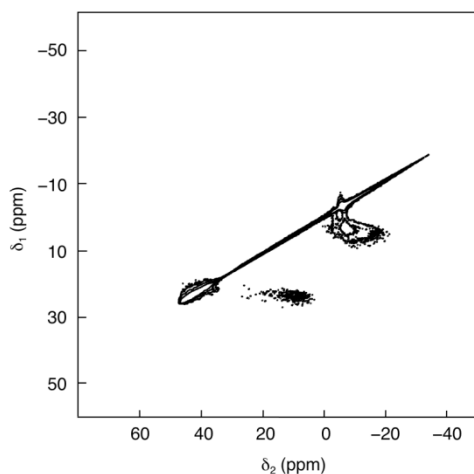


Figure 5.12 Two-dimensional ^{27}Al STMAS spectrum of deuterated morph-AlPO-34 recorded using the split- t_1 pulse sequence.

The variable-temperature ^{27}Al MAS NMR spectra of deuterated pip- and Hpip-AlPO-34 show a slight narrowing of the spinning sidebands as the temperature increases. It can be assumed that in deuterated pip- and H-pip-AlPO-34 some motions are present but it was not possible to record the STMAS spectrum of either sample to investigate this problem in more detail, probably due to strong dynamic broadening.

As ^2H spectroscopy is widely used in motional studies (on the μs timescale), primarily via lineshape analysis, ^2H MAS NMR experiments were performed in order to give an explanation of the effect of narrowing spinning sidebands with increasing temperature in the case of pip- and Hpip-AlPO-34. The purpose of the ^2H MAS NMR experiments was also to study dynamics

concentrating on the intensities or linewidths of the spinning sidebands that exhibit a strong motional broadening if a dynamic reorientation of the ^2H quadrupole tensor is occurring on the μs timescale.

^2H MAS NMR spectra with and without rotor-synchronization and with a wide spectral width were recorded to observe the intensities of the spinning sidebands. The ^2H MAS spectra of deuterated morph-, pip- and Hpip-AlPO-34 are displayed in Figure 5.13. In the case of deuterated morph-AlPO-34, the ^2H MAS spectrum shows a single narrow peak at ~ 7 ppm, probably corresponding to deuterons from deuterated morpholine molecules, and rotor-synchronization does not change the spectrum. However, the ^2H MAS spectrum of deuterated pip-AlPO-34 shows a single peak at 5.5 ppm which is narrow probably due to rapid tumbling of deuterated piperidine, while a broad component at 3.6 ppm appears during rotor-synchronization. This peak originates probably from deuterated water. The ^2H MAS spectrum of the third deuterated sample shows one narrow peak at 6.8 ppm with high intensity and three additional peaks at 8.2, 7.5 and 5.40 ppm. Peaks at 6.8, 7.5 and 8.2 ppm can originate from piperidine (6H arising from CH_2 groups, 1H from the NH group and 4H from $\text{N}(\text{CH}_2)_2$ groups, respectively) while the peak at 5.4 ppm can originate from deuterated water. However, as protonated instead of deuterated piperidine was used to synthesis piperidine within the sample. The ^2H MAS spectrum

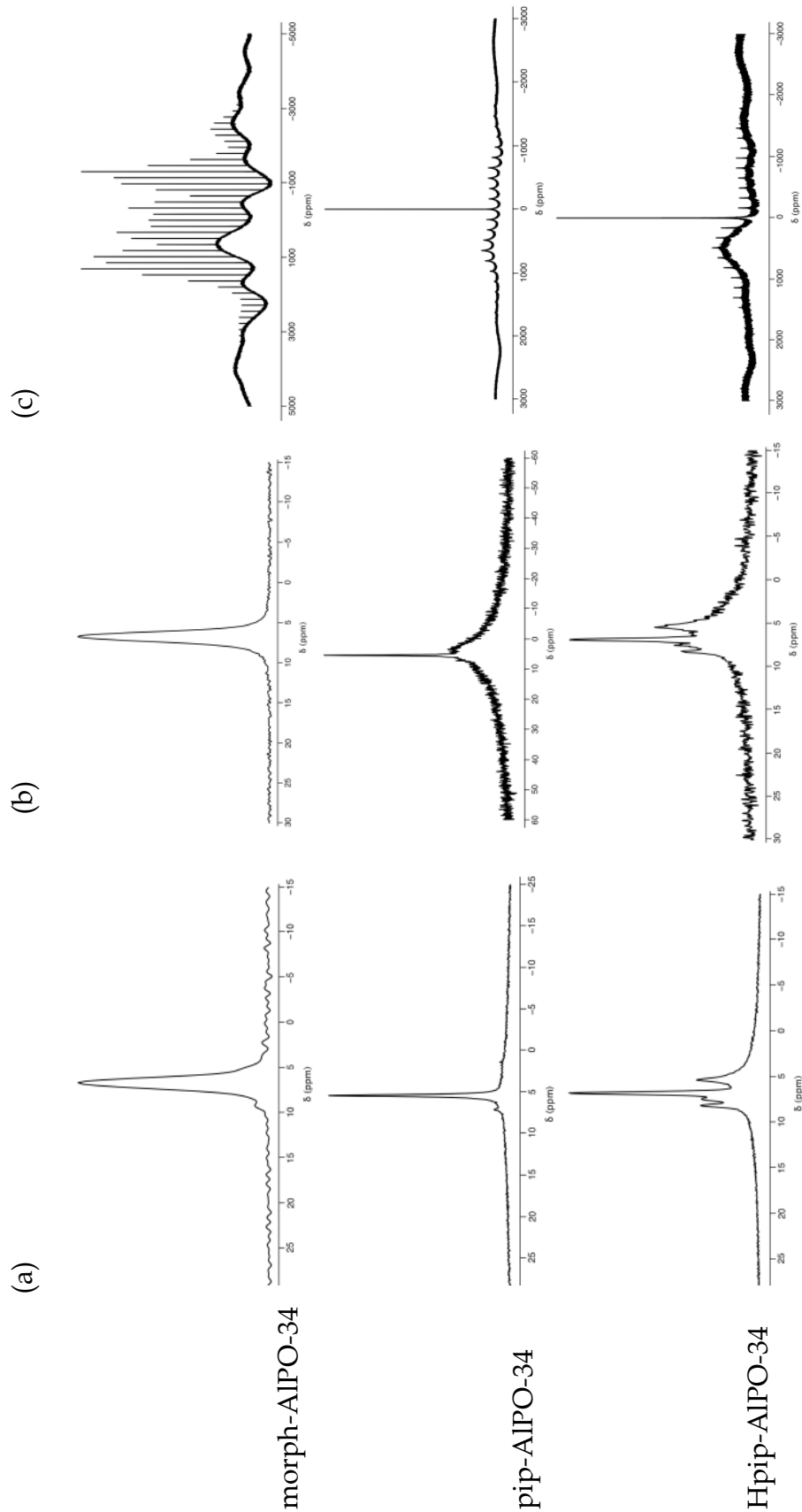


Figure 5.13 One-dimensional ^2H MAS NMR spectra recorded using (a) conventional, (b) rotor-synchronized acquisition and (c) recorded with wide spectral width of deuterated AlPO-34 samples. Spectra are the result of averaging 128 (morph) and 256 (pip and Hpip) transients. Recycle intervals of 5 s (morph) and 1s (pip and Hpip) were used. The MAS rate was 10 kHz.

of morph-AlPO-34 with a wide spectral width, presented in Fig. 5.13, shows a typical $I = 1$ Pake doublet split up into MAS sidebands. The width of this pattern is ~ 370 kHz. The ^2H MAS spectra of deuterated pip-AlPO-34 and Hpip-AlPO-34 with a wide spectral width also exhibit characteristic Pake doublet patterns but with lower intensity of the MAS sidebands than in the case of deuterated morph-AlPO-34. It can be assumed that this observation can be a result of the fast dynamic in deuterated morph-AlPO-34.

Since ^2H double-quantum NMR is a very useful technique to obtain information about dynamics, as mentioned previously, two-dimensional ^2H double-quantum (DQ) MAS NMR spectra were recorded in order to provide a very sensitive test for the presence of dynamics. The comparison of single- and double-quantum resonances is greatly facilitated if the two-dimensional experiment is performed in a rotor-synchronized manner in both the t_1 and t_2 time-domains, as explained in Chapter 3.

Figure 5.14 shows the two-dimensional ^2H DQMAS spectra of three deuterated samples. The spectrum in Fig. 5.14a reveals essentially the same linewidth in the single-quantum and double-quantum dimensions. This DQMAS spectrum might indicate very fast dynamics that are not detected using this experiment. However, one broad peak is seen in the single-quantum

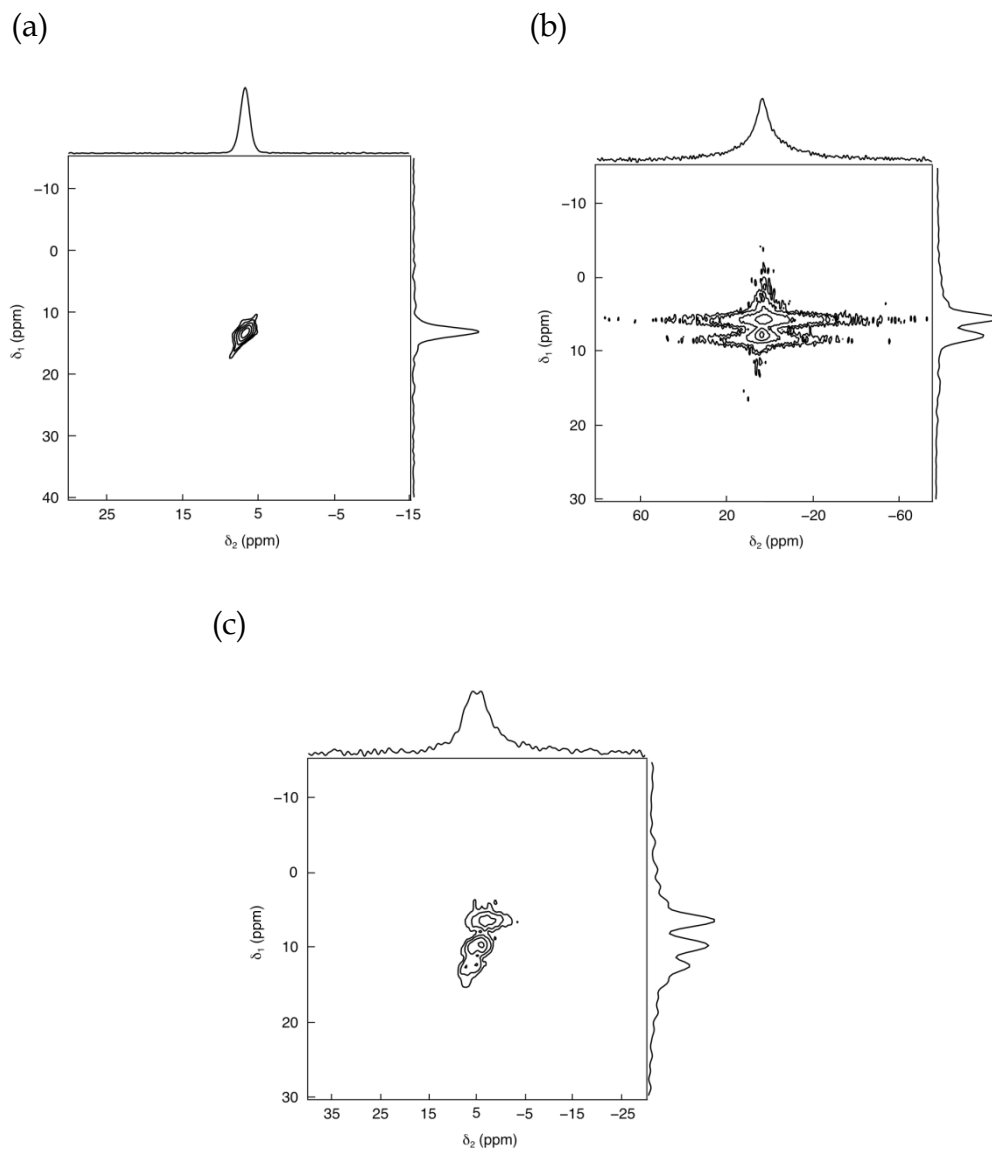


Figure 5.14 Two-dimensional ^2H double-quantum MAS NMR spectra (and δ_1 and δ_2 projections) of (a) morph-AlPO-34, (b) pip-AlPO-34 and (c) Hpip-AlPO034 recorded using rotor-synchronization in the t_1 and t_2 period. 32 transients were acquired for each of 200 t_1 increment of 100 μs . Recycle intervals the same as in one-dimensional ^2H MAS NMR spectra were used.

dimension of the two-dimensional ^2H DQMAS spectrum of deuterated pip-AlPO-34. This single peak observed in the single-quantum dimension is resolved in the double-quantum dimension indicating motion on the μs

timescale as was expected analysing ^2H one-dimensional spectrum which shows a broad peak for D_2O . The two-dimensional ^2H DQMAS spectrum of deuterated Hpip-AlPO-34 shows also only one broad peak in the single-quantum dimension, while three distinct motionally broadened peaks are observed in the double-quantum dimension. This result can confirm the presence of dynamic on the μs timescale from the dynamic reorientation of deuterated water molecules by 180° 'flips' about the C_2 axis.

5.2.3. Calcined AlPO-34

Calcination of either the pip- or morph-AlPO-34 materials results in removal of all template and water molecules to form calcined-dehydrated AlPO-34 and is achieved by heating the as-made material to a temperature of 500 - 600 °C. Full dehydration in turn is achieved by heating the calcined material for 2 h at 200 °C.

The unit cell of the calcined-dehydrated form has composition $\text{Al}_6\text{P}_6\text{O}_{24}$, with one crystallographically unique four-coordinated Al and P site. By calcination at about 500 °C, the organic species and HF are removed and the rhombohedral chabazite structure of AlPO-34 is formed [5.44]. Figure 5.1(a) shows the crystal structure of calcined-dehydrated AlPO-34. The sample

described here is calcined AlPO-34 from piperidine.

The one-dimensional ^{27}Al and ^{31}P MAS NMR spectra of calcined-dehydrated AlPO-34 are shown in Fig. 5.15. The ^{31}P spectrum of calcined dehydrated AlPO-34 shows one resonance at 31.1 ppm and it is consistent with the presence of one crystallographic site in that structure. However, although the ^{27}Al spectrum consists of one main peak, another component to the lineshape is also observed, which seems to look rather like an impurity. As it is not possible to assign the origin of the additional peak in the ^{27}Al MAS NMR spectrum by a simple lineshape analysis, a high-resolution ^{27}Al MQMAS spectrum of calcined-dehydrated AlPO-34 was recorded. Figure 5.16a displays the two-dimensional ^{27}Al MQMAS spectrum of calcined-dehydrated AlPO-34 recorded using phase-modulated split- t_1 pulse sequence. Only a single Al site with $C_Q = 3$ MHz and $\eta = 0.9$ is observed. It means that there is also only one crystallographic Al site within the structure of calcined-dehydrated AlPO-34 and this additional peak observed in one-dimensional spectrum originates from an impurity.

Figure 5.17 shows the ^{27}Al MAS NMR spectrum, along with the best fit to the second-order quadrupolar broadening lineshape, forcing one Al site to have $C_Q = 3$ MHz and $\eta = 0.9$ (as determined from the cross-section from

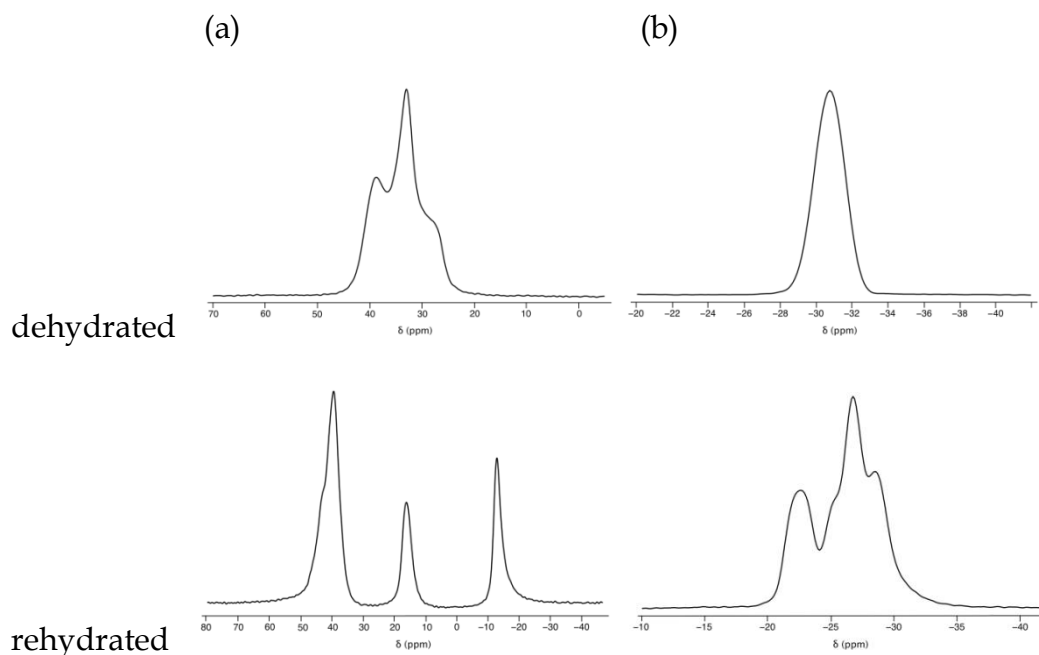


Figure 5.15 (a) ^{27}Al and (b) ^{31}P MAS NMR spectra of calcined dehydrated and rehydrated AlPO-34. ^{27}Al and ^{31}P spectra are the result of averaging 16 transients with recycle interval of 1 s and 4 transients with a recycle interval of 90 s, respectively.

MQMAS spectrum). The fitting uncovers a second Al population with 17% of the total intensity and small C_Q (which is probably the reason for the absence of this peak in the MQMAS spectrum). Therefore, this additional peak in the ^{27}Al MAS spectrum is assumed to be an impurity peak.

Since structural changes occurring upon hydration of an aluminophosphate framework are not well understood and their knowledge could have a practical impact because they usually modify the pore size and can have consequences for experimental techniques, further investigations on calcined AlPO-34 have been made. To ensure that the sample was fully

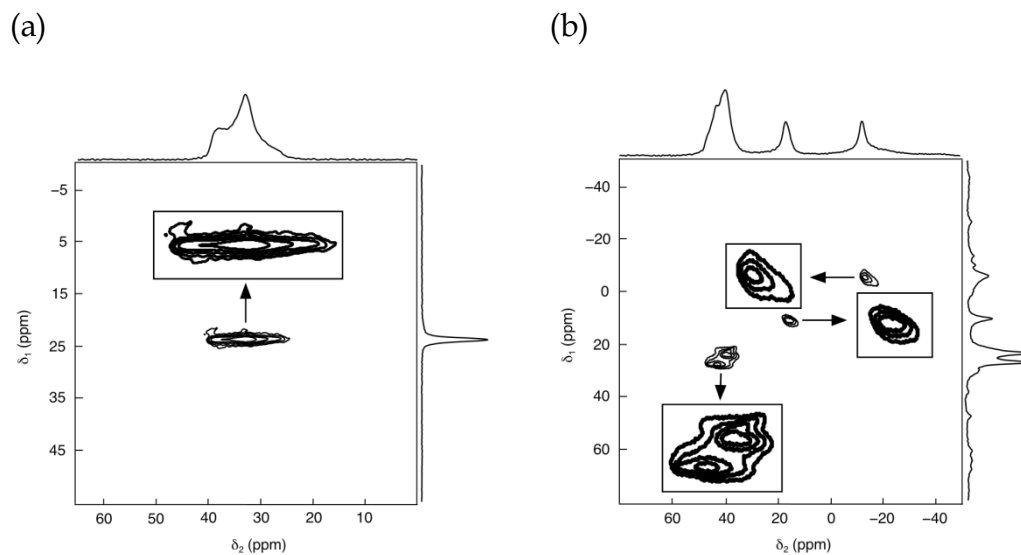


Figure 5.16 Two-dimensional ^{27}Al MQMAS (triple-quantum) spectrum of (a) calcined-dehydrated and (b) calcined-rehydrated AlPO-34. 96 transients were averaged for each of 256 t_1 values, with a t_1 increment of (a) 50 μs and (b) 12.5 μs and with a recycle interval of 1s. In (b) the time-proportional phase incrementation (TPPI) method of δ_1 sign discrimination and z-filter interval τ of 98.5 μs were used. The MAS rate was 10 kHz.

rehydrated, the open rotor was kept for three days because when the calcined material is contacted with air at room temperature, water molecules are absorbed.

The aim of recording the one-dimensional ^{27}Al and ^{31}P NMR spectra of calcined-rehydrated AlPO-34 shown in Fig. 5.15 was to observe how the sample behaves upon hydration and if the presence of water induces a motional broadening effect in these NMR spectra and change the local surroundings of the Al and P species. The ^{27}Al and ^{31}P spectra of the sample have been published previously [5.28].

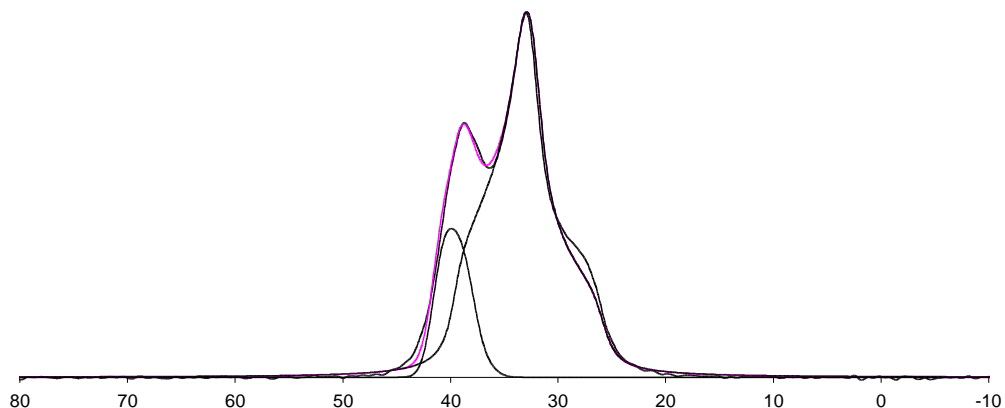


Figure 5.17 ^{27}Al MAS NMR spectrum of calcined dehydrated AlPO-34 fitted with the sum of two second-order quadrupolar broadening lineshapes.

The ^{31}P spectrum is composed of at least a few resonances between -20 and -30 ppm. This suggests the presence of at least four different environments for the P atoms in the unit cell. The ^{27}Al MAS NMR spectrum of fully rehydrated compound shows signals around 40 (4-coordinate), 16 (5-coordinate) and -12 ppm (6-coordinate). The first peak is more intense than the other peaks, indicating that this peak probably contains the resonances from two or more 4-coordinated Al sites. Therefore, the MQMAS spectrum was recorded once again to separate the contributions of the overlapping Al sites. The two-dimensional ^{27}Al MQMAS (triple-quantum) spectrum of calcined-rehydrated AlPO-34 recorded using an amplitude-modulated z-filter pulse sequence is displayed in Figure 5.16b. It can be observed that only four from six expected (from published data) [5.28] peaks are visible. Tuel et. al [5.28] recorded both ^{31}P and ^{27}Al NMR spectra and this ^{31}P MAS NMR spectrum is

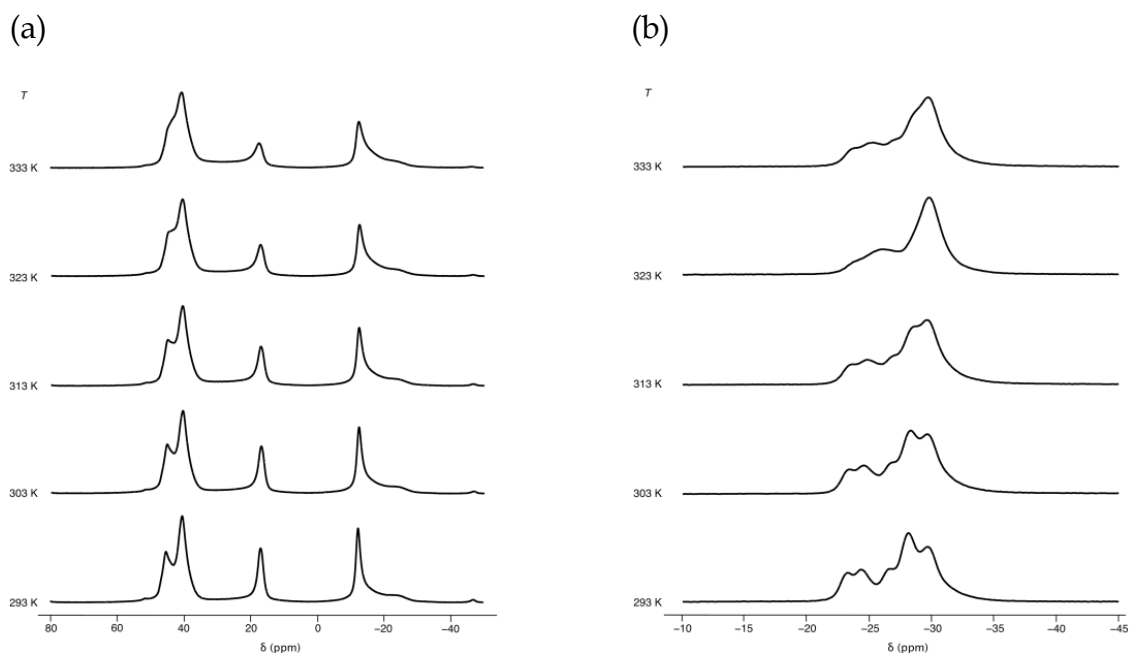


Figure 5.18 (a) ^{27}Al and (b) ^{31}P MAS NMR spectra of calcined-rehydrated AlPO-34 recorded at 14.1 T in the temperature range of 293 – 333 K. MAS rate was 10 kHz. ^{27}Al and ^{31}P spectra are the result of averaging 128 transients with recycle interval of 1 s and 8 transients with a recycle interval of 90 s, respectively.

composed of five lines between -22 and -28 ppm while in δ_1 dimension of ^{27}Al 5QMAS spectrum six resolved peaks is observed corresponding to three 4-coordinated, one 5-coordinated and two 6-coordinated Al species. Furthermore, they performed variable-temperature ^{27}Al and ^{31}P MAS experiments (between -20 °C and 50 °C) and did not observe any significant changes in the NMR spectra.

Therefore, the variable-temperature ^{27}Al and ^{31}P MAS NMR spectra were also recorded in the temperature range 293 – 333 K and they are presented in

Figure 5.18. It can be observed that the ^{27}Al linewidth increases with increasing temperature for all three Al sites and also the ^{31}P spectrum changes over the temperature range. The change between 293 and 303 K is probably due to a phase transition as found previously using X-ray powder diffraction [5.28]. However, the further change may be the effect of dynamic behaviour.

5.3. CASTEP calculations

Since the 1990s, *ab initio* computational tools have been used to study AlPO materials. First-principles calculations of NMR parameters of three as-made and calcined-dehydrated AlPO-34 were performed here using the NMR CASTEP code to combine DFT calculations with experimental data. The CASTEP program is a first-principles quantum-mechanical code for performing electronic structure calculations and it can be used to simulate a wide range of materials including amorphous materials.

CASTEP was used to calculate the isotropic chemical shifts of ^{27}Al , ^{31}P and ^{13}C within pip-, morph-, dmi-AlPO-34 and calcined-dehydrated AlPO-34, along with the quadrupolar NMR parameters C_Q and η of ^{27}Al .

As CASTEP does not calculate the chemical shift of a nucleus directly,

but its absolute shielding $\sigma_{\text{cal}}^{\text{sample}}$, it is necessary to calculate the shielding of a reference material (σ_{ref}) first in order to then convert the shielding of the sample into isotropic chemical shifts (δ_{iso}) according to the equation:

$$\delta_{\text{iso}} \approx \sigma_{\text{ref}} - \sigma_{\text{cal}}^{\text{sample}} \quad (5.2)$$

where the reference shielding is given by:

$$\sigma_{\text{ref}} \approx \delta_{\text{iso}}^{\text{ref}} + \sigma_{\text{cal}}^{\text{ref}} \quad (5.3)$$

and $\delta_{\text{iso}}^{\text{ref}}$ and $\sigma_{\text{cal}}^{\text{ref}}$ are isotropic chemical shift and calculated shielding for the reference material, respectively. The mineral berlinite was used as a reference material for ^{27}Al and ^{31}P and benzene was used as a reference material for ^{13}C .

The structural parameters (the unit cell and all atomic positions) for morph-AlPO-34 were obtained from the published crystal structure [5.24]. In the absence of a crystal structure for pip-AlPO, the conformation of the template in the pore was assumed to be the same as for morph-AlPO and a structure was generated by substituting an oxygen atom for a carbon atom. The CASTEP calculations for the third as-made AlPO-34 were performed by a

Table 5.1

Experimental and calculated ^{27}Al and ^{31}P isotropic chemical shifts (δ_{iso}) in ppm, quadrupolar coupling constants (C_Q) in MHz, asymmetry parameters (η) for three as-made AlPO-34 samples.

	pip-AlPO-34			morph-AlPO-34			dmi-AlPO-34		
	δ_{iso} (ppm)	C_Q / MHz	η	δ_{iso} (ppm)	C_Q / MHz	η	δ_{iso} (ppm)	C_Q / MHz	η
Experimental									
Al1	43.0	2.23	0.56	47.5	2.35	0.50	46.48	2.33	0.56
Al2	38.8	2.63	0.30	43.1	2.40	0.30	40.90	3.55	0.25
Al3	-5.02	1.76	0.80	-4.09	1.91	0.40	-4.95	1.91	0.80
P1	-9.03			-8.1			-7.73		
P2	-25.3			-24.1			-22.8		
P3	-31.2			-30.2			-28.9		
C1	47.3			65.4			134.1		
C2	22.6			46.1			125.2		
C3	—			—			36.9		
Calculated (no full geometry optimization)									
Al1	—	—	—	53.8	5.40	0.89	52.80	4.19	0.15
Al2	—	—	—	51.9	2.36	0.62	53.43	2.20	0.61
Al3	—	—	—	1.50	2.01	0.27	4.11	1.70	0.72

Table 5.1 (cont.)

P1	–			–6.10				–4.09	
P2	–			–23.5				–21.1	
P3	–			–30.4				–28.4	
C1	–			83.0				–	
C2	–			63.4				–	
C3	–			–				–	
Calculated (with full geometry optimization)									
Al1	42.8	3.76	0.61	49.2	3.91	0.51	48.44	4.71	0.66
Al2	37.2	2.76	0.77	43.7	2.95	0.30	48.76	2.30	0.48
Al3	–6.0	1.40	0.28	–0.30	1.19	0.40	0.61	2.54	0.16
P1	–5.05			–3.40				–1.06	
P2	–24.3			–23.0				–19.2	
P3	–33.0			–30.1				–25.2	
C1	47.5			65.9				132.8	
C2	22.1			44.1				125.0	
C3	–			–				32.9	

project student Lucy Clark of the University of St. Andrews. Table 5.1 lists the NMR parameters obtained from first-principles calculations and experiments for three as-made AlPO-34 samples. Geometry optimization was also performed within the CASTEP program. Using the DMFIT fitting program, the

lineshapes acquired were analysed so that experimental parameters could be extracted. From every one-dimensional spectrum fitting, the values of the asymmetry parameter, η , the quadrupolar coupling constant, C_Q , and the isotropic chemical shift, δ_{iso} , were obtained.

The resulting calculated parameters for as-made AlPO-34 were expected to agree with the experimental parameters and satisfactory agreement with the experimental values was achieved, especially if the structure geometry was optimized first.

Additionally, DFT calculations were combined with experimental data also for calcined-dehydrated AlPO-34 to study the structure modifications occurring during calcination of AlPO-34, for which a reasonably large ensemble of experimental information is known. Structural parameters (the unit cell and all atomic positions) of calcined-dehydrated AlPO-34 were obtained from published crystal structure [5.44]. Geometry optimization was also performed within the CASTEP program. Table 5.2 lists the NMR parameters obtained from first-principles calculation and experiment for calcined-dehydrated AlPO-34.

The resulting calculated parameters agree with the experimental values extracted from the ^{27}Al MQMAS experiment, even without prior geometry

Table 5.2

Experimental and calculated ^{27}Al and ^{31}P isotropic chemical shifts (δ_{iso}), quadrupolar coupling constants (C_Q), asymmetry parameters (η) for calcined-dehydrated AlPO-34.

	δ_{iso} (ppm)	C_Q / MHz	η
Experimental			
Al	39.6	3.0	0.90
P	-31.0		
Calculated (no optimization)			
Al	39.6	3.10	0.85
P	-28.9		
Calculated (geometry optimization)			
Al	40.3	3.10	0.87
P	-30.3		

optimization.

It is clear that in the case of the as-made AlPO-34 the geometry optimisation of the crystal structure is important in order to achieve more accurate results. It is typical to geometry optimise a crystal structure before

performing further DFT calculations since structural data obtained by diffraction often have high energies within the calculation and so geometry optimisation allows a unit cell to “relax”, reducing the forces acting on the atoms within the cell. However, when the templates have been removed from the pores, the calculated parameters agree with the experimental values without prior geometry optimization and therefore, the calculated parameters are expected to be more reliable. This is likely to be due to the fact that the structure of templated AlPO-34 samples is more complex than the structure of calcined-dehydrated AlPO-34. This observation is consistent with X-ray and NMR data.

5.4. GaPO-34 - gallium phosphate materials

Solid-state NMR of quadrupolar Ga nuclei (two isotopes of gallium are known, ^{69}Ga and ^{71}Ga ; both isotopes have spin $I = 3/2$, their natural abundances are 60.11% and 39.89%, and their Larmor frequencies at $B_0 = 9.4\text{ T}$ are 95.99 and 121.97 MHz, respectively) is a growing subject of interest for several reasons [5.45-5.48]. Quantitative measurements of quadrupolar nuclei are of great importance in the structural investigation of materials with a wide range of applications. In zeolitic materials or molecular sieves, Al/Ga substitution is

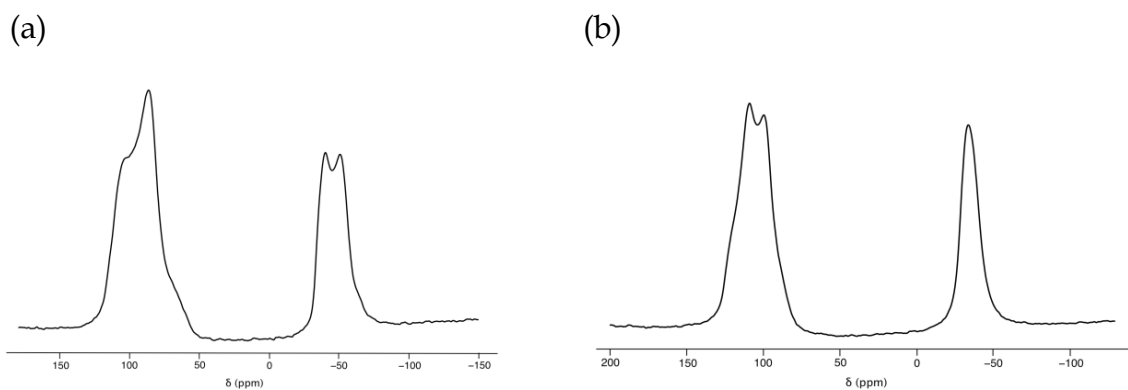


Figure 5.19 ^{71}Ga MAS NMR spectra of (a) mim-GaPO-34 and (b) py-GaPO-34. The spectra were recorded at 20.0 T using a 2.5-mm broadband MAS probe. Spectra are the result of averaging 512 transients. A recycle interval of 0.5 s was used.

used to tune or enhance application properties, typically as catalysts or microporous materials [5.49]. There is little known on Ga solid-state NMR, although there is a well established and confirmed correlation that links gallium and aluminium chemical shifts for four- and six-fold coordination in silicate, phosphates, zeolites and organic complexes [5.45,5.50]. The aim of this work was to identify the local surroundings of the different Ga species and to extract information about the effects of Ga substitution in AlPO-34 on dynamic behaviour. The ^{71}Ga MAS NMR spectra of py-GaPO-34 and mim-GaPO-34 have not yet been reported by other workers and this is the first investigation of GaPO-34 materials using NMR spectroscopy.

As ^{71}Ga and ^{69}Ga NMR experiments require special conditions to obtain interpretable spectra with fully resolved peaks, the experiments were acquired

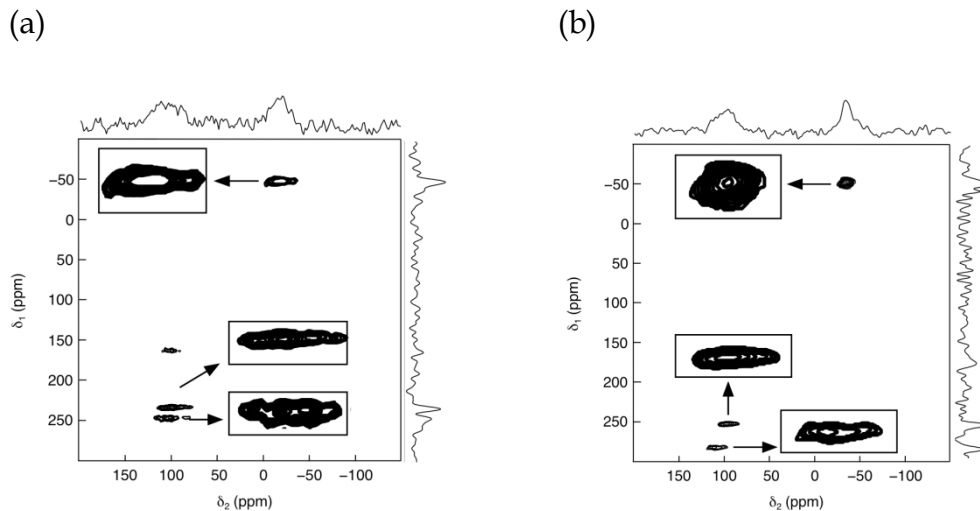


Figure 5.20 Two-dimensional ^{71}Ga MQMAS (triple-quantum) spectrum of (a) mim-GaPO-34 and (b) py-GaPO-34. MAS rate was 33 kHz. The spectra were recorded at 20.0 T using 2.5-mm broadband MAS probe. 480 transients were averaged for each 300 t_1 values, with a t_1 increment of 50 μs with a relaxation interval of 0.5 s. The State-Haberhorn-Ruben (States) method of δ_1 sign discrimination was used.

at high magnetic field and at fast spinning rates. Figure 5.19 presents one-dimensional ^{71}Ga MAS NMR spectra of both gallium phosphate samples recorded at 20.0 T.

The spectrum in Figure 5.19a shows two broad peaks at 95.5 and -45.3 ppm and they correspond to the 4- and 6-coordinated Ga species, respectively. The first peak is more intense than the peak at -45.3 ppm, indicating that this peak may contain the resonances from the two tetrahedral sites. Therefore a high-resolution ^{71}Ga MQMAS spectrum of mim-GaPO-34 was recorded in order to increase significantly the resolution of the spectrum. Figure 5.20a shows the

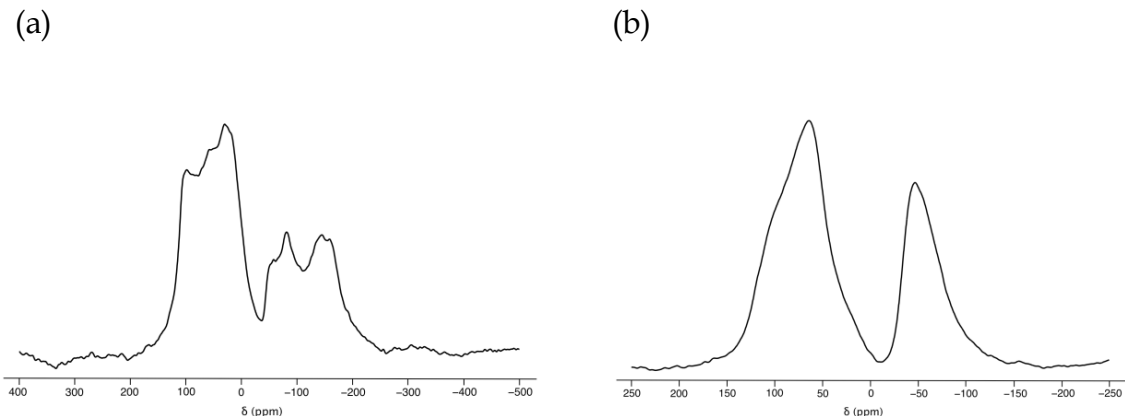


Figure 5.21 ^{69}Ga MAS NMR spectra of (a) mim-GaPO-34 and (b) py-GaPO-34. The spectra were recorded at 20.0 T using 1.3-mm broadband MAS probe. Spectra are the result of averaging 7200 transients. A recycle intervals of 0.5 s was used.

two-dimensional MQMAS spectrum of mim-GaPO-34. It can be observed that three peaks appear in the MQMAS spectrum corresponding to two 4-coordinated and one 6-coordinated gallium species. The ^{71}Ga MAS NMR spectrum of py-GaPO-34 shown in Fig. 5.19(b) also displays two broad lines at 105.2 and -34.1 ppm. However, the resonance at -34.1 ppm does not exhibit a lineshape characteristic of second-order quadrupolar broadening, as seen in Fig. 5.19a, but it shows slightly asymmetric lineshape. Once again the two-dimensional MQMAS spectrum of py-GaPO-34 was recorded to resolve overlapping peaks and it is presented in Fig. 5.20b. This spectrum shows two 4- and one 6-coordinated Ga species, as in the case of the first as-made GaPO-34.

As the gallium quadrupolar couplings are large, which gives rise to severe second-order broadening of the powder spectrum of its central transition

Table 5.3

^{71}Ga isotropic chemical shifts (δ_{iso}), quadrupolar coupling constants (C_Q) and asymmetry parameters (η) for mim- and py-GaPO-34.

	δ_{iso} (ppm)	C_Q / MHz	η
mim-GaPO-34			
Ga1	116.5	15.7	0.71
Ga2	107.8	14.0	0.83
Ga3	-29.76	13.3	0.30
py-GaPO-34			
Ga1	121.9	12.7	0.40
Ga2	110.8	12.0	0.70
Ga3	-26.38	9.02	0.90

as observed in one-dimensional spectra, therefore the cross-sections from MQMAS spectra were analysed, using the DMFIT fitting program, so that quadrupolar parameters could be extracted. In the case of 6-coordinated Ga species the one-dimensional spectra instead of cross-sections were analysed using DMFIT program. From each lineshape fitting, the values of the asymmetry parameter, η , the quadrupolar coupling constant C_Q and the isotropic chemical shift, δ_{iso} were obtained and results are presented in Table

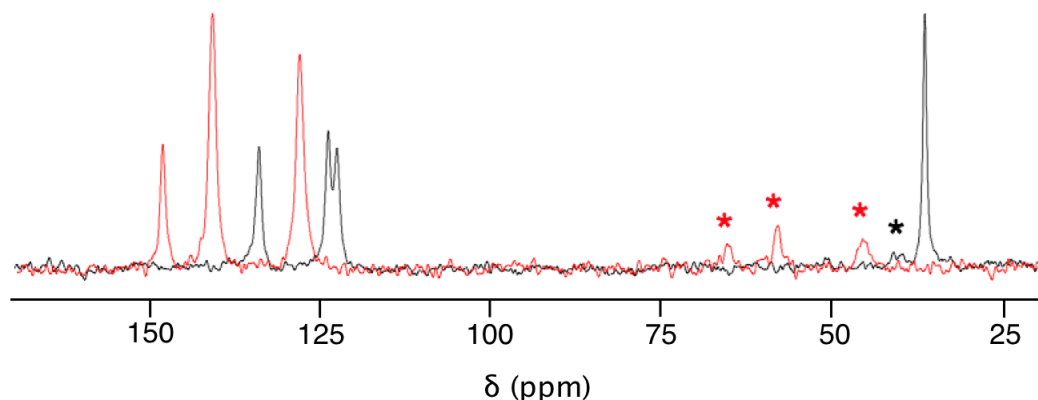


Figure 5.22 ^{13}C MAS NMR spectra of mim-GaPO-34 (black line) and py-GaPO-34 (red line). The MAS rate was 12.5 kHz. The spectra were recorded at 14.1 T using 2.5-mm broadband MAS probe. Spinning sidebands are denoted with asterisks. Spectra are the result of averaging 576 (mim-GaPO-34) and 384 (py-GaPO-34) transients with a recycle interval of 5 s and CP contact time of 1 ms (mim-GaPO-34) and 2 ms (py-GaPO-34). ^1H decoupling (TPPM-15, $\nu_{\text{rf}} = 100$ kHz) was applied during acquisition.

5.3. As the signal-to-noise ratio is low in the MQMAS spectra, larger errors are expected for those values. The quadrupolar coupling constants of all Ga sites are stronger for mim-GaPO-34. These results are consistent with the line broadening observed in ^{71}Ga MAS NMR spectra, especially in the case of 6-coordinated Ga site as the difference in these two linewidths is evident.

Furthermore, the one-dimensional ^{69}Ga MAS NMR spectra of mim-GaPO-34 and py-GaPO-34 were recorded and are displayed in Figure 5.21. Both spectra also show two broad peaks owing to the strong quadrupolar coupling. The spectrum in Fig. 5.21a exhibits second-order quadrupolar broadening lineshape while the spectrum in Fig. 5.21b shows asymmetric lineshapes of 4-

coordinated and 6-coordinated Ga species, similar to the ^{71}Ga MAS NMR spectra.

Figure 5.22 shows the one-dimensional ^{13}C MAS NMR spectra of mim-GaPO-34 and py-GaPO-34. The ^{13}C CPMAS NMR spectrum of mim-GaPO-34 contains three resonances at 134.2, 124.1, 122.8 corresponding to the carbons bonded to both nitrogen atoms and the other carbons from the ring linked to the NH group and those linked to the $\text{N}(\text{CH}_3)$ group, respectively, and one peak at 36.7 ppm assigned to methyl groups, as found in the literature [5.39]. The ^{13}C CPMAS NMR spectrum of py-GaPO-34 shows three resonances at 148.7, 141.5 and 128.7 ppm with linewidth of each of the peaks around 200 Hz. The chemical shifts of these three lines in the ^{13}C MAS NMR spectrum correspond to the two carbons bonded to the nitrogen atom, the other carbons located across from the nitrogen atom and all the other carbons in the ring, respectively [5.39].

Furthermore, the one-dimensional ^{31}P MAS NMR spectra of GaPO-34 samples were recorded and are presented in Fig. 5.23. The ^{31}P MAS NMR spectrum of both samples contains three resonances at -0.9 , -12.0 and -20.2 ppm for mim-GaPO-34 and at -0.8 , -13.8 and -20.5 ppm for py-GaPO-34 corresponding to tetrahedral P sites in the GaPO framework. The chemical shifts are very close to those of AlPO-34 suggesting the same structure of AlPO

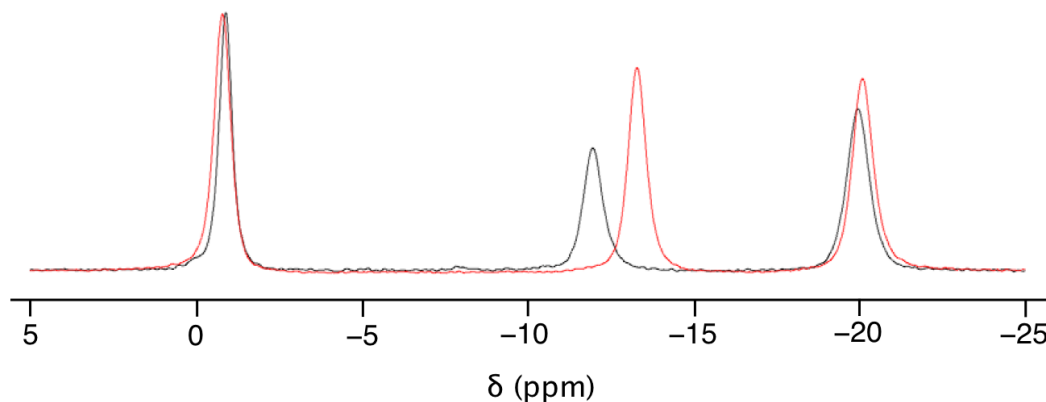


Figure 5.23 ^{31}P MAS NMR spectra of mim-GaPO-34 (black line) and py-GaPO-34 (red line). The MAS rate was 25 kHz. The spectra were recorded at 14.1 T. Spectra are the result of averaging 8 transients with a recycle interval of 60 s.

and GaPO frameworks.

5.5. Conclusion

Three as-made AlPO-34 samples have similar structure as they show the same number of crystallographically distinct Al and P sites in ^{27}Al and ^{31}P MAS NMR spectra. It means that template does not influence the AlPO framework. In the case of pip-, morph- and dmi-AlPO-34 the framework is composed of three Al sites (one 6-coordinated and two 4-coordinated) and three P sites (all 4-coordinated). These results are consistent with the literature and X-ray powder diffraction data.

It has been shown that the combination of MQMAS, STMAS and some

variable-temperature experiments permit useful interpretation of dynamic behaviour of the all samples.

The effect of calcination and on AlPO-34 materials has been also investigated and the first ^{27}Al , ^{31}P and ^2H MAS NMR spectra of deuterated pip- and morph-AlPO-34 are presented and interpreted here. ^{27}Al and ^{31}P MAS NMR spectra of calcined-dehydrated AlPO-34 show a single narrow peak (omitting an impurity) consistent with the structural determination. Previous publications confirm the presence of one Al and P sites within the sample.

However, as the NMR spectra of calcined-dehydrated AlPO-34 are clear and easy to interpret, the results of calcined-rehydrated material are difficult to explain. The changes occurring during the rehydration over specific temperature range can be interpreted as due to phase transition as found by Tuel et. al or due to dynamics. This is the first observation of this effect because the same NMR experiments have been performed previously but they did not indicate the presence of any phase transition or motion.

Since ^2H NMR spectroscopy became a simple way to probe motion on μs timescale, AlPO samples were also deuterated and ^2H NMR experiments were performed in order to observe dynamic behaviour of those samples. It has been

demonstrated here that in the case of deuterated morph-AlPO-34 motion are absent or faster than Larmor frequency so it is not possible to observe the effect of motional broadening or narrowing using described methods. On the other hand, in the case of either pip- or Hpip-AlPO-34 narrowing of the spinning sidebands in ^{27}Al MAS NMR spectra recorded with wide spectral width is present. Furthermore, ^2H DQMAS spectra of both materials indicate motion on μs timescale, probably due to D_2O or guest dynamic in framework solid. However, these results are complex and further work will have to be carried out to interpret the work presented here in more detail.

The first NMR results for GaPO-34 synthesized with pyridine and methylimidazole as the templates are also demonstrated here. Two-dimensional ^{71}Ga MQMAS NMR spectra of py- and mim-GaPO-34 show two tetrahedral and one octahedral Ga species. One-dimensional ^{31}P spectra show three tetrahedral P sites as in the case of as-made AlPO-34 samples. Interpretation of dynamic behaviour in GaPO materials is more difficult due to a very strong Ga quadrupolar coupling. Therefore, further experiments will have to be performed to extract more information about motion within GaPO-34 samples.

Additionally, CASTEP calculations presented here turned out to be very helpful in analysis of the experimental data.

Appendix A

Preparation of 9,12-diiodo-*ortho*-carborane

A stirred solution of *ortho*-carborane (0.291 g, 2.02 mmol) and iodine (0.513 g, 2.02 mmol) in glacial acetic acid (8 ml) was heated to 353 K and treated slowly with a mixture of conc. HNO₃ and conc. H₂SO₄ (1:1 *v/v* 5 ml). The solution produced a brown vapour and after 1 hr turned pale orange. The mixture was poured into distilled water (60 ml) and the precipitate was washed with water and then dissolved in ether. The ether was then evaporated from the solution. The product was then recrystallized using hexane to give 187 mg (23.4% yield) of 9,12-diiodo-*ortho*-carborane (C₂H₁₀B₁₀I₂).

Preparation of pip-AlPO-34

The reactants used to synthesize pip-AlPO-34 were piperidine, phosphoric acid, hydrofluoric acid, and aluminum isopropoxide. The relative molar composition of the reaction mixture used in the preparation of pip-AlPO-34 was Al₂O₃:P₂O₅: HF: 2 piperidine: 100 H₂O. The mixture was prepared by successive addition of phosphoric acid, hydrofluoric acid, and piperidine to a suspension of aluminum isopropoxide in water with constant stirring. The crystallization

was performed at 190°C for 4 days under static conditions. The products were recovered, washed with deionized water, filtered and dried at 70°C in air overnight.

Preparation of dim-AlPO-34 (SIZ-4)

A sample of SIZ-4 was prepared by adding a 1-butyl-3methylimidazolium bromide ionic liquid along with aluminium isopropoxide, phosphoric acid and hydrofluoric acid to a Teflon-lined steel autoclave. The autoclave was then heated in an oven to the necessary temperature for the required time. Once the reaction was complete, the autoclave was removed from the oven and allowed to cool to room temperature. The product was filtered and washed with water and acetone.

Appendix B

Coefficients of zero-, second- and fourth-rank terms in Eqn. (3.8) for half-integer spin nuclei

	m_I	$A^0(I, m_I)$	$A^2(I, m_I)$	$A^4(I, m_I)$
$I = 3/2$	$1/2$	$-2/5$	$-8/7$	$54/35$
	$3/2$	$6/5$	0	$-6/5$
$I = 5/2$	$1/2$	$-16/15$	$-64/21$	$144/35$
	$3/2$	$-4/5$	$-40/7$	$228/35$
	$5/2$	$20/3$	$40/21$	$-60/7$
$I = 7/2$	$1/2$	$-30/15$	$-120/21$	$270/35$
	$3/2$	$-54/15$	$-96/7$	$606/35$
	$5/2$	$30/15$	$-240/21$	$330/35$
	$7/2$	$294/15$	$168/21$	$-966/35$
$I = 9/2$	$1/2$	$-48/15$	$-192/21$	$432/35$
	$3/2$	$-108/15$	$-168/7$	$1092/35$
	$5/2$	$-60/15$	$-600/21$	$1140/35$
	$7/2$	$168/15$	$-336/21$	$168/35$
	$9/2$	$648/15$	$432/21$	$-2332/35$

Appendix C

Reduced Rotation Matrix Elements

$$l = 1$$

$$d_{1,-1}^1(\beta) = d_{-1,1}^1(\beta) = \frac{1}{2}(1 - \cos\beta)$$

$$d_{1,1}^1(\beta) = d_{-1,-1}^1(\beta) = \frac{1}{2}(1 + \cos\beta)$$

$$d_{0,1}^1(\beta) = d_{-1,0}^1(\beta) = d_{0,-1}^1(\beta) = d_{1,0}^1(\beta) = \frac{1}{\sqrt{2}} \sin\beta$$

$$d_{0,0}^1(\beta) = \cos\beta$$

$$l = 2$$

$$d_{2,2}^2(\beta) = d_{-2,-2}^2(\beta) = \cos^4(\beta/2)$$

$$d_{2,1}^2(\beta) = -d_{1,2}^2(\beta) = -d_{-2,-1}^2(\beta) = -d_{-1,-2}^2(\beta) = -\frac{1}{2} \sin\beta(1 + \cos\beta)$$

$$d_{2,0}^2(\beta) = d_{0,2}^2(\beta) = d_{-2,0}^2(\beta) = d_{0,-2}^2(\beta) = \frac{\sqrt{3}}{\sqrt{8}} \sin^2 \beta$$

$$d_{2,-1}^2(\beta) = d_{1,-2}^2(\beta) = -d_{-2,1}^2(\beta) = -d_{-1,2}^2(\beta) = -\frac{1}{2} \sin\beta(1 - \cos\beta)$$

$$d_{2,-2}^2(\beta) = d_{-2,2}^2(\beta) = \sin^4(\beta/2)$$

$$d_{1,1}^2(\beta) = d_{-1,-1}^2(\beta) = -\frac{1}{2} (1 - 2 \cos\beta)(1 + \cos\beta)$$

$$d_{1,-1}^2(\beta) = d_{-1,1}^2(\beta) = \frac{1}{2} (1 + 2 \cos\beta)(1 - \cos\beta)$$

$$d_{1,0}^2(\beta) = d_{0,-1}^2(\beta) = -d_{0,1}^2(\beta) = -d_{-1,0}^2(\beta) = -\frac{\sqrt{3}}{\sqrt{2}} \sin\beta \cos\beta$$

$$d_{0,0}^2(\beta) = \frac{1}{2} (3 \cos^2 \beta - 1)$$

l = 4

$$d_{0,0}^4(\beta) = \frac{1}{8} (35 \cos^4 \beta - 30 \cos^2 \beta + 3)$$

$$d_{0,2}^4(\beta) = d_{2,0}^4(\beta) = -\frac{\sqrt{10}}{128} (14 \cos 4\beta - 8 \cos 2\beta - 6)$$

$$d_{0,4}^4(\beta) = d_{4,0}^4(\beta) = -\frac{\sqrt{70}}{128} (\cos 4\beta - 4 \cos 2\beta + 3)$$

Appendix D

MQMAS ratios ($A^4(I,m)/A^4(I,1/2)$) for half-integer spin nuclei.

Spin I	Three-quantum	Five-quantum	Seven-quantum	Nine-quantum
3/2	- 7/9			
5/2	19/12	- 25/12		
7/2	101/45	11/9	- 161/45	
9/2	91/36	95/36	7/18	- 31/6

Appendix E

STMAS ratios $R(I,q)$, for $m_I = \pm (q - 1) \leftrightarrow \pm q$ single-quantum transitions.

I	q	$R(I,q)$
3/2	3/2	- 8/9
5/2	3/2	7/24
	5/2	- 11/6
7/2	3/2	28/45
	5/2	-23/45
	7/2	-12/5
9/2	3/2	55/72
	5/2	1/18
	7/2	-9/8
	9/2	-25/9

References

- [1.1] E. M. Purcell, H. C. Torrey, R. V. Pound, *Phys. Rev.* **69**, 37 (1946).
- [1.2] F. Bloch, W. W. Hansen, M. Packard, *Phys. Rev.* **70**, 474 (1946).
- [1.3] J. T. Arnold, S. S. Dharmatti, M. E. Packard, *J. Chem. Phys.* **19**, 507 (1951).
- [1.4] E. R. Andrew, A. Bradbury, R. G. Eades, *Nature* **182**, 1659 (1958).
- [1.5] E. R. Andrew, A. Bradbury, R. G. Eades, *Nature* **183**, 1802 (1959).
- [1.6] I. J. Lowe, *Phys. Rev. Lett.* **2**, 258 (1959).
- [1.7] S. R. Hartmann, E. L. Hahn, *Phys. Rev.* **128**, 2042 (1962).
- [1.8] R. R. Ernst, W. A. Anderson, *Rev. Sci. Instr.* **37**, 93 (1966).
- [1.9] J. Jeener, Ampere International Summer School, Basko Polje, Yugoslavia, (1971).
- [1.10] E. D. Ostroff, J. S. Waugh, *Phys. Rev. Lett.* **16**, 1097 (1966).
- [1.11] P. Mansfield, D. Ware, *Phys. Letters* **22**, 133 (1966).
- [1.12] A. Llor, J. Virlet, *Chem. Phys. Lett.* **152**, 248 (1988).
- [1.13] A. Samoson, A. Lippmaa, A. Pines, *Mol. Phys.* **65**, 1013 (1988).
- [1.14] A. Samoson, A. Lippmaa, *J. Magn. Reson.* **84**, 410 (1989).
- [1.15] K. T. Mueller, B. Q. Sun, G. C. Chingas, J. W. Zwanziger, T. Terao, A. Pines, *J. Magn. Reson.* **86**, 248 (1990).
- [1.16] L. Frydman, J. S. Harwood, *J. Am. Chem. Soc.* **117**, 5367 (1995).
- [1.17] P. R. Bodart, J. Parmentier, R. K. Harris, D. P. Thompson *J. Phys. Chem. Solids* **60**, 223 (1999).
- [1.18] H. Kraus, R. Prins, A. P. M. Kentgens, S. Wimperis, *J. Phys. Chem.* **100**, 16336 (1996).
- [1.19] L. Marinelli, L. Frydman, *Chem. Phys. Lett.* **275**, 188 (1997).
- [1.20] Z. Gan, *J. Am. Chem. Soc.* **122**, 3242 (2000).

- [1.21] M. C. Payne, M. P. Teter, D. C. Allan, T. A. Arias, J. D. Joannopoulos, *Rev. Mod. Phys.* **64**, 1045 (1992).
- [2.1] F. Bloch, *Phys. Rev.* **70**, 460 (1946).
- [2.2] R. R. Ernst, W. A. Anderson, *Rev. Sci. Instr.* **37**, 93 (1966).
- [2.3] A. E. Derome, in "Modern NMR Techniques for Chemistry Research", p. 13, Pergamon Press, Oxford, 1991.
- [2.4] A. Abragam, in "Principles of Nuclear Magnetism", p. 33, Oxford, Science Publications, 1961.
- [2.5] A. E. Derome, in "Modern NMR Techniques for Chemistry Research", p. 77, Pergamon Press, Oxford, 1991.
- [2.6] M. J. Duer, in "Introduction to Solid-State NMR Spectroscopy", Chapter 4, Blackwell Publishing, Oxford, 2004.
- [2.7] M. Mehring, A. Pines, W. K. Rhim, J. S. Waugh, *J. Chem. Phys.* **54**, 3239 (1971).
- [2.8] A. Abragam, in "Principles of Nuclear Magnetism", p. 480-495, Oxford, Science Publications, 1961.
- [2.9] E. R. Andrew, in "Encyclopedia of Nuclear Magnetic Resonance" (D. M. Grant and R. K. Harris, Eds.), Vol. 5, p. 2891, Wiley, Chichester, 1996.
- [2.10] P. J. Hore, in "Nuclear Magnetic Resonance", p. 9, Oxford University Press, Oxford, 1995.
- [2.11] A. J. Vega, in "Encyclopedia of Nuclear Magnetic Resonance" (D. M. Grant and R. K. Harris, Eds.), Vol. 6, p. 3869, Wiley, Chichester, 1996.
- [2.12] P. P. Man, in "Encyclopedia of Nuclear Magnetic Resonance" (D. M. Grant and R. K. Harris, Eds.), Vol. 6, p. 3838, Wiley, Chichester, 1996.
- [2.13] J. P. Amoureux, *Solid State Nucl. Magn. Reson.* **2**, 83 (1993).
- [2.14] A. Abragam, in "Principles of Nuclear Magnetism", p. 232, Oxford,

Science Publications, 1961.

- [2.15] P. W. Atkins, R. S. Friedman, in "Molecular Quantum Mechanics", Chap. 6, Oxford University Press, Oxford, 1997.
- [2.16] S. E. Ashbrook, S. Wimperis, *J. Magn. Reson.* **177**, 44 (2005).
- [2.17] S. Samoson, E. Lippmaa, *J. Magn. Reson.* **84**, 410 (1989).
- [2.18] R. N. Zare, in "Angular Momentum", Chap. 5, Wiley, Chichester, 1996.
- [2.19] H. A. Buckmaster, *Can. J. Phys.* **42**, 386 (1964).
- [2.20] R. N. Zare, in "Angular Momentum", Chap. 2, Wiley, Chichester, 1987.
-
- [3.1] J. Keeler, in "Understanding NMR Spectroscopy", Chap. 9, Wiley, Chichester, 2005.
- [3.2] S. P. Brown, S. Wimperis, *Chem. Phys. Lett.* **237**, 509 (1995).
- [3.3] E. R. Andrew, in "Encyclopedia of Nuclear Magnetic Resonance" (D. M. Grant and R. K. Harris, Eds.), Vol. 5, p. 2891, Wiley, Chichester, 1996.
- [3.4] A. Abragam, in "Principles of Nuclear Magnetism", p. 480-495, Oxford Science Publications, 1961.
- [3.5] S. E. Ashbrook, M. J. Duer, *Concepts Magn. Reson.* **A 28**, 183 (2006).
- [3.6] R. R. Ernst, G. Bodenhausen, and A. Wokaun, in "Principles of Nuclear Magnetic Resonance in One and Two Dimensions", Chap. 6, Clarendon Press, Oxford, 1987.
- [3.7] C. Fernandez, J. P. Amoureux, *Solid State NMR* **5**, 315 (1996).
- [3.8] D. Marion, K. Wüthrich, *Biochem. Biophys. Res. Commun.* **113**, 967 (1983).
- [3.9] D. J. States, R. A. Haberkorn, D. J. Ruben, *J. Magn. Reson.* **48**, 286

- (1982).
- [3.10] J. P. Amoureux, C. Fernandez, J. Steuernagel, *J. Magn. Reson.* **A 123**, (1996).
- [3.11] O. W. Sørensen, M. Rance, R. R. Ernst, *J. Magn. Reson.* **56**, 527 (1984).
- [3.12] S. P. Brown, S. J. Heyes, S. Wimperis, *J. Magn. Reson.* **A119**, 280 (1996).
- [3.13] P. J. Grandinetti, J. H. Baltisberger, J. Stebbins, U. Werner, M. A. Eastman, A. Pines, *Mol. Phys.* **81**, 1109 (1994).
- [3.14] S. P. Brown, S. Wimperis, *J. Magn. Reson.* **128**, 42 (1997).
- [3.15] D. Massiot, B. Touzo, D. Trumeau, J. P. Coutures, J. Virlet, P. Florian, P. J. Grandinetti, *Solid State NMR* **6**, 73 (1996).
- [3.16] P. K. Madhu, A. Goldburt, L. Frydman, S. Vega, *Chem. Phys. Lett.* **307**, 41 (1999).
- [3.17] Z. Gan, H. T. Kwak, *Solid State NMR* **20**, 87 (2001).
- [3.18] T. J. Ball, S. Wimperis, *J. Magn. Reson.* **187**, 343 (2007).
- [3.19] P. R. Bodart, J. Parmentier, R. K. Harris, D. P. Thompson *J. Phys. Chem. Solids* **60**, 223 (1999).
- [3.20] H. Kraus, R. Prins, A. P. M. Kentgens, *J. Phys. Chem.* **100**, 16336 (1996).
- [3.21] G. Wu, S. Kroeker, R. E. Wasylshen, R. G. Griffin, *J. Magn. Reson.* **128**, 237 (1997).
- [3.22] L. Marinelli, L. Frydman, *Chem. Phys. Lett.* **275**, 188 (1997).
- [3.23] R. Freeman, in "A Handbook of Nuclear Magnetic Resonance", 2nd ed., p. 88, Longman, Harlow, 1997.
- [3.24] S. E. Ashbrook, S. Wimperis, *Prog. Nucl. Magn. Reson. Spectrosc.* **45**, 53 (2004).
- [3.25] H. T. Kwak, Z. Gan, *J. Magn. Reson.* **164**, 369 (2003).
- [3.26] N. G. Dowell, S. E. Ashbrook, S. Wimperis, *J. Phys. Chem.* **B 108**, 13292 (2004).
- [3.27] C. Fernandez, L. Delevoye, J. P. Amoureux, D. P. Lang, M. Pruski,

- J. Am. Chem. Soc.* **119**, 6858 (1997).
- [3.28] M. Pruski, D. P. Lang, C. Fernandez, J. P. Amoureux, *Solid State Nucl. Magn. Reson.* **7**, 327 (1997).
- [3.29] G. A. Morris, R. J. Freeman, *J. Am. Chem. Soc.* **101**, 760 (1979).
- [3.30] D. T. Pegg, D. M. Doddrell, W. M. Brooks, M. R. J. Bendall, *J. Magn. Reson.* **44**, 32 (1981).
- [3.31] J. P. Amoureux, J. Trebosc, J. Wiench, M. Pruski, *J. Magn. Reson.* **184**, 1 (2007).
- [3.32] J. Keeler, in "Understanding NMR Spectroscopy", Chap. 7, Wiley, Chichester, 2005.
- [3.33] C. A. Fyfe, K. C. Wongmoon, Y. Huang, H. Grondey, *J. Am. Chem. Soc.* **117**, 10397 (1995).
- [3.34] Y. S. Yen, D. P. Weitekamp, *J. Magn. Reson.* **47**, 476 (1982).
- [3.35] L. Müller, *Chem. Phys. Lett.* **91**, 303 (1982).
- [3.36] A. Lesage, L. Emsley, *J. Magn. Reson.* **148**, 449 (2001).
- [3.37] R. Kemp-Harper, D. J. Philp, P. W. Kuchel, *J. Chem. Phys.* **115**, 2908 (2001).
- [4.1] M. J. Duer, in "Introduction to Solid-State NMR Spectroscopy", Chapter 6, Blackwell Publishing, Oxford, 2004.
- [4.2] R. R. Ernst, G. Bodenhausen and A. Wokaun, in "Principles of Nuclear Magnetic Resonance in One and Two Dimensions", Clarendon, Oxford, 1987.
- [4.3] J. Jeener, B. H. Meier, P. Bachmann, R. R. Ernst, *J. Chem. Phys.* **71**, 4546 (1979).
- [4.4] L. S. Cahill, R. P. Chapman, J. F. Britten, G. R. Goward, *J. Phys. Chem.* **B110**, 7171 (2006).

- [4.5] F. Wang, G. P. Grey, *J. Am. Chem. Soc.* **120**, 970 (1998).
- [4.6] S. Chaudhuri, F. Wang, C. P. Grey, *J. Am. Chem. Soc.* **124**, 11746 (2002).
- [4.7] N. Kim, R. N. Vannier, C. P. Grey, *Chem. Mater.* **17**, 1952 (2005)
- [4.8] J. Cabana, N. Dupre, G. Rousse, C. P. Grey, M. R. Palacin, *Solid State Ionics* **176**, 2205 (2005).
- [4.9] H. S. Gutowsky, G. E. Pake, *J. Chem. Phys.* **18**, 162 (1950).
- [4.10] E. R. Andrew, *J. Chem. Phys.* **18**, 607 (1950).
- [4.11] M. M. Maricq, J. S. Waugh, *J. Chem. Phys.* **70**, 3300 (1979).
- [4.12] S. E. Ashbrook, S. Antonijevic, A. J. Berry, S. Wimperis, *Chem. Phys. Lett.* **364**, 634 (2002).
- [4.13] S. Antonijevic, S. E. Ashbrook, S. Biedasek, R. I. Walton, S. Wimperis, H. Yang, *J. Am. Chem. Soc.* **128**, 8054 (2006).
- [4.14] M. J. Thrippleton, M. Cutajar, S. Wimperis, *Chem. Phys. Lett.* **452**, 233 (2008).
- [4.15] J. H. Kristensen, G. L Hoatson, R. L. Vold *Solid State NMR* **13**, 1 (1998).
- [4.16] M. Hologne, J. Hirschinger *Solid State NMR* **26**, 1 (2004).
- [4.17] B. C. Gerstein, in "Encyclopaedia of Nuclear Magnetic Resonance" (D. M. Grant and R. K. Harris, Eds.), p. 1835, Wiley, Chichester, 1996.
- [4.18] J. H. Davis, K. R. Jeffrey, M. Bloom, M. I. Valic, T. P. Higgs, *Chem. Phys. Lett.* **42**, 390 (1976).
- [4.19] L. W. Jelinski, J. J Dumais, A. K. Engel, *Macromolecules* **16**, 492 (1983).
- [4.20] M. J. Duer, C. Stourton, *J. Magn. Reson.* **129**, 44 (1997).
- [4.21] M. Cutajar, S. E. Ashbrook, S. Wimperis, *Chem. Phys. Lett.* **423**, 276 (2006).
- [4.22] J. M. Griffin, A. J. Miller, A. J. Berry, S. Wimperis, S. E. Ashbrook *Phys. Chem. Chem. Phys.* **12**, 2989 (2010).
- [4.23] T. Bräuniger, R. Poupko, H. Zimmermann, Z. Luz *J. Chem. Soc.* **2**,

- 1255 (1997).
- [4.24] G. H. Penner, J. M. Polson, *J. Chem. Soc., Dalton Trans.* 803 (1993).
- [4.25] T. Chang, Ch. P. Cheng, Ch. Yeh, *J. Chem. Soc.* **90**, 1157 (1994).
- [4.26] Ch. F. Lee, L. K. Myers, K. G. Valentine, M. E. Thompson *J. Chem. Soc., Chem. Commun.* 201 (1992).
- [4.27] H. T. Edzes, W. S. Veeman, *Polymer Bulletin* **5**, 255 (1981).
- [4.28] B. C. Perry, J. L. Koenig, J. B. Lando, *Macromolecules* **20**, 422 (1987).
- [4.29] J. R. Garbow, J. Schaefer, *Macromolecules* **20**, 819 (1987).
- [4.30] J. Bonmatin, I. C. P. Smith, H. C. Jarrell, D. J. Siminovitch, *J. Am. Chem. Soc.* **110**, 8693 (1988).
- [4.31] D. J. Siminovitch, M. J. Ruocco, E. T. Olejniczak, S. K. Das Gupta, R. G. Griffin, *Biophys. J.* **54**, 373 (1988).
- [4.32] P. P. Man, in "Encyclopedia of Nuclear Magnetic Resonance" (D. M. Grant and R. K. Harris, Eds.), p. 3838, Wiley, Chichester, 1996.
- [4.33] M. J. Duer, in "Introduction to Solid-State NMR Spectroscopy", Chapter 5, Blackwell Publishing, Oxford, 2004.
- [4.34] U. Eliav, G. Navon, *J. Chem. Phys.* **95**, 7114 (1991).
- [4.35] R. Poupko, A. Baram, Z. Luz, *Mol. Phys.* **27**, 1345 (1974).
- [4.36] L. G. Werbelow, *J. Chem. Phys.* **70**, 5381 (1979).
- [4.37] P. O. Westlund, H. Wennerström, *J. Magn. Reson.* **50**, 451 (1982).
- [4.38] L. Werbelow, R. E. London, *Concepts in Magn. Reson.* **8**, 325 (1996).
- [4.39] J. L. Bjorkstam, P. Ferloni, M. Villa, *J. Chem. Phys.* **73**, 2932 (1980).
- [4.40] D. Brinkmann, M. Mali, J. Roos, R. Messer, H. Birli, *Phys. Rev.* **B 26**, 4810 (1982).
- [4.41] M. Witschas, H. Eckert, *J. Phys. Chem.* **A 103**, 10764 (1999).
- [4.42] E. C. Reynhardt, S. Froneman, *Mol. Phys.* **74**, 61 (1991).
- [4.43] P. Beckmann, A. J. Leffler, *J. Chem. Phys.* **72**, 4600 (1980).
- [4.44] R. K. Harris, J. Bowles, I. R. Stephenson, E. H. Wong, *Spectrochimica*

- Acta* **A 44**, 273 (1988).
- [4.45] U. Eliav, H. Shinar, G. Navon, *J. Magn. Reson.* **94**, 439 (1991).
- [4.46] L. Frydman, J. S. Harwood, *J. Am. Chem. Soc.* **117**, 5367 (1995).
- [4.47] S. Wimperis, *J. Magn. Reson. A* **102**, 302 (1993).
- [4.48] T. Kurkiewicz, M. J. Thrippleton, S. Wimperis, *Chem. Phys. Lett.* **467**, 412 (2009).
- [4.49] M. C. Payne, M. P. Teter, D. C. Allan, T. A. Arias, J. D. Joannopoulos, *Rev. Mod. Phys.* **64**, 1045 (1992).
- [4.50] J. Keeler, in "Understanding NMR Spectroscopy", Chap. 9, Wiley, Chichester, 2005.
- [4.51] A. J. Leffler, *J. Chem. Phys.* **63**, 3971 (1975).
- [4.52] M. Winterlich, R. Böhmer, *J. Chem. Phys.* **123**, 094504 (2005).
- [4.53] L. A. Leites, *Chem. Rev.* **92**, 279 (1992).
- [4.54] H. P. Diogo, N. T. Correia, J. J. M. Ramos, *J. Phys. Chem. Solids* **66**, 832 (2005).
- [5.1] S. T. Wilson, B. M. Lok, C. A. Messina, T. R. Cannan, E. M. Flanigen, *J. Am. Chem. Soc.* **104**, 1146 (1971).
- [5.2] S. T. Wilson, B. M. Lok, C. A. Messina, T. R. Cannan, E. M. Flanigen, *ACS Symp. Ser.* **218**, 79 (1983).
- [5.3] Y. Li, J. Yu, R. Xu, <http://mezeopor.jlu.edu.cn/alpo> and references therein.
- [5.4] J. M. Thomas, Y. Xu, C. R. A. Catlow, J. W. Couves, *Chem. Mater.* **3**, 667 (1991).
- [5.5] Y. Xu, C. P. Grey, J. M. Thomas, A. K. Cheetham, *Catal. Lett.* **4**, 251 (1990).
- [5.6] M. Stocker, *Microporous Mesoporous Mater.* **29**, 3 (1999).
- [5.7] J. M. Thomas, R. Raja, G. Sankar, R. G. Bell, *Nature* **398**, 227 (1999).
- [5.8] J. M. Thomas, R. Raja, G. Sankar, R. G. Bell, *Acc. Chem. Res.* **34**, 191 (2001).

- [5.9] http://izasc.ethz.ch/fmi/xsl/iza-sc/ftc_fw.xsl?-db=Atlas_main&-lay=fw&STC=CHA&-find
- [5.10] M. Zema, S. C. Tarantino, G. Montagna, *Chem. Mater.* **20**, 5876 (2008).
- [5.11] H. Kessler, in "Synthesis, Characterization and Novel Applications of Molecular Sieve Materials" (R. L. Bedard et al., Eds), p. 47, Materials Research Society, Pittsburg, PA, 1991.
- [5.12] F. Rey, G. Sankar, J. M. Thomas, P. A. Barrett, D. W. Lewis, C. R. A. Catlow, S. M. Clark, G. N. Greaves, *Chem. Mater.* **7**, 1435 (1995).
- [5.13] G. Muncaster, A. T. Davies, G. Sankar, C. R. A. Catlow, J. M. Thomas, S. L. Colston, P. Barnes, R. I. Walton, D. O'Hare, *Phys. Chem. Chem. Phys.* **2**, 3523 (2000).
- [5.14] D. W. Lewis, C. R. A. Catlow, J. M. Thomas, *Faraday Discuss.* 451 (1997).
- [5.15] D. W. Lewis, C. R. A. Catlow, J. M. Thomas, *Chem. Mater.* **8**, 1112 (1996).
- [5.16] N. Rajic, D. Stojakovic, S. Hocevar, V. Kaucic, *Zeolites* **13**, 384 (1993).
- [5.17] G. Nardin, L. Randaccio, V. Kaucic, N. Rajic, *Zeolites* **11**, 192 (1991).
- [5.18] A. M. Prakash, S. Unnikrishnan, *J. Chem. Soc. – Faraday Trans.* **90**, 2291 (1994).
- [5.19] S. Ashtekar, S. V. V. Chilukuri, A. M. Prakash, D. K. Chakrabarty, *J. Phys. Chem.* **100**, 3665 (1996).
- [5.20] S. Ashtekar, S. V. V. Chilukuri, A. M. Prakash, C. S. Harendranath, D. K. Chakrabarty, *J. Phys. Chem.* **99**, 6937 (1995).
- [5.21] E. Dumitriu, A. Azzouz, V. Hulea, D. Lutic, H. Kessler, *Microporous Mater.* **10**, 1 (1997).
- [5.22] C. U. Denavarro, F. Machado, M. Lopez, D. Maspero, J. Perezpariente, *Zeolites* **15**, 157 (1995).
- [5.23] Y. Xu, P. J. Maddox, J. W. Couves, *J. Chem. Soc. – Faraday Trans.* **86**, 425 (1990).
- [5.24] M. M. Harding, B. M. Kariuki, *Acta Crystallogr. Sect. C Cryst. Struct.*

- Commun.* **50**, 852 (1994).
- [5.25] N. Rajic, A. Ristic, A. Tuel, V. Kaucic, *Zeolites* **18**, 115 (1997).
- [5.26] H. Kessler, J. Patarin, C. Schott-Darie, *Stud. Surf. Sci. Catal.* **85**, 85 (1994).
- [5.27] C. Fernandez, J. P. Amoureux, L. Delmotte, H. Kessler, *Microporous Materials* **6**, 125 (1996).
- [5.28] A. Tuel, S. Caldarelli, A. Meden, L. B. McCusker, Ch. Baerlocher, A. Ristić, N. Rajić, G. Mali, V. Kaučič, *J. Phys. Chem.* **B 104**, 5697 (2000).
- [5.29] D. Muller, W. Gessner, A. R. Z. Grimmer, *Chem.* **17**, 453 (1977).
- [5.30] D. Muller, W. Gessner, H. J. Behrens, G. Scheler, *Chem. Phys. Lett.* **79**, 59 (1981).
- [5.31] V. M. Mastikhin, O. P. Krivorochko, B. P. Zolotovskii, R. A. Buyanov, *React. Kinet. Catal. Lett.* **18**, 117 (1981).
- [5.32] D. Freude, H. J. Behrens, *Cryst. Res. Technol.* **16**, K36 (1981).
- [5.33] F. V. Lampe, D. Muller, W. Gessner, A. R. Grimmer, G. Z. Scheler, *Anorg. Allg. Chem.* **489**, 16 (1982).
- [5.34] B. H. W. S. de Jong, C. M. Schramm, V. E. Parziale, *Cosmochim. Acta* **47**, 1223 (1983).
- [5.35] E. L. Eliel, D. Kandansamy, C. Y. Yen, D.D. Hargrave. *J. Am. Chem. Soc.* **102**, 3698 (1980).
- [5.36] D. Massiot, B. Touzo, D. Trumeau, et al., *Solid State Nucl. Magn. Reson.* **6**, 73 (1996).
- [5.37] O. W. Sorensen, M. Rance, R. R. Ernst, *J. Magn. Reson.* **56**, 527 (1984).
- [5.38] J. P. Amoureux, C. Fernandez, S. Steuernagel, *J. Magn. Reson.* **A123**, 116 (1996).
- [5.39] http://riodb01.ibase.aist.go.jp/sdbs/cgi-bin/cre_index.cgi
- [5.40] E. R. Cooper, C. D. Andrews, P. S. Wheatley, P. B. Webb, P. Wormald, R. E. Morris, *Nature* **430**, 1012 (2004).
- [5.41] E. R. Parnham, P. S. Wheatley, R. E. Morris, *Chem. Commun.* **380**, (2006).

- [5.42] E. R. Parnham, R. E. Morris, *Accounts of Chemical Research* **40** (10), 1005 (2007).
- [5.43] J. Yu, J. Li, K. Sugiyama, N. Togashi, O. Terasaki, K. Hiraga, B. Zhou, S. Qiu, R. Xu, *Chem. Mater.* **11**, 1727 (1999).
- [5.44] C. Schott-Darie, H. Kessler, E. Benazzi, *Stud. Surf. Sci. Catal.* **83**, 3 (1994).
- [5.45] D. Massiot, I. Farnan, N. Gautier, D. Trameau, A. Trokiner et. al, *Solid State Nucl. Magn. Reson.* **4**, 241 (1995).
- [5.46] D. Massiot, I. Farnan, N. Gautier, D. Trameau, P. Florian et. al, *J. Chem. Phys.* **92**, 1847 (1995).
- [5.47] T. Vosegaard, D. Massiot, N. Gautier, H. Jakobsen, *Inorg. Chem.* **36**, 2446 (1997).
- [5.48] T. Vosegaard, I. P. Byriel, L. Binet, D. Massiot, H. Jakobsen, *J. Am. Chem. Soc.* **120**, 8184 (1998).
- [5.49] D. Massiot, T. Vosegaard et. al, *Solid State Nucl. Magn. Reson.* **15**, 159 (1999).
- [5.50] S. M. Bradley, R. F. Howe, R. A. Kydd, *Magn. Reson. Chem.* **31**, 883 (1993).